



INSTITUTE FOR COMPUTER SCIENCE VII
ROBOTICS AND TELEMATICS

Bachelor's thesis

Evaluation of Quantity and Positioning of Inertial Measurement Units for different Spherical Robot Types regarding the Orientation Determination

Carolin Bösch

January 2023

First reviewer: Prof. Dr. Andreas Nüchter
Advisor: M.Sc. Jasper Zevering

Zusammenfassung

Die vorliegende Arbeit befasst sich mit der Bewertung von Inertial Measurement Unit (IMU)-Konfigurationen für verschiedene Typen von kugelförmige Roboter bezüglich der Genauigkeit der Orientierungsbestimmung. Hintergrund dieser Arbeit ist die Descent And Exploration in Deep Autonomy of Lava Underground Structures (DAEDALUS) Mission, bei der ein kugelförmiger Roboter den Eingang und den ersten Teil der Lavaröhren auf dem Mond erkunden und charakterisieren soll. Für den Rahmen dieser Arbeit haben wir ein Programm zur Orientierungsbestimmung geschrieben, welches dynamisch die angeschlossenen IMUs verwaltet. Voraussetzung für die interne Achsenzuordnung der IMUs ist, dass diese auf den Rotationsachsen angebracht sind und ihre Orientierung um eine beliebige Anzahl von 90° -Drehungen von der Ausrichtung des Base Coordinate System (BCS) abweicht.

In einer Reihe von vier Experimenten evaluieren wir verschiedene Aspekte von IMU Konfigurationen. Im ersten Experiment untersuchen wir den Zusammenhang zwischen der Anzahl der IMUs und der Genauigkeit der Orientierungsbestimmung. Die Ergebnisse zeigen eine exponentiell sinkende Tendenz des Root Mean Square Error (RMSE) mit zunehmender Anzahl von IMUs. Im zweiten Experiment untersuchen wir den Zusammenhang zwischen der Genauigkeit der Orientierungsbestimmung und dem Abstand der IMU zum Zentrum der Sphäre. Aus den Ergebnissen erkennen wir, dass eine IMU im Zentrum die genauesten Daten liefert. Im dritten Experiment zeigen wir, dass die symmetrische Anbringung von zwei IMUs auf einer Rotationsachse auf unterschiedlichen Seiten des Sphärenzentrums im Vergleich zu beiden IMUs auf einer Seite keine genauere Orientierung liefert. Im letzten Experiment vergleichen wir die Platzierung von einer IMU auf jeder Rotationsachse mit drei IMUs im Zentrum der Sphäre und mit einer IMU auf jeder Rotationsachse und eine im Zentrum der Sphäre. Die genaueste Orientierung liefern die IMUs im Zentrum der Sphäre und drei IMUs außen liefern die Ungenaueste. Auf der Grundlage dieser Erkenntnisse haben wir die optimalen Konfigurationen zur Bestimmung der Orientierung für die verschiedenen Robotertypen festgelegt.

Zusammenfassend ist zu sagen, dass wir die Grundaussagen der getesteten Zusammenhänge zwischen bestimmten Aspekten von IMU Konfigurationen und der Genauigkeit der Orientierungsbestimmung getroffen haben. Jedoch besteht die Möglichkeit, dass wir genauere Zusammenhänge aufgrund der Ungenauigkeit der gewählten Grundwahrheit nicht aufstellen konnten.

Abstract

This thesis deals with the evaluation of IMU configurations for different spherical robot types in terms of orientation determination accuracy. The background of this work is the DAEDALUS mission, in which a spherical robot is designed to explore and characterize the entrance and first part of the lava tubes on the Moon. For the scope of this work, we wrote an orientation determination program that dynamically manages the attached IMUs. The prerequisite for the internal axis assignment of the attached IMUs is that the IMUs are attached to the rotation axes and their orientation differs from the orientation of the BCS by an arbitrary number of 90° rotations.

In a series of four experiments, we evaluate different aspects of IMU configurations. In the first experiment, we investigate the relationship between the number of IMUs and the accuracy of orientation determination. The results show an exponential downward trend of the RMSE with increasing number of IMUs. In the second experiment, we investigate the relationship between the accuracy of orientation determination and the distance of an IMU from the center of the sphere. From the results, we see that an IMU at the center provides the most accurate orientation. In the third experiment, we show that placing two IMUs on opposite sides of the sphere's center on one axis of rotation does not provide more accurate orientation compared to placing both IMUs on one side. In the last experiment we compare the following configurations: one IMU on each rotation axis, three IMUs in the center of the sphere, and one IMU on each rotation axis plus one IMU in the center of the sphere. The most accurate orientation is provided by the IMUs at the center of the sphere and the least accurate orientation is provided by the three IMUs on the outside. Based on these findings, we set up the optimal configurations for the different types of robots to determine their orientation.

In summary, we have established the ground truth of the tested relationships between certain aspects of IMU configurations and the accuracy of orientation determination. However, there is a possibility that we could not establish more precise correlations due to the imprecision of the chosen ground truth.

Contents

1	Introduction	1
2	Related Work	3
2.1	Characteristics of Multi Inertial Sensor Systems	3
2.2	IMU-based pose-estimation for spherical robots	7
3	Theoretical Background	9
3.1	Orientation	9
3.2	Inertial Measurement Unit (IMU)	11
3.3	Madgwick Filter	14
3.4	Complementary Filter	16
3.5	Spherical Robot Types	17
4	Theory	25
4.1	General Approach	25
4.2	Specific Approach	26
5	Experiments and Evaluation	29
5.1	Technical Setup	29
5.1.1	Inertial Measurement Unit (IMU)	29
5.1.2	Ground Truth	29
5.1.3	Periphery	30
5.1.4	Orientation Determination	32
5.2	Experiments	34
5.2.1	Experiment A: Number of IMUs	37
5.2.2	Experiment B: Distance from Center	44
5.2.3	Experiment C: Symmetry in Placement	47
5.2.4	Experiment D: Axial Placement	49
5.3	Comparison and Discussion	52
6	Conclusions	57

A	Raw Data Plots	59
A.1	Experiment A	59
A.2	Experiment B	78
A.3	Experiment C	90
A.4	Experiment D	96

List of Figures

2.1	Exemplary optimal configurations for five sensors (black arrows) on a cone	6
3.1	Representation of an orientation change using coordinate systems.	10
3.2	Illustration of the rotation order of the $Z - Y' - X''$ Euler Angle convention . .	11
3.3	Visualization of a spring and mass system in a resting state.	12
3.4	Illustration of the operation principle of a gyroscope.	13
3.5	Schematic representation of the mechanical structure of a gyroscope.	13
3.6	Visualization of the concept of a Micro-Electro-Mechanical System (MEMS) mag- netometer.	14
3.7	Block diagrams of the Complementary Filter.	17
3.8	Schematic of a spherical robot with pendulum mechanism.	18
3.9	Schematic of a spherical robot with Internal Drive Unit (IDU).	19
3.10	Example of a spherical robot with an universal wheel (BHQ-3).	19
3.11	Schematic of a spherical robot with shifting masses mechanism and exemplary design (Mojabi).	20
3.12	Cross-section of a shell transforming spherical robot with pressurized air bladders in motion.	21
3.13	Cross-section of spherical robot with deformable shell in different stages.	21
3.14	Component diagram (left) and a side view (right) of the Gyrover.[1]	22
3.15	Internal structure of Joshi's spherical robot using reaction wheels.[2]	22
3.16	Blueprint of the rod-driven robot without the spherical shell.[3]	23
3.17	Illustration of the locomotion principles of rod-driven robots.	23
5.1	Illustration of the $AX = BY$ coordinate transformation on the basis of an exem- plary experimental setup with two sets of 6 Degrees of Freedom (DOF) data. . .	30
5.2	Mounting for the IMUs as Computer-Aided Design (CAD) Model.	31
5.3	Picture of the real mounting for the IMUs.	31
5.4	Blueprint of the base plate in scale 1:2.	32
5.5	Blueprint of the small plate in scale 1:2.	33
5.6	Schematic visualization of Experiment A: different number of IMUs in the center. .	34
5.7	Schematic visualization of Experiment B: different distances of the IMU from the center.	35
5.8	Schematic visualization of Experiment C: symmetrical placement of the IMU from the center.	35

5.9	Schematic visualization of Experiment D: different axis assignment of the IMUs.	36
5.10	Illustration of the data obtained in the first test experiment (shell closed and yaw rotation) of Configuration A1 as Euler angles.	38
5.11	Display of the balls recognized by the three cameras of the Optitrack system (detail of the Motive:Tracker software).	39
5.12	Illustration of the data obtained in the second test experiment (shell open and Yaw rotation) of Configuration A1 as Euler angles.	40
5.13	Mean absolute error of Roll and Pitch as a function of the angular velocity around their respective rotational axis.	41
5.14	Bar graph: RMSE for each of the performed experiments and the merged RMSE for each configuration of Experiment A.	43
5.15	Bar graph: RMSE for each of the performed experiments and the merged RMSE for each configuration of Experiment B.	46
5.16	Bar graph: RMSE for each of the performed experiments and the merged RMSE for each configuration of Experiment C.	48
5.17	Bar graph: RMSE for each of the performed experiments and the merged RMSE for each configuration of Experiment D.	51
5.18	End results of Experiment A. Merged RMSE [rad] for each configuration plotted against the number of IMUs.	52
5.19	End results of Experiment B. Merged RMSE [rad] for each configuration plotted against the distance d from the center of the sphere.	53
A.1	Illustration of the data obtained in the first experiment (Roll rotation) of Configuration A1 as Euler angles.	60
A.2	Illustration of the data obtained in the second experiment (Pitch rotation) of Configuration A1 as Euler angles.	61
A.3	Illustration of the data obtained in the third experiment (Roll and Pitch rotation) of Configuration A1 as Euler angles.	62
A.4	Illustration of the data obtained in the first experiment (Roll rotation) of Configuration A2 as Euler angles.	63
A.5	Illustration of the data obtained in the second experiment (Pitch rotation) of Configuration A2 as Euler angles.	64
A.6	Illustration of the data obtained in the third experiment (Roll and Pitch rotation) of Configuration A2 as Euler angles.	65
A.7	Illustration of the data obtained in the first experiment (Roll rotation) of Configuration A3 as Euler angles.	66
A.8	Illustration of the data obtained in the second experiment (Pitch rotation) of Configuration A3 as Euler angles.	67
A.9	Illustration of the data obtained in the third experiment (Roll and Pitch rotation) of Configuration A3 as Euler angles.	68
A.10	Illustration of the data obtained in the first experiment (Roll rotation) of Configuration A4 as Euler angles.	69
A.11	Illustration of the data obtained in the second experiment (Pitch rotation) of Configuration A4 as Euler angles.	70

A.12 Illustration of the data obtained in the third experiment (Roll and Pitch rotation) of Configuration A4 as Euler angles.	71
A.13 Illustration of the data obtained in the first experiment (Roll rotation) of Configuration A5 as Euler angles.	72
A.14 Illustration of the data obtained in the second experiment (Pitch rotation) of Configuration A5 as Euler angles.	73
A.15 Illustration of the data obtained in the third experiment (Roll and Pitch rotation) of Configuration A5 as Euler angles.	74
A.16 Illustration of the data obtained in the first experiment (Roll rotation) of Configuration A6 as Euler angles.	75
A.17 Illustration of the data obtained in the second experiment (Pitch rotation) of Configuration A6 as Euler angles.	76
A.18 Illustration of the data obtained in the third experiment (Roll and Pitch rotation) of Configuration A6 as Euler angles.	77
A.19 Illustration of the data obtained in the first experiment (Roll rotation) of Configuration B1 as Euler angles.	78
A.20 Illustration of the data obtained in the second experiment (Pitch rotation) of Configuration B1 as Euler angles.	79
A.21 Illustration of the data obtained in the third experiment (Roll and Pitch rotation) of Configuration B1 as Euler angles.	80
A.22 Illustration of the data obtained in the first experiment (Roll rotation) of Configuration B2 as Euler angles.	81
A.23 Illustration of the data obtained in the second experiment (Pitch rotation) of Configuration B2 as Euler angles.	82
A.24 Illustration of the data obtained in the third experiment (Roll and Pitch rotation) of Configuration B2 as Euler angles.	83
A.25 Illustration of the data obtained in the first experiment (Roll rotation) of Configuration B3 as Euler angles.	84
A.26 Illustration of the data obtained in the second experiment (Pitch rotation) of Configuration B3 as Euler angles.	85
A.27 Illustration of the data obtained in the third experiment (Roll and Pitch rotation) of Configuration B3 as Euler angles.	86
A.28 Illustration of the data obtained in the first experiment (Roll rotation) of Configuration B4 as Euler angles.	87
A.29 Illustration of the data obtained in the second experiment (Pitch rotation) of Configuration B4 as Euler angles.	88
A.30 Illustration of the data obtained in the third experiment (Roll and Pitch rotation) of Configuration B4 as Euler angles.	89
A.31 Illustration of the data obtained in the first experiment (Roll rotation) of Configuration C1 as Euler angles.	90
A.32 Illustration of the data obtained in the second experiment (Pitch rotation) of Configuration C1 as Euler angles.	91
A.33 Illustration of the data obtained in the third experiment (Roll and Pitch rotation) of Configuration C1 as Euler angles.	92

A.34	Illustration of the data obtained in the first experiment (Roll rotation) of Configuration C2 as Euler angles.	93
A.35	Illustration of the data obtained in the second experiment (Pitch rotation) of Configuration C2 as Euler angles.	94
A.36	Illustration of the data obtained in the third experiment (Roll and Pitch rotation) of Configuration C2 as Euler angles.	95
A.37	Illustration of the data obtained in the first experiment (Roll rotation) of Configuration D1 as Euler angles.	96
A.38	Illustration of the data obtained in the second experiment (Pitch rotation) of Configuration D1 as Euler angles.	97
A.39	Illustration of the data obtained in the third experiment (Roll and Pitch rotation) of Configuration D1 as Euler angles.	98
A.40	Illustration of the data obtained in the first experiment (Roll rotation) of Configuration D2 as Euler angles.	99
A.41	Illustration of the data obtained in the second experiment (Pitch rotation) of Configuration D2 as Euler angles.	100
A.42	Illustration of the data obtained in the third experiment (Roll and Pitch rotation) of Configuration D2 as Euler angles.	101
A.43	Illustration of the data obtained in the first experiment (Roll rotation) of Configuration D3 as Euler angles.	102
A.44	Illustration of the data obtained in the second experiment (Pitch rotation) of Configuration D3 as Euler angles.	103
A.45	Illustration of the data obtained in the third experiment (Roll and Pitch rotation) of Configuration D3 as Euler angles.	104

List of Tables

5.1	Results of Experiment A. Specification of the RMSE in rad. RMSE in x (Roll) and y (Pitch) direction and merged RMSE for each of the performed experiments. Merged RMSE for each configuration (gray rows).	42
5.2	Results of Experiment A. Relative Improvement compared to the first experiment (here A1).	43
5.3	Results of Experiment B. Specification of the RMSE in rad. RMSE in x (Roll) and y (Pitch) direction and merged RMSE for each of the performed experiments. Merged RMSE for each configuration (gray rows).	45
5.4	Results of Experiment B. Relative Improvement compared to the first experiment (here B1).	45
5.5	Results of Experiment C. Relative Improvement compared to the first experiment (here C1).	47
5.6	Results of Experiment C. Specification of the RMSE in rad. RMSE in x (Roll) and y (Pitch) direction and merged RMSE for each of the performed experiments. Merged RMSE for each configuration (gray rows).	48
5.7	Results of Experiment D. Specification of the RMSE in rad. RMSE in x (Roll) and y (Pitch) direction and merged RMSE for each of the performed experiments. Merged RMSE for each configuration (gray rows).	50
5.8	Results of Experiment D. Relative Improvement compared to the first experiment (here D1).	50
5.9	End results of Experiment A. Merged RMSE for each configuration.	52
5.10	Results of Experiment A. Relative Improvement compared to previous configuration (improvement for A2 in reference to A1, and improvement for A3 in reference to A2, etc.).	53
5.11	End results of Experiment B. Merged RMSE for each configuration.	54
5.12	End results of Experiment C. Merged RMSE for each configuration.	54
5.13	End results of Experiment D. Merged RMSE for each configuration.	54

Chapter 1

Introduction

Since the 1960s, people have been sending rovers to celestial bodies other than Earth to explore the universe remotely. The first rover to land on the moon was Lunokhod 1 by the Soviet Union in 1970 [4]. For navigation it was equipped with television cameras that transmitted images of the environment, which enabled remote control from Earth [5]. Then in 1997, the Sojourner rover from National Aeronautics and Space Administration (NASA) as part of the Mars Pathfinder mission became the first rover to successfully deploy on another planet. Sojourner used a computerized control system to move independently and a system of photographic objectives and laser emitters to identify obstacles along its path. Furthermore, NASA installed a gyroscope to determine the robot's heading during a turn maneuver and three accelerometers. Those measured the acceleration of gravity along three perpendicular directions, making it possible to measure the surface's slope [6]. Based on this research and testing of inertial sensors in space, the Mars Exploration Rovers, Spirit and Opportunity with their mission to explore the geological conditions on Mars and look for evidence of water, incorporated an IMU. With the installed IMU each rover is able to determine its tilt [7]. Later missions, such as Curiosity from NASA's Mars Science Laboratory mission, launched in 2011, and NASA's Mars2020 Perseverance rover, extend the use of IMUs not only to determine the tilt of the rover, but also to support the navigation with 3-axis information on its position [8, 9].

Newer missions and concepts, such as Laser-Mapping Unidirectional Navigation Actuator (L.U.N.A.) [10] and the DAEDALUS [11], deal with the idea of sending spherical robots into space. The new type of robot poses new challenges. Spherical robots roll instead of moving on wheels or legs. The L.U.N.A. sphere moves with the help of momentum, which is generated by flywheels. Due to the mission's concept, the laser scanner is at the center of the sphere. Therefore, they place three IMUs located off-center to simulate one virtual IMU at the center. The z -axes of the imus correspond to one possible rotation axis of the sphere, ergo a perpendicular arrangement. DAEDALUS is also a compact spherical robot for exploring underground lava tubes on the moon or other extraterrestrial areas. It moves with rods and thus belongs to the group of rod-driven spherical robots. The primary exploration tool set within the sphere is a Light Detection and Ranging (Lidar) scanner to produce 3D models with high spatial accuracy. For these models to be very accurate, it is better to place the scanner in the center of the sphere to avoid translational movements up and down during locomotion. However, with regard to

the placement of the sensors, this also implies that only off centered placement of the IMUs is possible. Based on this, this thesis deals with the evaluation of IMU configurations for general spherical robot types and specifically the DAEDALUS sphere.

Outline

The structure of this thesis is as follows: In Chapter 2 we summarize previous works on the use of multiple sensors and IMUs. We also sum up the main characteristics of Multi Inertial Sensor and Multi Inertial Measurement Unit (MIMU) systems and introduce an inertial measurement-based pose estimation method for spherical robots. In Chapter 3 we present theoretical background knowledge about orientation, IMU and its functionality, the Madgwick and the Complementary Filter, and the different types of spherical robots. Next, in Chapter 4 we analyze possible IMU architectures for the different spherical robot types and define the experiments to be performed. In Chapter 5 we first describe the technical setup for the experiments and following the execution of the experiments. Then we compare the obtained data and discuss the results. Lastly, in Chapter 6 we give a final conclusion and an outlook of the knowledge gained.

Chapter 2

Related Work

In this Chapter, we first discuss previous works on the use of multiple IMUs, or sensors in general, and the characteristics of MIMU systems. Subsequently, we present an inertial measurement-based pose estimation method for spherical robots, which serves as the basis for the orientation determination of this work.

2.1 Characteristics of Multi Inertial Sensor Systems

IMUs are nowadays built into many consumer electronics devices, such as smartphones, tablet computers, video games, toys, power tools, and so on. This promotes the rapid development of MEMS technology and reduces the size, cost, and power consumption of IMUs. But these low cost, compact IMUs have lower accuracy than high-end sensors. For systems that require better performance than a single IMU can provide, one approach is to fuse multiple IMUs into a single high-performance artificial IMU.[12–14]

Skog [12] built a low-cost embedded MIMU platform with single-chip ultra-low-cost IMUs and a parallel software data bus. Moreover, he gives a comprehensive overview of the basic characteristics of MIMU systems and the corresponding gains. In summary, the fundamental properties of MIMU systems are

- 1) Stochastic Error Diversity ,
- 2) Component Redundancy and Diversity,
- 3) Spatial Diversity,
- 4) Temporal Diversity.

The first property of MIMU systems is stochastic error diversity, which allows independent stochastic errors, such as distortion and noise, to be suppressed by combining the independent measurements. This fundamental gain does not depend on the combination strategy. The second property of MIMU systems is the component redundancy and diversity. In the event of an IMU failure, the system is able to continue to operate using the remaining functioning sensors. It is possible to identify and isolate the failing IMU for systems with 3 IMUs or more. In addition, the

use of IMUs with complementary measurement characteristics has further specific advantages, such as the measurement of inertia over an extended dynamic range without introducing a significant amount of noise. The spatial and dynamics diversity allows the MIMU systems in the rigid fixation of the IMUs to capture rotational information with the accelerometers due to the separation of the sensors. Nevertheless, the gyroscopes all sense the same rotation. In case of non-rigid relations between the IMUs, it is not possible to set the measurements in relation to each other. Finally, multiple asynchronous IMUs give an effective higher sampling rate as a result of temporal diversity and effective sampling rate. Since we use synchronous IMUs for this work, we do not elaborate the temporal diversity further.

Stochastic Error Diversity

First experiments with MEMS IMUs pursue to enhance navigation performance of Global Positioning Systems (GPSs), such as presented in [15]. They show that four IMUs increase navigation performance, particularly that of orientation, by 30 to 50 %.

Further research seeks to determine the number of sensors required to meet a specific accuracy or predetermined specifications using the stochastic error diversity. Guerrier [16] presents a simulation tool that can be used for this purpose. It also aims to establish the alignment of sensors with system performance (discussed later in Chapter 2.1). His work shows an inverse correlation between the error magnitude and the number of employed sensors. Moreover, it shows that for n independent measurements (ergo measurements from n independent IMUs) of equal variance (σ_n^2) the theoretical noise reduction $\sigma_{\hat{x}}$, with

$$\sigma_{\hat{x}} = \frac{\sigma_{xi}}{\sqrt{n}}, \quad (1)$$

represents the maximum improvement in navigation performance. This relation applies to any sensor configuration. But it is most likely limited by the correlations between the inertial measurements and the correlations between the Extended Kalman Filter (EKF) states. Crain [17] also establishes this correlation between the number of IMUs used n and noise reduction. Furthermore, he shows that after $n = 10$, the effective reduction in error per unit has reached a point where improving accuracy is no longer profitable. It follows, that single unit failures do not affect overall performance in MIMU systems of 10 to 15 units. In addition to the above research, Ludwig [13] evaluates different numbers of sensor configurations of a Magnetic and Inertial Measurement Unit (MagIMU) sensor array using a simulation environment. Using the Madgwick Filter, he incrementally adds MagIMU sensors with different rotations to estimate the Euler angles of the foot-mounted data. The evaluation measure employed is the RMSE based on Euler angles versus ground truth. The results show an exponential downward trend in the RMSE values as predicted by [16] and [17]. It is possible to detect this trend in the relative improvement values for an increasing number of sensors. In numbers, there is a relative improvement of 11.54 % when using two sensors and 26.01 % when using 16 sensors. Based on the finding of equation 1, Greenheck [18] develops and demonstrates an IMU cluster configuration that meets the mass, energy, and volume constraints of a 1U CubeSat to produce the predicted improvement. He places multiple MEMS sensors on a single circuit board and synthesizes the outputs to yield a single output. Using simple averaging of the sensor data, the results generally

approximate the predicted square root of n of the performance improvement for the RMSE. Some sensors show lower performance improvement than others, which suggests a higher correlation between individual sensors.

Component Redundancy

Motivated by the use of a cluster of MEMS IMUs configured for use in a CubeSat platform [18], Bittner [19] examines Fault Detection, Isolation, and Recovery (FDIR) for large IMU clusters using a k -th nearest neighbor algorithm to identify failed IMUs. He recognizes that the greatest potential of MIMU systems due to the component redundancy lies in the ability to detect and isolate faults. Srivastava [20] states, that FDIR techniques have proven to be especially important for autonomous and robotic missions of the aerospace industry, such as Unmanned Aerial Vehicles (UAVs), and for manned missions, where errors must be detected and intercepted before they endanger the crew.

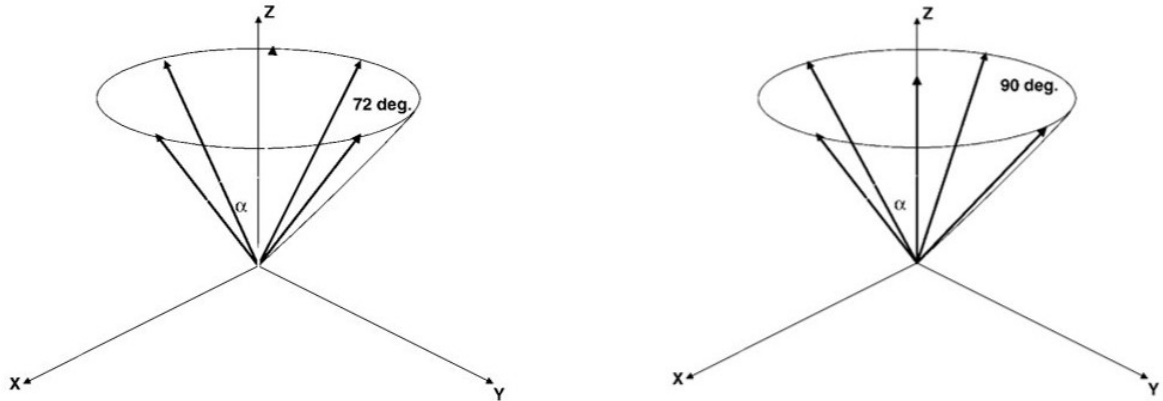
Essentially, by placing two sensors colinear with each other, it is possible to determine if a fault has occurred in one of the sensors and three sensors are required to isolate the fault. For a complete three-dimensional system, nine sensors are required (three on each axis) ergo three IMUs.[21]

Spatial Diversity

Pesja [22] developed the first theory for obtaining an optimal configuration regarding the placement of any number of sensors in 1974. Here, he distributes an arbitrary number of sensors uniformly on a cone with the half angle α . The criterion applied is the determination of the half angle. This in turn minimizes the average statistical uncertainty of the configuration, which is a function of the half angle and the uncertainty of the individual sensors. Figure 2.1 shows exemplary optimal configurations for five sensors.

Based on Pesja's finding that optimal configurations in information space take the form of a sphere, i.e. an equal amount of information on each axis, Sukkarieh [21] introduces a method for obtaining an optimal configuration by using an information filter. In other words, he considers the entire information contained in the configuration, rather than an average uncertainty (or certainty) in the statistical sense. The results in the two-dimensional case show that for n identical sensors, or n sensors with equal variance, the optimal configuration conforms to a homogeneous distribution on a unit circle. This corresponds to the shape of a regular polygon. In the three-dimensional case, on the other hand, there is no unique solution, since the optimal configuration, despite having a unique shape, can have an arbitrary orientation. For 4 sensors, the shape of the optimal configuration corresponds to a tetrahedron, and for 6 sensors to an octahedron. Generally, regular polyhedra is the optimal configuration for 4, 6, 8, 12, and 20 sensors. Both cases confirm Pesja's conclusion.

According to Guerrier [16], another method to express the optimality of a redundant IMUs configuration in addition to the information filter method is the partial redundancy method. Here, Guerrier uses the term optimal to describe the improvement in accuracy for a given number of IMUs. This method is usually applied in geodetic networks and evaluates the controllability of each sensor. An optimal sensor configuration minimizes the difference in controllability of



(a) Optimal Placement with a half angle α of 54.74° . Sensors equally separated by 72° along the cone.

(b) Four sensors placed on the cone equally separated by 90° , while the fifth sensor is on the cone axis. The half angle is now 65.91° .

Figure 2.1: Optimal Placement of five sensors on a cone. The cone spans from the upper circle around the z -axis and the coordinate system center. [21]

the individual sensors. This method leads in general to similar results as the information filter approach. Further, this method shows that for triaxial IMUs, the relative sensor alignment is irrelevant to the optimality of the system. Therefore, he recommends an orthogonal arrangement, which is usually the simplest configuration, to avoid unnecessary burdening, especially for systems with more than three IMUs.

According to Zevering [10] one non-centered IMU leads to lower quality measurements. Therefore, they combine the data of three non-centered IMUs, where each IMU only measures the static rotation along one of the rotational axes. This method leads to less noise in the overall angular velocity measurements.

In the case of sensors, however, it is necessary to distinguish between location-dependent and location-independent sensors. The measurement data of gyroscopes is independent of the positioning. The accelerometer and magnetometer data of an IMU, on the other hand, are dependent on the position of the sensor [23]. Zappa [24] uses this fact to obtain the complete acceleration state of a rigid body with twelve accelerometers under the following conditions:

- 1) Division of the accelerometers into three groups,
- 2) Same orientation for all accelerometers of each group,
- 3) Different and linearly independent orientation of the three groups,
- 4) Non-coplanar accelerometers within each group.

The equations become simplified if the three directions from point 3) are orthogonal to each other. This means 4 non-coplanar IMUs, each with a triaxial accelerometer, are sufficient to measure the angular velocity of the body.

2.2 IMU-based pose-estimation for spherical robots

The orientation determination in this paper is based on Zevering's pose determination using IMUs [25]. He presents a spherical robot pose determination method that works for any spherical robot with IMUs that moves based on rotation. It has low jitter to keep the world measurements constant at standstill and also avoids exponentially growing errors in position estimation. The prerequisite in this approach is that the IMUs rotate along with at least the shell of the robot. This method exhibits reduced jitter in orientation for given ground truths, as well as better handling of slip and partial slide behavior than other commonly used filters such as the Madgwick filter. The use of this method compares advantageously with existing approaches under the following assumptions and conditions:

- A) Real time operations,
- B) Limitation of computational power,
- C) Low costs of hardware,
- D) Spherical shape with a constant radius,
- E) Sphere affected by slip and slide,
- F) Slightly false pose preferred over exact but noisy and jumping position,
- G) Avoidance of jumping values or abrupt changes of data,
- H) Uncertainty of iterative position integration,
 - I) No use of magnetometer for space suitability,
 - J) Short term mobility for use with laser scanners,
- K) Non-reliability of locomotion commands.

For orientation, he uses a combination of the Madgwick and the Complementary Filter. Zevering applies the Madgwick Filter for motion and the Complementary Filter at standstill, because the Madgwick Filter exhibits jittering behavior at standstill and the Complementary Filter is disturbed by motion due to its dependence on the gravity vector. Depending on the estimated state of motion of the sphere, he realizes the transition between the two filters by assigning a certain fixed factor to the filter weights. This factor is determined by a quadratic function and the empirically determined threshold values of the filters. This ensures a smooth transition without jumping values and abrupt changes in behavior.

Chapter 3

Theoretical Background

In this chapter, we provide an overview of essential theoretical background knowledge. First, we explain what orientation is and how it can be represented. Then we introduce IMUs and how they work. This is followed by the Madgwick Filter and the Complementary Filter for orientation estimation. Finally, we present the different spherical robot types including an indication for possible sensor placement.

3.1 Orientation

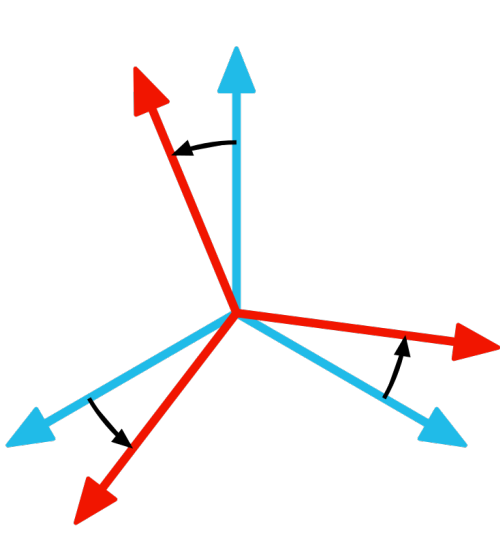
In geometry, the orientation of an object is part of the description of how it is arranged in the space it occupies. Other names for orientation are angular position, attitude, bearing, or direction. The position and orientation of an object describe its placement in space completely. More precisely, the position, or location, describes an imaginary displacement of the object in space. Whereas the orientation is an imaginary rotation required to move the object from a reference position to its current position, as shown in Figure 3.1a. In general, the orientation is given relative to a reference frame, which is usually specified by a Cartesian coordinate system.[26]

The orientation of an object can be parameterized in many different ways, such as rotation matrices or rotation vectors. A common representation is the unit quaternion, first presented in 1844 by Hamilton [27]. The unit quaternion is a 4×1 vector consisting of a 3×1 vector q_v and a scalar q_0 . In order for it to be a unit quaternion, the length of the 4×1 vector must equal 1. Therefore, we get

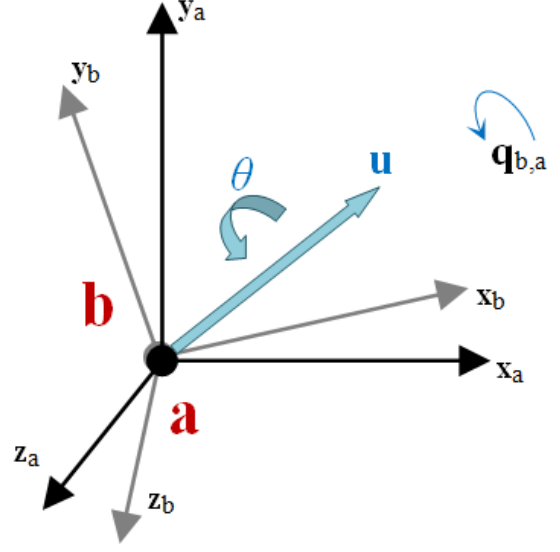
$$q = \left(q_0 \quad q_1 \quad q_2 \quad q_3 \right)^\top = \begin{pmatrix} q_0 \\ q_v \end{pmatrix}, \text{ with } \|q\| = 1. \quad (2)$$

The vector q_v represents the axis and the scalar q_0 represents the angle of rotation [28], as shown in Figure 3.1b. According to [29], the individual values of the quaternion are calculated for a rotation with an angle of θ about a vector $k = [k_x \ k_y \ k_z]^\top$ with

$$q_0 = \cos \frac{\theta}{2}, \quad q_1 = k_x \sin \frac{\theta}{2}, \quad q_2 = k_y \sin \frac{\theta}{2}, \quad q_3 = k_z \sin \frac{\theta}{2}. \quad (3)$$



(a) Changing orientation of an object, before (blue) vs. after (red), illustrated by the coordinate system attached to the object.[26]



(b) Illustration of an quaternion orientation change. Change of orientation from frame a to frame b with an angle of θ around the vector u , that result into the quaternion $q_{b,a} = [\theta u]^\top$. [30]

Figure 3.1: Representation of an orientation change using coordinate systems.

It is also possible to construct the rotation matrix R_q from a given quaternion q and vice versa, the quaternion q_R from a given rotation matrix R with

$$R_q = \begin{pmatrix} 1 - 2q_2^2 - 2q_3^2 & 2(q_1q_2 - q_3q_0) & 2(q_1q_3 + q_2q_0) \\ 2(q_1q_2 + q_3q_0) & 1 - 2q_1^2 - 2q_3^2 & 2(q_2q_3 - q_1q_0) \\ 2(q_1q_3 - q_2q_0) & 2(q_2q_3 + q_1q_0) & 1 - 2q_1^2 - 2q_2^2 \end{pmatrix}, \quad (4)$$

$$\begin{aligned} q_{R0} &= \frac{1}{2} \sqrt{1 + r_{11} + r_{22} + r_{33}}, & q_{R1} &= \frac{r_{32} - r_{23}}{4q_0}, \\ q_{R2} &= \frac{r_{13} - r_{31}}{4q_0}, & q_{R3} &= \frac{r_{21} - r_{12}}{4q_0}. \end{aligned} \quad (5)$$

Another representation of orientation is the Euler angle notation. This notation depicts the orientation as a successive rotation about three axes and defines the Euler angles as the three successive rotation angles [31]. According to [29], there are different conventions that determine the axes and rotation sequence. One possible convention is the $Z - Y' - X''$ convention, also known as Roll, Pitch, and Yaw. Here, the reference system A and the object system B initially lie on top of each other. Each of the following rotations is performed around the moving frame B , see Figure 3.2. The first rotation takes place around the z -axis of B (Z_B) by the angle α . After that, the second rotation takes place around the new y -axis of B (\hat{Y}_B) axis by the angle β and then the last rotation around the new x -axis (\hat{X}_B) by γ . Let φ be Yaw, θ be Pitch and

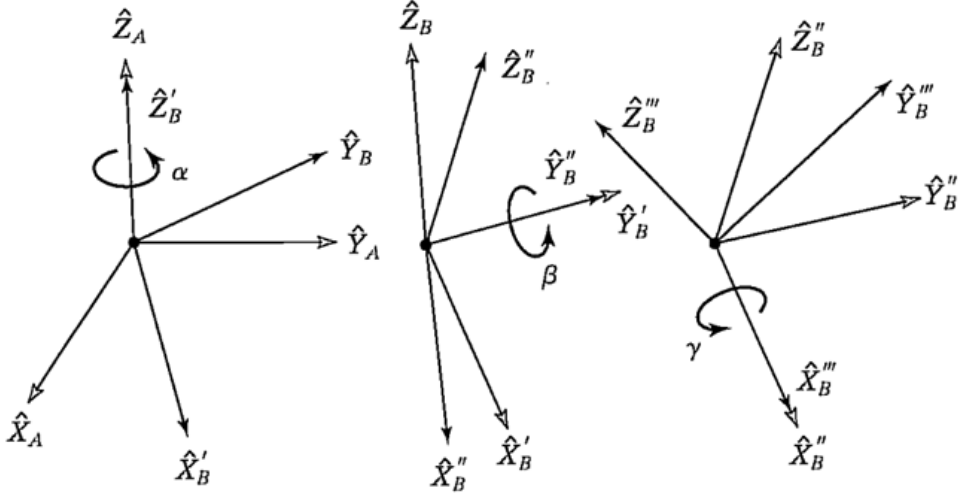


Figure 3.2: Illustration of the Roll, Pitch, and Yaw convention ($Z-Y'-X''$ convention). First, rotation of the object's coordinate system B around Z_B by the angle α (left). Second rotation of B around \hat{Y}'_B axis by the angle β (middle) and last rotation around \hat{X}''_B by γ (right).[29]

ϕ be Roll, then the rotation matrix is defined as

$${}^A_B R = \begin{pmatrix} \cos \varphi \cos \theta & \cos \varphi \sin \theta \sin \phi - \sin \varphi \cos \phi & \cos \varphi \sin \theta \cos \phi + \sin \varphi \sin \phi \\ \sin \varphi \cos \theta & \sin \varphi \sin \theta \sin \phi + \cos \varphi \cos \phi & \sin \varphi \sin \theta \cos \phi - \cos \varphi \sin \phi \\ -\sin \theta & \cos \theta \sin \phi & \cos \theta \cos \phi \end{pmatrix}. \quad (6)$$

A quaternion q can also be represented by the Euler angle notation. Let ϕ be Roll, θ be Pitch, and φ be Yaw, then the quaternion results in

$$\phi = \text{atan2} \left(2q_2q_3 - 2q_0q_1, 2q_0^2 + 2q_3^2 - 1 \right), \quad (7)$$

$$\theta = -\sin^{-1} (2q_1q_3 + 2q_0q_2), \quad (8)$$

$$\varphi = \text{atan2} \left(2q_1q_2 - 2q_0q_3, 2q_0^2 + 2q_1^2 - 1 \right). \quad (9)$$

These equations apply to Euler angles in the so-called aerospace sequence as defined by [32], which corresponds to the $Z - Y' - X''$ convention.[33]

3.2 Inertial Measurement Unit (IMU)

An IMU measures acceleration, orientation, angular velocity, and other gravitational forces. This electrical device consists of an triaxial accelerometer and a triaxial gyroscope. Sometimes, depending on the requirements, it also has a triaxial magnetometer installed. A triaxial sensor consists of three orthogonal sensors in order to be able to record translational and rotational movements, or the magnetic field strength, for all three spatial directions. There are the following types of IMUs: IMUs based on Fiber Optic Gyroscopes, Ring Laser Gyroscope IMUs and IMUs

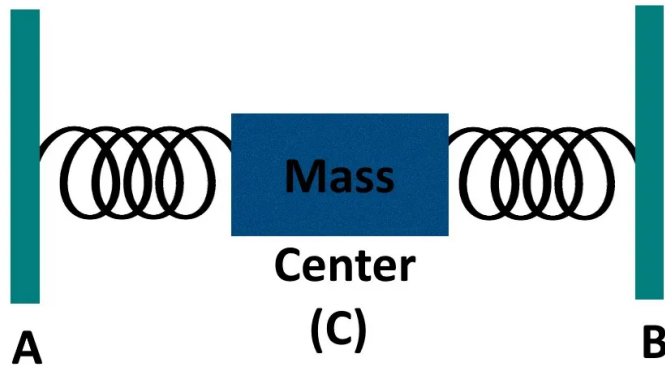


Figure 3.3: Illustration of a spring and mass system in a resting state. A and B (green): fixed Frame. C (blue): proof mass on a spring.[35]

based on MEMS technology [14]. This work will use IMUs based on MEMS technology. The following explains how the individual sensors, which are installed in an MEMS IMU, work.

Accelerometer

An accelerometer measures proper acceleration, i.e. the acceleration experienced relative to free fall, which people and objects experience [34]. The acceleration is measured in the unit m/s^2 . An accelerometer is conceptually a damped proof mass on a spring, see Figure 3.3. The system is damped so that vibrations of the mass and spring do not interfere with the required measurements. As soon as the accelerometer experiences an acceleration, the mass in the sensor accelerates slower than the rest of the sensor due to its inertia. This causes the mass to shift in the opposite direction of the acceleration. The mass shifts to the point where the spring can push/accelerate the mass with the same acceleration as the body of the sensor. Ergo, the magnitude of this displacement depends on the magnitude of the acceleration. Thus, it is possible to determine the acceleration by measuring the compression of the spring. Another approach to measure the displacement of the mass is by means of a capacitor. This capacitor consists of stationary/fixed plates and movable plates, which are attached to the mass or even replace it. If the movable plates shift, the capacitance C across the fixed and movable plate changes. This change in capacitance (like the compression of the spring) is proportional to how fast the sensor is accelerated.[35, 36]

Gyroscope

A gyroscope measures angular velocity using Coriolis acceleration. The Coriolis effect occurs due to rotation. It describes a force on an object moving on a rotating body and is directly proportional to the rotational speed. More specifically, the object moves toward or away from the axis of rotation of the rotating body. The Coriolis force accelerates this object in the direction perpendicular to its relative velocity and the axis of rotation according to the right-hand rule. The faster the object moves, the higher the acceleration due to the Coriolis force. A gyroscope

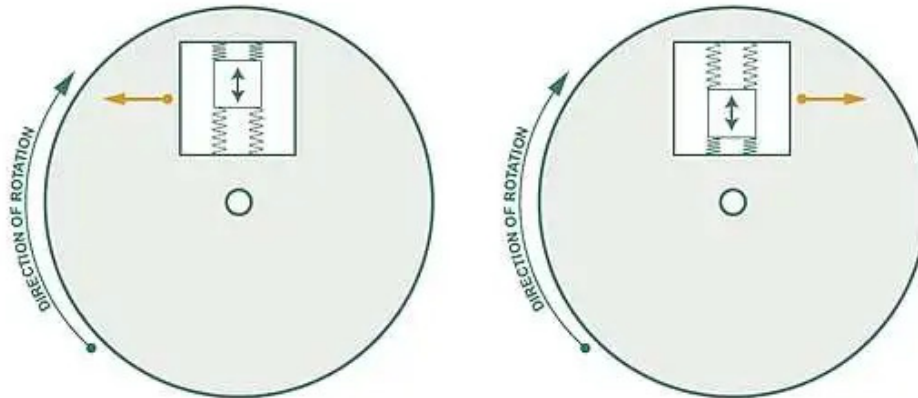


Figure 3.4: Illustration of the principle of operation of a gyroscope. Demonstration of Coriolis effect in response to a resonating mass (white box with arrow) suspended inside a frame (white space that contains the resonating mass)). Mass moving outwards (left) and back inwards (right). Orange arrows: Coriolis force applied to the rotating body (light green round plate).[37]

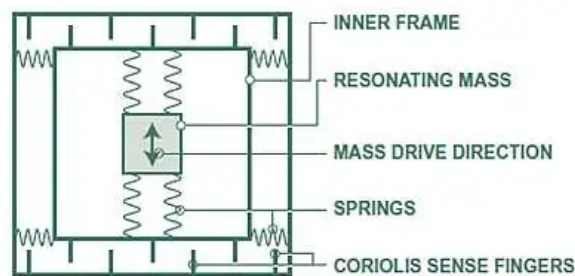


Figure 3.5: Schematic representation of the mechanical structure of a gyroscope.[37]

takes advantage of this effect by means of an oscillating mass that moves away from and toward the axis of rotation. The mass is attached to a frame with springs so that it can only oscillate in this direction. If the oscillating mass moves away from the axis of rotation on a clockwise rotating body, as shown in Figure 3.4, it experiences an acceleration to the right due to the Coriolis force. Thus, according to Newton's actio-reactio principle, the oscillating mass exerts a force on the rotating body to the left. Conversely, when the mass moves inward, it exerts a force to the right. To measure the Coriolis acceleration, the frame containing the oscillating mass is attached to the rotating body through springs at an angle of 90° relative to the resonant motion, as shown in Figure 3.5. Analogous to the accelerometer, capacitors measure the displacement of the proof mass, in this case the entire inner frame including the oscillating mass, by capacitive conversion. As the speed of rotation increases, the displacement of the inner frame also increases, which changes the signal derived from the corresponding capacitance.[37]

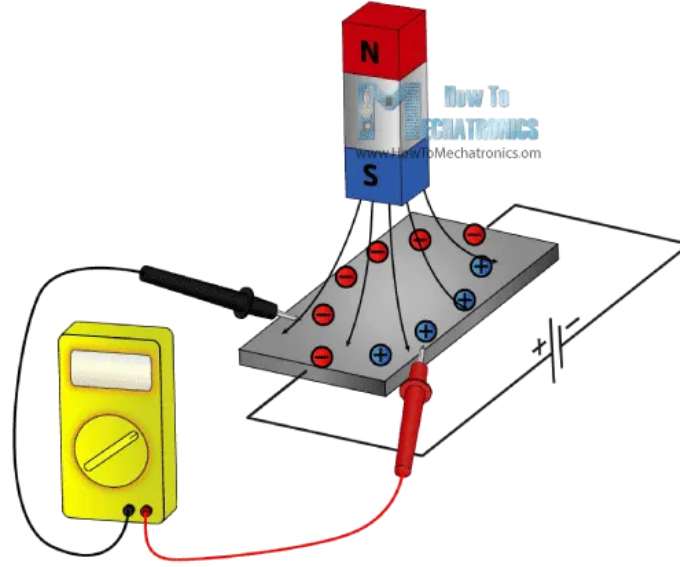


Figure 3.6: Concept of a MEMS magnetometer. A conductive plate (gray) with applied voltage is influenced by magnetic field (red and blue charged particles) from a Magnet. Generation of a voltage U_H proportional to the magnetic field strength. Measurement of this voltage with a voltmeter (yellow).[38]

Magnetometer

A magnetometer measures the earth's magnetic field using the Hall effect. Due to the Hall effect, a current carrying conductor builds up a voltage, called the Hall voltage, when he is in a homogeneous magnetic field. This voltage is perpendicular to both the direction of current flow and the direction of the magnetic field. Let I be the current flowing through the conductor, B the magnetic field strength, d the thickness of the conductor parallel to \vec{B} and R_H Hall constant depending on the material of the conductor then the Hall voltage U_H is calculated as

$$U_H = R_H \cdot \frac{I \cdot B}{d}. \quad (10)$$

A magnetometer measures the strength of the earth's magnetic field via the applied Hall voltage across its conductive plate, as depicted in Figure 3.6.[38, 39]

3.3 Madgwick Filter

Madgwick Filter by Sebastian O.H. Madgwick [33] is an orientation filter for IMUs consisting of triaxial gyroscopes and accelerometers, as well as for IMUs that additionally contain a triaxial magnetometer. He refers to IMUs that contain a magnetometer as Magnetic, Angular Rate, and Gravity (MARG) arrays. For the scope of this work, we continue to use the term IMU. The filter uses a quaternion representation of orientation, presented in 3.1, to describe the nature of orientation in three dimensions. The filter addresses the following challenges to compute an estimate of orientation by optimally fusing gyroscope, accelerometer, and magnetometer measurements.

- Gyroscopes are not suitable for providing absolute orientation alone, because the orientation determination is based on the integration of the gyroscope data. I.e., measurement errors lead to accumulating error due to the integration.
- Accelerometers and magnetometers provide absolute references for orientation due to the earth's magnetic field and gravity. However, they are likely to be subject to a high degree of noise. For example, motion of accelerometers distorts the direction of the gravity vector.

In the following sections, we describe the filter's functionality.

Orientation from angular rate

A triaxial gyroscope measures the angular velocity in x, y and z direction. These angular velocities are correspondingly denoted by ω_x , ω_y and ω_z and are defined as a vector by

$$\omega = \begin{pmatrix} 0 & \omega_x & \omega_y & \omega_z \end{pmatrix}. \quad (11)$$

Madgwick computes the orientation by numerical integration of the quaternion derivative. This requires that we know the initial conditions. Let ω_t be the angular rate measured at time t , $q_{\text{est},t-1}$ be the previously estimated orientation, $\dot{q}_{\omega,t}$ be the orientation derivative and Δt be the sampling period of the gyroscope, then we can calculate the orientation $q_{\omega,t}$ at time t with

$$\dot{q}_{\omega,t} = \frac{1}{2} q_{\text{est},t-1} \otimes \omega_t, \quad (12)$$

$$q_{\omega,t} = q_{\text{est},t-1} + \dot{q}_{\omega,t} \Delta t. \quad (13)$$

Orientation as solution of Gradient Descent

In a quaternion representation, a complete solution for orientation must be found. The formulation of an optimization problem achieves this. Here, an orientation of the sensor q matches any predefined reference in the earth frame, ${}^E d = [0 \ d_x \ d_y \ d_z]$, with the corresponding measured direction in the sensor frame ${}^S s = [0 \ s_x \ s_y \ s_z]$, by using a rotation operation. Therefore, we find q as the solution to

$$\min f(q, {}^E d, {}^S s), \text{ with} \quad (14)$$

$$f(q, {}^E d, {}^S s) = q^* \otimes {}^E d \otimes q - {}^S s. \quad (15)$$

To solve this optimization problem, Madgwick uses the gradient descent algorithm, because it is one of the simplest to both implement and compute. The gradient descent algorithm is based on an initial estimate q_0 and a step size μ . We obtain the n^{th} estimate of the orientation with

$$q_n = q_{n-1} - \mu \frac{\nabla f(q_{n-1}, {}^E d, {}^S s)}{\|\nabla f(q_{n-1}, {}^E d, {}^S s)\|}. \quad (16)$$

The objective function and its Jacobian define the gradient of the solution ∇f as

$$\nabla f(q_n, {}^E d, {}^S s) = J(q_n, {}^E d)^\top f(q_n, {}^E d, {}^S s). \quad (17)$$

Using IMUs with gyroscope and accelerometer, we assume by convention that the direction of gravity defines the vertical z -axis. I.e., the predefined reference in the earth frame is thus ${}^E d = {}^E g = [0 \ 0 \ 0 \ 1]$. The normalized accelerometer measurement ${}^S a = [0 \ a_x \ a_y \ a_z]$ replaces the corresponding measured direction in the sensor frame ${}^S s$ in the optimization problem. We obtain the function $f(q, {}^S a)$, which solves the estimation of the orientation using inertial sensors only (gyroscopes and accelerometers).

It works similarly with IMUs that use magnetometer. The magnetic field of the earth has a certain inclination depending on the location. Madgwick assumes that the reference orientation ${}^E d = {}^E b$ has only components in the vertical and in a horizontal axis. This reduces the reference magnetic vector to ${}^E b = [0 \ b_x \ 0 \ b_z]$. The sensor direction ${}^S s$ is the normalized data of the magnetometer ${}^S m_t = [0 \ m_x \ m_y \ m_z]$. From this we get $f(q, {}^E b, {}^S m)$ for the optimization problem. For IMUs with magnetometer, we combine the measurements and reference directions of gravity and magnetic field. Therefore, we get $f(q, {}^S a, {}^E b, {}^S m)$. For this, a solution has a minimum defined by a single point, as long as the northern magnetic intensity is defined ($b_x \neq 0$).

We calculate the estimated orientation q_{∇} using the gradient descent algorithm. This requires a previous estimate of the orientation $q_{\text{est},t-1}$ and the target function gradient from the accelerometer and magnetometer data ∇f . The type of sensors used defines ∇f . Let $q_{\text{est},t-1}$ be the previously estimated orientation, ∇f be the objective function gradient and μ_t be the step size, then we calculate the estimated orientation at time t , $q_{\nabla,t}$, with

$$q_{\nabla,t} = q_{\text{est},t-1} - \mu_t \frac{\nabla f}{\|\nabla f\|}. \quad (18)$$

An optimal value of μ_t ensures that the convergence rate of $q_{\nabla,t}$ is limited to the physical orientation rate.

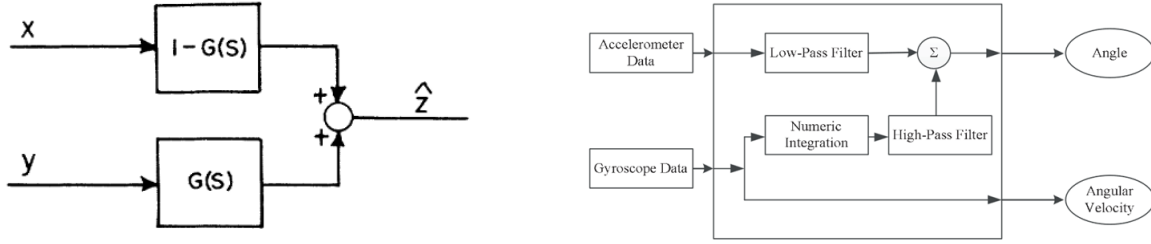
Fusion algorithm

To combine the orientations of the gyroscope and the gradient descent algorithm, Madgwick uses a weighted fusion of the orientation calculations. Let $q_{\nabla,t}$ be the estimated orientation from the gradient descent algorithm, $q_{\omega,t}$ be the estimated orientation from the gyroscopes and γ_t be the weight, then we compute the estimated orientation of the sensor frame relative to the earth frame $q_{\text{est},t}$ as

$$q_{\text{est},t} = \gamma_t q_{\nabla,t} + (1 - \gamma_t) q_{\omega,t}, \quad 0 \leq \gamma_t \leq 1. \quad (19)$$

3.4 Complementary Filter

The Complementary Filter, proposed by Colton [40], generates an estimate \hat{z} from two noisy measurements, x and y , of a signal z . Assume that the noise in y is primarily high-frequency and the noise in x is mostly low-frequency. The Complementary Filter uses a low-pass filter $G(s)$ to filter out the high frequency noise in y . Thus, the complement of $G(s)$, $[1 - G(s)]$, is a high-pass filter, that filters out the low frequency noise in x . [41] Figure 3.7a shows this basic structure of the Complementary Filter.



(a) General approach of a complementary filter for signal estimations. Low-pass filter $G(s)$ for x with mostly low-frequency noise, and high-pass filter $[1 - G(s)]$ for y with primarily high-frequency noise, results in a signal estimation \hat{z} . [41]

(b) Complementary Filter Algorithm according to [42] using the data of an accelerometer and a gyroscope for orientation estimation. Low-pass filter for the accelerometer data and high-pass filter for the integrated data of a gyroscope.

Figure 3.7: Block diagrams of the Complementary Filter. General approach (left) and orientation estimation using accelerometer and gyroscope (right).

Regarding the orientation estimation using IMUs, the Complementary Filter applies the low-pass filter to the data from the accelerometer and the high-pass filter to the integrated gyroscope data, see Figure 3.7b. Let θ_{angle} be the Euler angle (Roll or Pitch), α the filter coefficient, ω the measured angular velocity of the gyroscope, a_{acc} the angle obtained through the data from the accelerometer and dt the sampling interval, then the mathematical model of the Complementary Filter is

$$\theta_{angle} = \alpha \cdot (\theta_{angle} + \omega dt) + (1 - \alpha) \cdot a_{acc}. \quad (20)$$

The low-pass filter eliminates short-term fluctuations and allows only long-term changes to pass. Applied to the accelerometer, it only lets the long term angle estimate through and filters out unwanted noise of the data. The high-pass filter does the same for long term variations. It passes only the short term signals from the gyroscope, but filters out the accumulating error/drift. Thus, the Complementary Filter takes advantage of each sensor. [42]

3.5 Spherical Robot Types

Spherical robots belong to the mobile robots. Due to their spherical shape, they have some advantages over other mobile robots. For example, it is possible to design them holonomic, thus the controllable degrees of freedom are equal to the total degrees of freedom, or to completely seal them off from hazardous environments with the shell. In addition, they can overcome certain obstacles or recover from collisions with obstacles quickly and non-destructively. These characteristics make spherical robots suitable for tasks in space, underwater, snow, and other challenging environments, or for swarm applications. It even allows the robot to be dropped. [43]

Spherical robots are distinguished by their methods of propulsion and are divided into two main groups. Those that use the displacement of a robot's center of gravity (the barycenter) to produce a desired motion, and those with other approaches to motion. The group that uses **barycenter offset** for motion includes the following types:

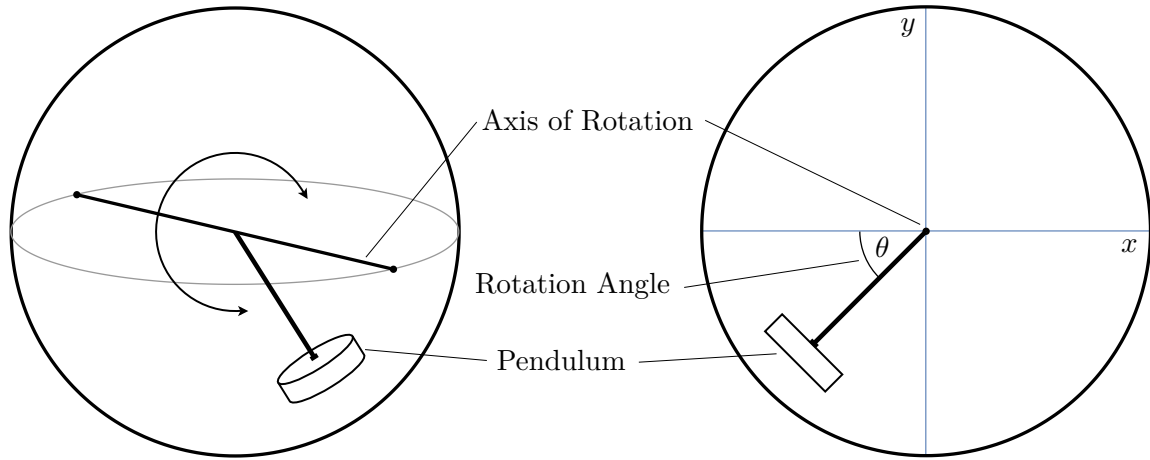


Figure 3.8: Spherical robot (black circle) with pendulum mechanism. Schematic representation according to [43, 44] from the slanted view (left), and side view including the robot's BCS (right).

Pendulum Based

First, there are the pendulum based robots as shown in Figure 3.8. In this type of spherical robot, a pendulum including a pendulum body is attached to a horizontal axis that passes through the center of the outer shell of the robot. The pendulum can rotate around this axis, as well as shift left or right along the axis. As the pendulum rotates, the center of mass shifts outward from the center and the shell begins to roll. On the other hand, shifting the pendulum causes a rotation in the corresponding direction [43, 44]. Many variants of pendulum based robots exist, such as the Roball [45] or the Groundbot [46]. Some designs even use the concept of two pendulums, as for instance the work presented in [47, 48].

Regarding the placement of IMUs, since the pendulum rotates around the axis of rotation, it is not possible to attach an IMU in the x - y -plane as shown in Figure 3.8. Furthermore, due to the translation of the pendulum along the axis of rotation, only limited positioning is possible here as well. Thus, the IMUs can be placed in the shell or on the rotation axis outside the pendulum's shift.

IDU

A spherical robot with an IDU moves similarly to the principle of locomotion based on a pendulum. Here, the movement of the internal vehicle changes the position of the center of mass of the overall system. The concept of an IDU is wheel based, thus it derives the propulsion from a wheel in contact with the bottom of the sphere. There are generally speaking three types of IDUs. First, there is the **hamster ball**, see Figure 3.9, where an internal car resting at the bottom of the sphere serves as the drive mechanism. This internal car is a small-wheeled robot, whose weight provides enough force to propel the robot when it moves. In addition to the hamster ball, another design is the **spring-loaded IDU**. Here, a rod and a spring are attached to the top of the internal robot and press against the shell. This ensures that the wheels must be in constant contact with the shell. To ensure the movement of the spring along the shell,

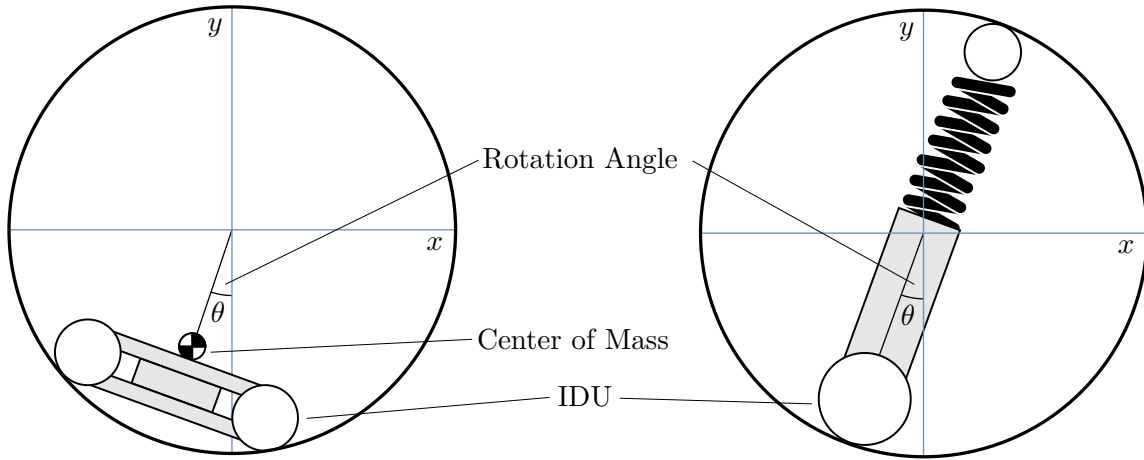


Figure 3.9: Spherical robot (black circle) with IDU. Hamster ball (left) according to [51] and spring-loaded IDU (right), both including the robot's BCS.

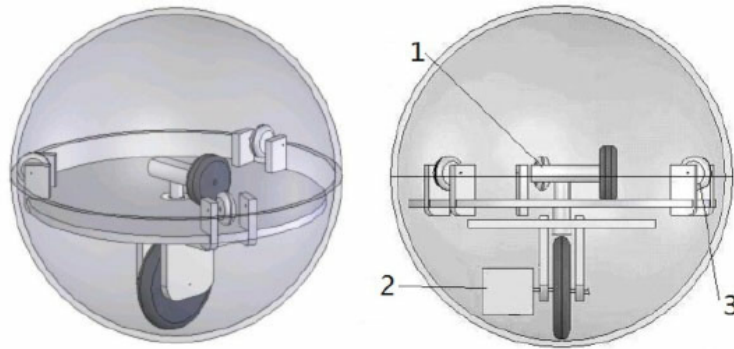


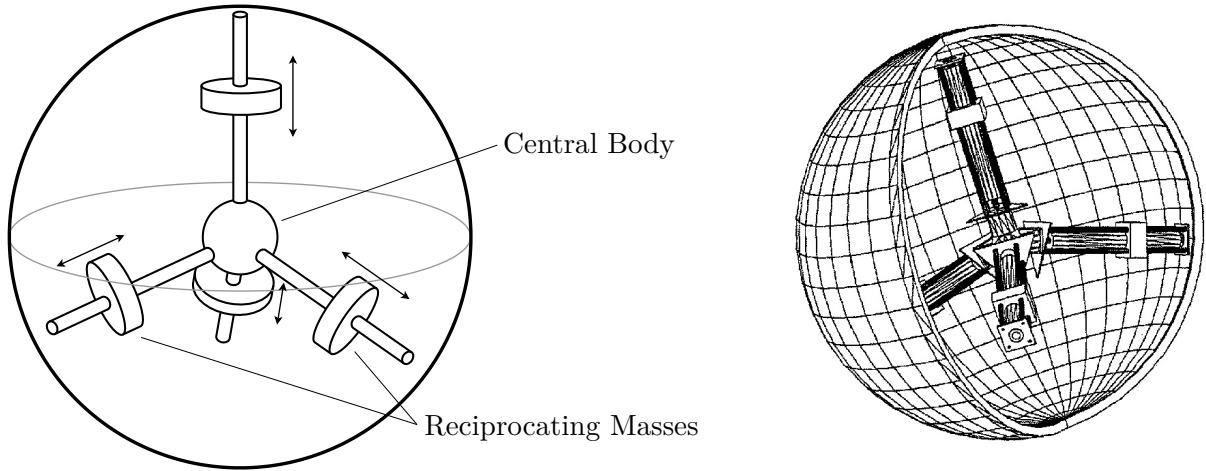
Figure 3.10: Structure of the BHQ-3 Design by Zhan [49]. Example of an universal wheels robot.

a ball bearing with 3 DOF is attached to the upper end of the spring. Figure 3.9 shows this design. The last type of the barycenter offset group is the **universal wheel**. It is a combination of the hamster wheel and the spring-loaded IDU. The IDU can rotate freely because of the combination of wheels inside the robot. Two motors control the inner drive mechanism, one motor controls the orientation of the IDU and one motor controls the speed of the drive wheel. Examples of universal wheels robots are BHQ-3 [49], see Figure 3.10, and the HIT Spherical Robot [50]. [43, 44]

For the use of Zevering's orientation determination, the IMUs must at least rotate with the shell. Therefore, in the case of IDU robots we can only place the IMUs in the shell, since the IDUs rotates independently of the shell.

Shifting Masses

Like the two types before, robots using the principle of shifting masses' actuator is the displacement of its center of gravity. Here, shafts connect the central mass to the shell, as seen in



(a) Concept of an spherical robot (black circle) using the shifting masses (cylinders with arrows) principle according to [52].

(b) Exemplary design for a robot with shifting masses by Mojabi [54].

Figure 3.11: Spherical robot with shifting masses mechanism.

Figure 3.11. In addition to the central mass, special weights are attached to the shafts, which can traverse along them. By redistributing these masses, the spherical robot can move in any direction. However, the central mass can also be the robot's payload.[52, 53]

In a shifting masses robot, it is not possible to locate the IMUs in the center or within reach of the reciprocating masses. Therefore, we place them either on the very outside, in the shell, or on any other axis at any distance from the center.

Besides the group that uses the displacement of the barycenter for locomotion, there are the following **other types**:

Shell Transformation

A more recent idea for locomotion is shell transformation. Here, instead of a complicated internal mechatronic system to drive the sphere, the outer body of the robot is deformed [44]. There are many different implementations for this type, including designs that use a dielectric elastomer actuator, see Artusi [55], or pressurized air bladders, such as presented by Wait [56]. For the design by Wait see Figure 3.12.

But there are other approaches, like Sugiyama's [57]. He uses pulse width modulation to manipulate four rings, which connect in the middle with a wire made of a metal alloy. This changes the shape of the sphere and allows the robot to take different shapes, as shown in Figure 3.13, to move around.

In terms of the placement of IMUs, it is difficult to make a general statement for robots that use shell transformation. Since the shell serves as an actuator, no placement is possible here. The positioning of the IMUs depends entirely on the internal structure of the robot. It therefore varies with the specific design and shell forming approach.

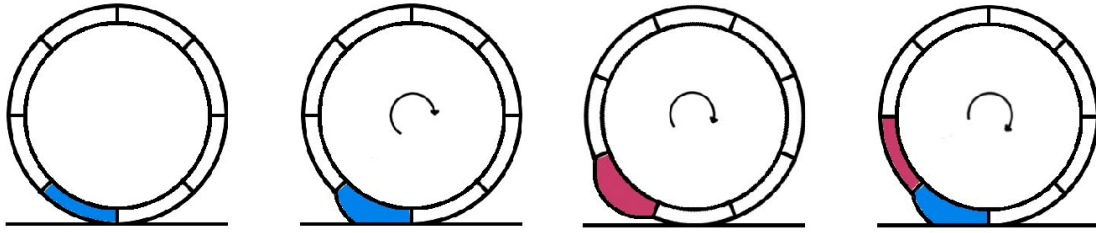


Figure 3.12: Cross-section of a shell transforming spherical robot (black circle) with pressurized air bladders in motion by Wait [56]. Blue: inflating air bladder. Red: deflating air bladder.

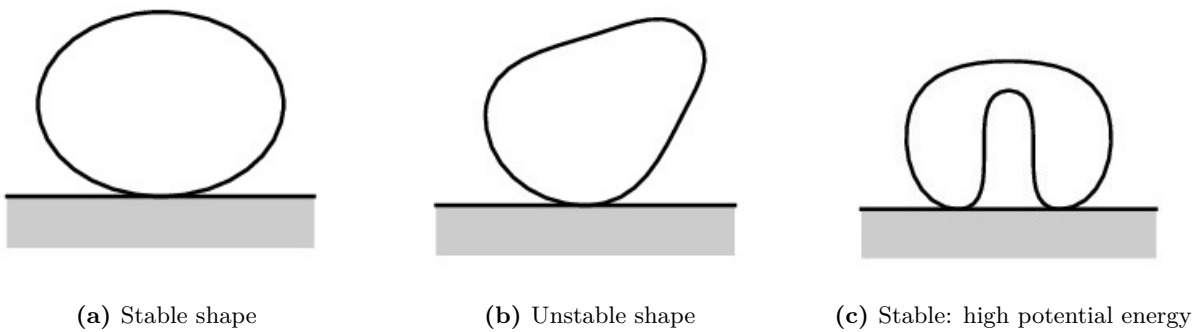


Figure 3.13: Cross-section of spherical robot with deformable shell (black) in different stages.[57]

Reaction Wheels

Another approach to spherical robot locomotion is to use reaction wheels. Here, the laws of conservation of angular momentum are used to control the movement of the robot by rotating a large flywheel quickly about an axis. To date, several designs using flywheels exist.[44] One example of a robot with reaction wheels is the Gyrover, presented in [1, 58]. The Gyrover has rather the shape of a disk, see Figure 3.14 balancing on its edge thanks to a gyroscope. The effect of the precession moment is used for steering. Other designs use two pairs of diametrically opposed control moment gyroscopes, such as the design by Joshi [2] as seen in Figure 3.15. To rotate the robot, the angular velocity of one pair is increased. This causes the shell to rotate in the opposite direction to maintain the total angular momentum of the system.

Analogous to shell transforming robots, the positioning of IMUs for robots that use reaction wheels depends on the internal structure. Since there are many different possible designs, we must place the sensors specifically for each individual robot.

Rod-Driven Locomotion

A rod-driven robot essentially consists of two similar disks containing the rod stars and a slightly larger center disk. Supports connect these disks, see Figure 3.16 for a technical sketch. There are two ways to make the robot move, as shown in Figure 3.17. The first way to create a rotation

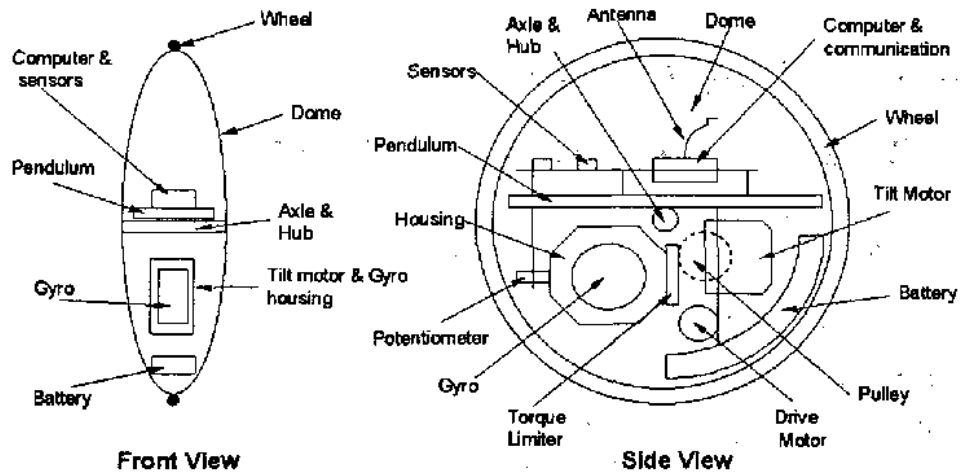


Figure 3.14: Component diagram (left) and a side view (right) of the Gyrover.[1]

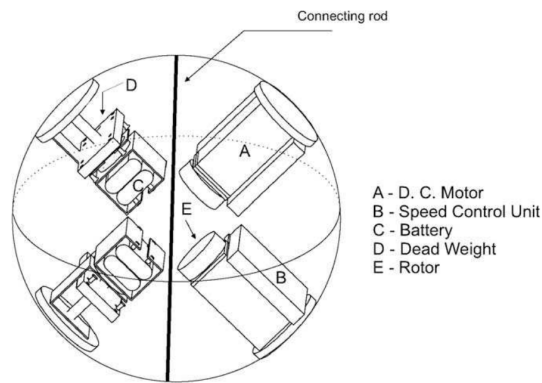


Figure 3.15: Internal structure of Joshi's spherical robot using reaction wheels.[2]

is to push against the ground by extending the rods. The second way is to use leverage. Here, the rods extend along the rolling direction and generate a torque due to their mass.[3]

As for the placement of IMUs, it is possible to put them on the entire middle disk, as well as in the space between the disks. Thus, the positioning in the center is a possibility, as well as the placement in the shell.

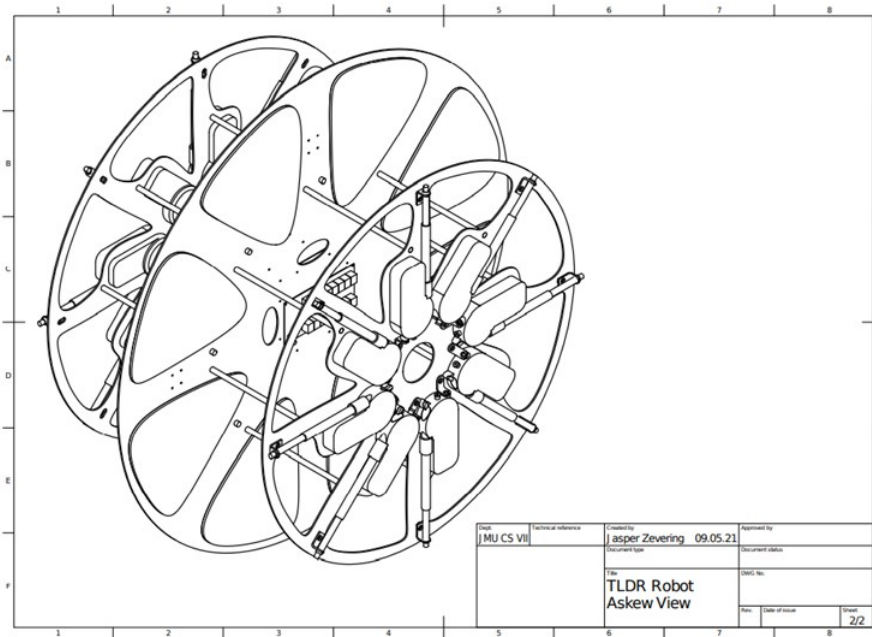


Figure 3.16: Blueprint of the rod-driven robot without the spherical shell.[3]

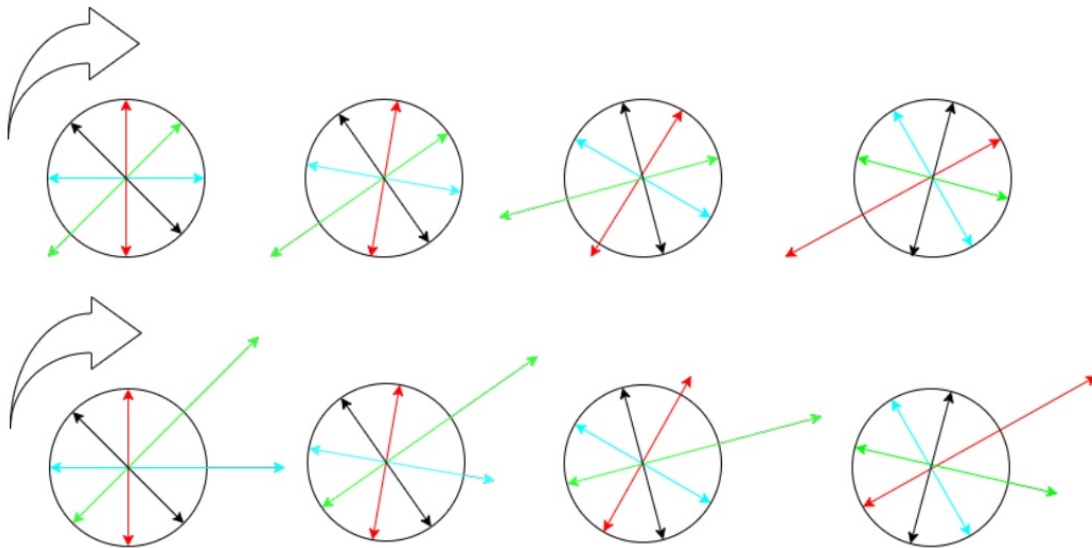


Figure 3.17: Illustration of the locomotion principles of rod-driven robots (black circle). Rotation by push (above) and rotation by leverage (below) for rod-driven robots [3]. Arrows: rods, color coded for motion indication.

Chapter 4

Theory

For the purpose of evaluating different IMU configurations for the various spherical robot types, presented in Chapter 3.5, we first define a general approach for possible IMU architectures. Furthermore, we state restrictions and initial theses for the scope of this work. Then, we define an approach specific to the different types of spherical robots, from which we later derive the experiments to be performed.

4.1 General Approach

Since this work is concerned about the number and placement of IMUs, the focus is on the benefits provided by stochastic error and spatial diversity, as introduced in Chapter 2. Regarding the quantity of IMUs, we expect an exponential decreasing trend of the RMSE based on [13, 16–18]. Depending on the number of IMUs n , we assume the RMSE will follow the form of

$$RMSE \sim \frac{1}{\sqrt{n}}. \quad (21)$$

According to [23], the data of a gyroscope is independent of the placement of the sensor. It follows, that the placement of the gyroscopes does not affect the orientation determination. In contrast to this, the accelerometer and magnetometer data depends on the placement of the sensors. The filter we use, presented in 2.2, does not use magnetometers. Since gyroscopes and accelerometers are both built into an IMU, the orientation determination depends on the placement of the IMUs. We presume that an IMU in the center of the sphere determines the orientation more accurately than an IMU placed off center. This assumption is based on the fact that the accelerometers in the center of the sphere do not experience significant height differences when the sphere is moving. Thus, they do not measure accelerations other than the acceleration from the motion of the entire sphere. If we place the IMUs outside the center of the sphere, the accelerometers will rotate along with the sphere and hence sense centripetal forces as well.

When placing the IMUs, we use mainly equal distances to the center or rather between the IMUs, since optimal configurations have the shape of polygons or polyhedra according to [21]. The relative orientation of the individual IMUs is irrelevant for the optimality of the system

as stated by [16]. We include the placement of the IMUs in the data merging process. Thus, an arbitrary placement regarding the orientation of each IMU within the sphere boundaries is possible without losses in the quality of the data due to peculiarities of the specific positions. For the scope of this thesis, we locate the sensors only on the rotation axes, ergo an orthogonal arrangement as recommended by [16], to limit the complexity and the extent of this work. Furthermore, according to [24], it is possible to measure the angular velocity of the body using four non-coplanar IMUs, each with a triaxial accelerometer. Although we use the filter presented by [25] for orientation determination, thus using gyroscopes for the angular velocity, we consider the configuration of four non-coplanar IMUs to be worth an experiment.

4.2 Specific Approach

From the various spherical robot types, presented in Chapter 3.5, we conclude the following configurations. For pendulum based robots, it is important to determine first whether the sensors are best placed on the very outside of the spherical robot, ergo in the shell, or closer to the center on the axis of rotation of the pendulum. It is therefore necessary to determine the accuracy of the orientation determination as a function of the distance of the IMU from the center. We place the IMUs on the rotation axis of the pendulum in case the IMU gives better results closer to the center. Since it is not possible to place the sensors in the center, we either put the IMUs on this axis on one side or on opposite sides of the pendulum/center of the sphere. Thus, an experiment that determines the symmetry in the placement of the IMUs on a single axis is necessary. For the other case, that the IMUs provide better results on the very outside of the spherical robot, the resulting situation is the same as for robots with an IDU, because for those spherical robots, the placement of the sensors is only possible in the shell. We can set up the following placement options for the IMUs on the very outside of the spherical robot, taking into account the limitations already established. Since according to [10] only one non-centered IMU leads to lower quality measurements, we want to determine whether three IMUs, one on each axis of rotation, give similar accurate orientation estimations as three IMUs located in the center. It is also possible to mount two sensors on opposite sides of an axis. If the symmetrical placement of the sensors proves advantageous, is an arrangement of six IMUs (two on each axis on opposite sides of the sphere's center) more accurate than all of them in the center? This again results in the necessity of a experiment regarding the symmetry. A similar situation applies to spherical robots with shifting masses. Since it is not only possible to locate the IMUs in the shell, but also inside the sphere out of reach of the reciprocating masses, we further consider the distance to the center here. For the rod-driven robots, a placement for the IMUs in the center, as well as on all three axes in any distance from the center is possible, except for where the disks are installed. Since there are hardly any restrictions regarding the placement of the IMUs, the following question arises in addition to those we already posed. Is there an advantage in using four coplanar IMUs, for example a combination of center and one on each axis, as stated by [24]? It is possible to transfer this general approach for the IMU placement, and thus indirectly the quantity, to the robots that use reaction wheels or shell transformation. Here, it is necessary to place the sensors specifically for each individual robot, since no general restrictions regarding the placement exist. For the specific robots, depending on the constraints on the placement of

the IMUs, one has to find a suitable configuration using the results of this work.

The focus of this work is on the impact of IMU placement configurations on orientation determination. It does not serve the purpose of investigating the effect of IMU clusters, as e.g. the work of Greenheck [18] and Crain [17]. Therefore, the maximum number of IMUs for a configuration is six, since we do not need a higher number of IMUs to answer the above-mentioned questions about the accuracy of the configurations with respect to the orientation determination. Another factor is the limitation of the scope and cost of this work.

Chapter 5

Experiments and Evaluation

In this chapter, we first provide an overview of the technical setup for the experiments. This is followed by the performance of the experiments. Finally, we compare and discuss the results of the experiments carried out.

5.1 Technical Setup

Here, we present the components used to perform the experiments. First, we introduce the used IMUs and the system, as well as the algorithm we use to obtain the ground truth. In the peripheral part, we present the construction for mounting the IMUs in the sphere, as well as the microcontroller. Lastly, we specify how to get the orientation from the measured data of the IMUs.

5.1.1 Inertial Measurement Unit (IMU)

For this work, we use six PhidgetSpatial Precision 3/3/3 High Resolution 1044_1 IMUs. They comprise an acceleration, rotation rate and magnetic field sensor with three axes each. Chapter 3.2 explains the functionality of this sensor system. The PhidgetSpatial Precision 3/3/3 High Resolution 1044_1 works with a data recording rate of 250 Hz and has enhanced precision in the accelerometer when measuring less than ± 2.5 g, and enhanced gyroscope precision at speeds less than $100^\circ/\text{s}$.^[59]

5.1.2 Ground Truth

In order to evaluate the data from the IMUs we require an exteroceptive sensor to provide ground truth measurements of absolute orientation to compare the estimated orientation from the IMUs. For this purpose, we use the Optitrack V120 Trio 330694 [60]. This model has a resolution of 640×480 , for each of the three cameras, and a frame rate of 120 Frames per Second (FPS). The cameras capture the reflective markers on the observed body and the Motive:Tracker software combines them into so-called rigid bodies. Then a Virtual Reality Peripheral Network (VRPN) Client Robot Operating System (ROS) [61] publishes the position and orientation of these rigid bodies via ROS topics.

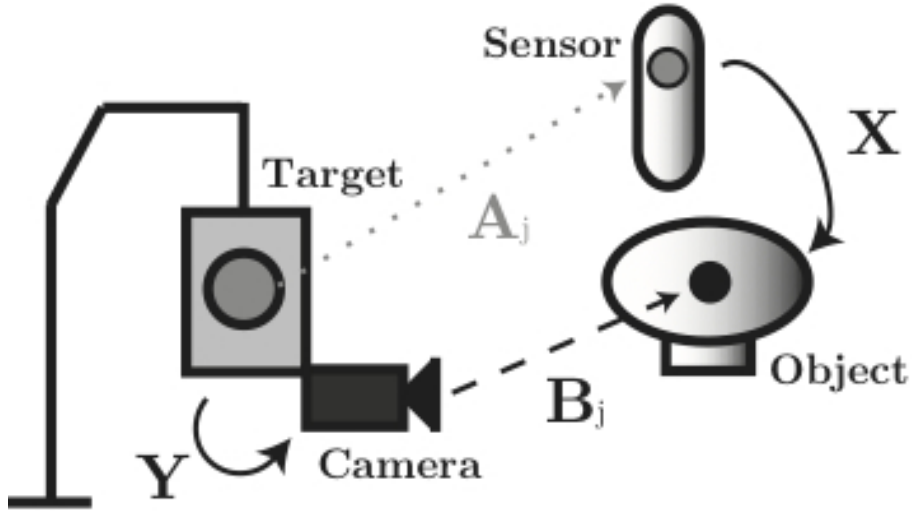


Figure 5.1: Exemplary experimental setup with two sets of 6 DOF data. Data gathered from system A (A_j , here: sensor) and from system B (B_j , here: camera). Leaves two unknowns (black arrows, X : transformation between sensor and object, and Y : transformation between target to camera). [62]

Since the data from the Optitrack system is not given in the same coordinate system as the data from the IMUs, it is necessary to perform a coordinate transformation in order to compare the datasets directly. Therefore, we have two sets of 6 DOF data collected by two independent systems, A (IMUs) and B (Optitrack). As seen in Figure 5.1, this problem leaves two unknowns in this setup, Y and X , and has the form of

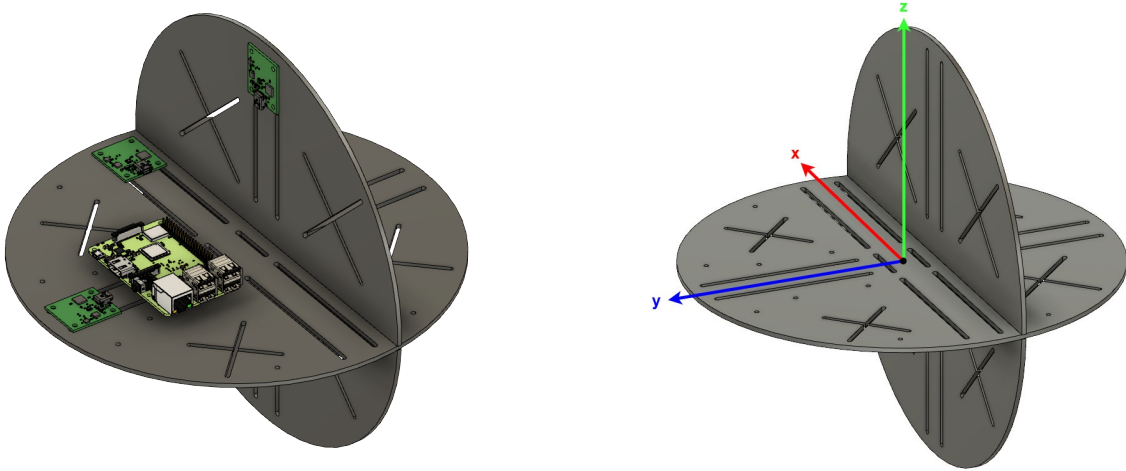
$$AX = YB. \quad (22)$$

For this work, we will use [62] to solve this problem and to transfer the results from the Optitrack system into the IMU's coordinate system. For further information, refer to [63].

5.1.3 Periphery

In order to allow the adjustable attachment of the IMUs to the rotary axes of the sphere, we use the mounting as shown in Figure 5.2 using 3D CAD software. The software used is Fusion360, developed by the company Autodesk.

The construction consists of two interlocking plates laser cut from perspex. The base plate, see Figure 5.4 for technical sketch, is the slightly bigger plate and comprises the x - and y -axis. The small plate contains the z -axis. Figure 5.5 displays the technical sketch for the small plate. The slits, one next to the x -axis rail for the IMUs in the base plate and the other one on the small plate, are for interlocking the two plates. The slit on the base plate has an offset by 22 mm from the center. We overcome this distance with standoff hexagonal spacers when mounting the IMUs on the plates. Furthermore, the base plate is lowered by 5 mm, so that the IMUs are at the height of the center when attached, hence the 5 mm offset of the small plate's slit for the base plate. The x-shaped cutouts and the holes in the plates are mainly for mounting the



(a) Exemplary mounting of 3 IMUs (one on each positive rotation axis) and the Raspberry Pi on the construction.

(b) Illustration of the Base Coordinate System (BCS) of the sphere.

Figure 5.2: Mounting for the IMUs as CAD Model.



Figure 5.3: Picture of the real mounting for the IMUs.

Optitrack balls, and give the option to attach further modules, such as the power supply. For more stability of the construction, we glue the two plates together using superglue.

The mounting is embedded in a plexiglass sphere with an inner diameter of 28.3 cm. Figure 5.3 shows the actual construction with open shell. We define the coordinate system of the sphere, called the BCS, as presented in Figure 5.2b. We attach the Optitrack balls to the small plate with the tripod and the microcontroller as shown in Figure 5.3.

A Raspberry Pi 3 microcontroller is the main processing unit, see Figure 5.2a for attachment onto the base plate. The used Raspberry Pi 3 model B has a Quad Core 1.2 GHz Broadcom BCM2837 64 bit CPU and 1 GB RAM. Furthermore, it is equipped with 4 USB ports for communicating with and providing power for the IMUs.[64] To attach more than four IMUs we use a Universal Serial Bus (USB) 3.2 GEN1 Hub with four ports and extra power supply. We run an Ubiquiti image [65] on the Raspberry Pi. This image has preinstalled ROS packages and starts up a WiFi hotspot by default, allowing a connection via Secure Shell (SSH).

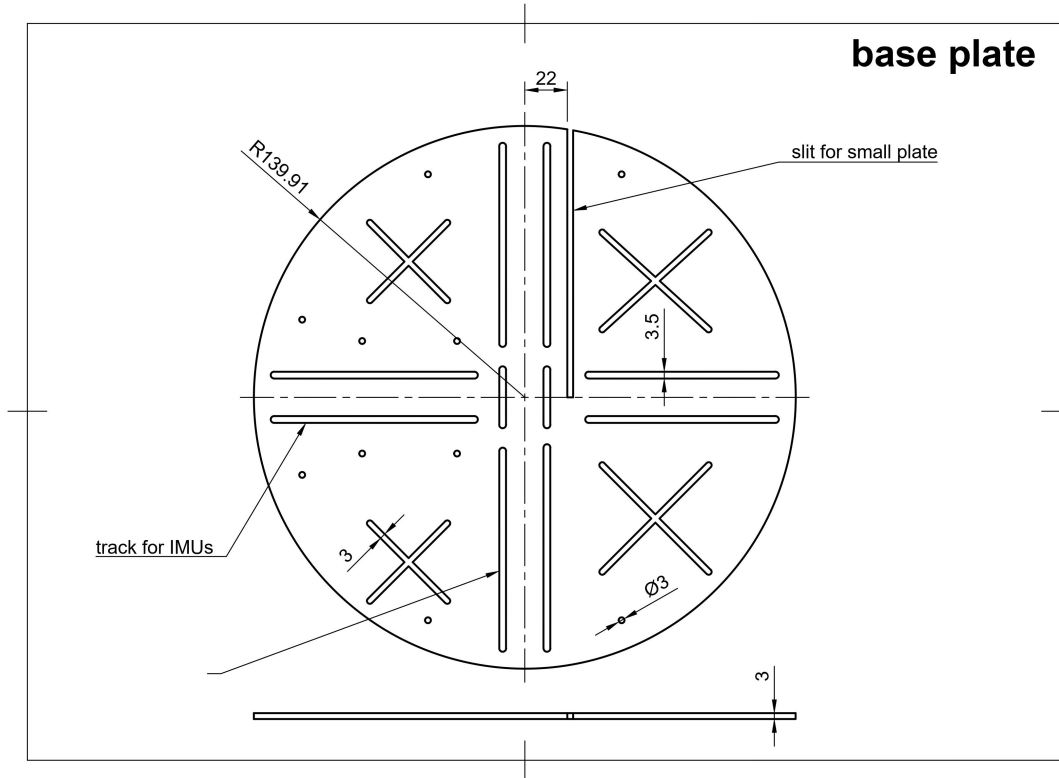


Figure 5.4: Blueprint of the base plate in scale 1:2.

5.1.4 Orientation Determination

We determine the orientation by using a filter combination of the Madgwick and the Complementary Filter as presented in [25], see IMU-based pose-estimation for spherical robots in Chapter 2.2. Therefore, it is necessary to first retrieve and combine the data of the individual IMUs. A Phidget Manager performs this task. He handles the detection and management of available Phidgets and saves the attached Phidgets in a hash map/unordered map. We use this dynamic data structure because it can insert and delete objects faster and performs slightly better at accessing known elements than an ordered map [66]. The Phidget Manager stores the attached Phidgets in the map as struct *imu* objects. The *imu* struct comprises the following:

- **Phidget Spatial Handle:** This spatial channel is responsible for aligning simultaneously data from the accelerometer, gyroscope, and magnetometer.
- **Spatial Number:** The spatial number enumerates the IMUs in the order they are attached.
- **Internal Values:** Here we store the measured values of the IMU both as positive and negative values.
- **Pointer:** The pointers assign the correct internal values to the BCS of the sphere.

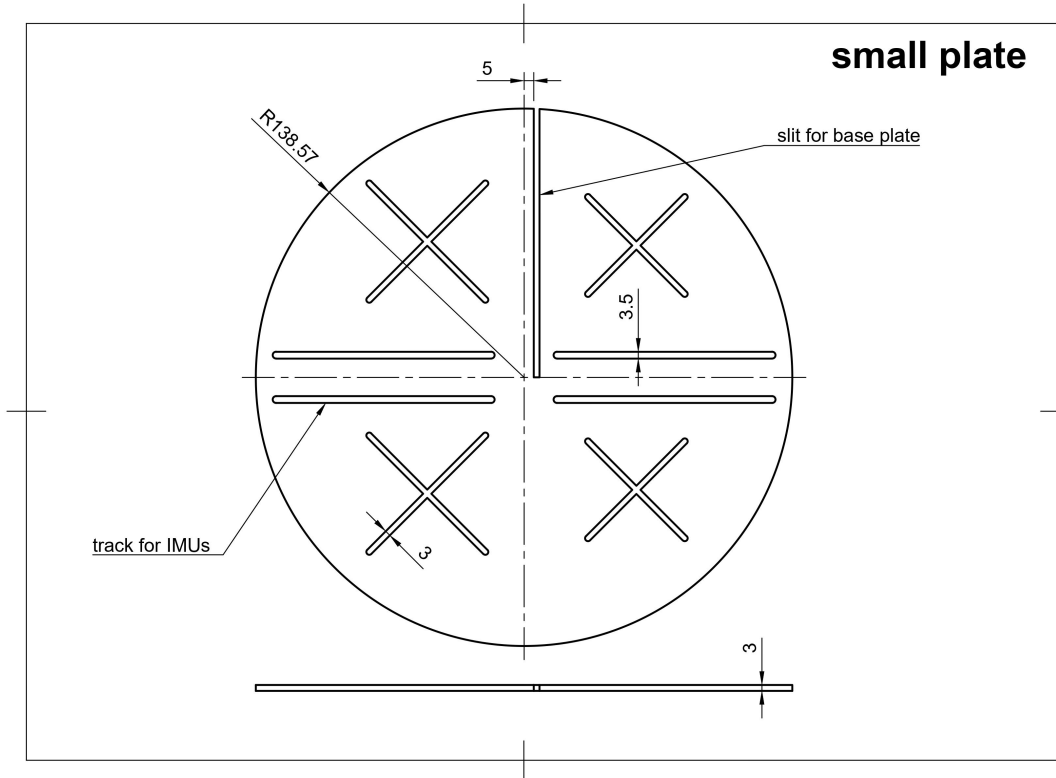


Figure 5.5: Blueprint of the small plate in scale 1:2.

- **Axis Configuration Array:** This array stores the coinciding internal axis for each axis of the BCS of the sphere. This allows a simple pointer assignment and especially facilitates the saving and loading of the configurations from YAML files.

The map uses the unique serial number of the IMUs as a key. This enables easy access to the *imu* object by serial number for each event the IMU sends. When we attach an IMU, it sends an attach event that the Phidget Manager's attach handler registers. The attach handler creates a matching spatial channel with the serial number in a new *imu* object and waits for the virtual channel to connect to the physical one. Responsive to the virtual channel being connected to the physical one, the attach handler stores the created *imu* object in the hash map. Similarly, in the instance of a detach event, the Phidget Manager's detach handler closes and deletes the corresponding spatial channel of the *imu* object via the serial number and removes the *imu* object from the hash map.

The function for combining the raw data is now able to iterate through the hash map with for-each-loops to combine the gyroscope and accelerometer values of the IMUs. It accesses the values via the pointers gx , gy , gz , ax , ay and az , since we need the values in the respective base direction. To combine the accelerometer data, we use the arithmetic mean. Let $a_k(t)$ be the acceleration in direction k at time t with $k \in \{x, y, z\}$, $a_{ki}(t)$ be the measured acceleration in k direction of the i^{th} IMU and n be the number of attached IMUs, then we calculate the new

$a_k(t)$ with

$$a_k(t) = \frac{\sum_{i=1}^n a_{ki}(t)}{n}. \quad (23)$$

For the gyroscope, we add the new data to the existing data and take the arithmetic mean from it. Let $g_k(t-1)$ be the previous-determined angular velocity in direction k with $k \in \{x, y, z\}$, $g_{ki}(t)$ be the measured angular velocity in k direction of the i^{th} IMU at time t and n be the number of attached IMUs, then we calculate $g_k(t)$ with

$$g_k(t) = \frac{g_k(t-1) + \sum_{i=1}^n g_{ki}(t)}{n+1}. \quad (24)$$

The axis configuration array assigns the pointers for each IMU to the respective BCS axis. There are two options for assigning the corresponding values to this array, either by loading a YAML file or by a dynamic allocation. In the case of dynamic allocation, we first determine the z -axis using the gravity vector, by aligning the sphere with the BCS z -axis pointing upwards. Then, by rotating around the Roll axis (BCS x -axis), we find the corresponding internal axis for each IMU using the gyroscopes. The right-hand rule [67] defines the last axis. For the assignment of the inner axes to the base axes, we specify that all IMUs, or rather their orientations, are offset from the BCS's orientation by any number of 90° rotations. Using the save configuration option, it is possible to save the axis configuration arrays in a YAML file after the dynamic allocation.

5.2 Experiments

Based on the approach from Chapter 4, we set up the following experiments:

- In our first experiment, **Experiment A**, we review the relationship between the number of IMUs and the RMSE, as the equation 21 states. In this experiment, we place different numbers of IMUs in the center of the sphere. Figure 5.6 shows schematically the sphere with an increasing number of IMUs in the sphere's center. Thereby, we do not test a fixed placement yet.

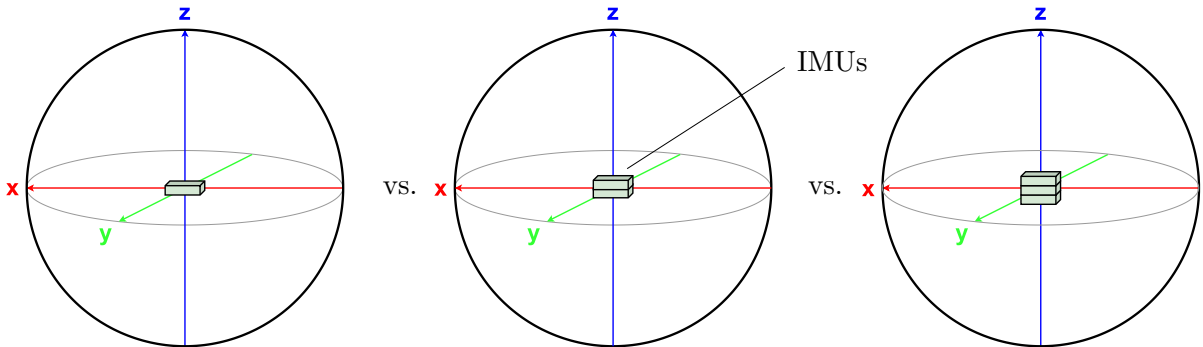


Figure 5.6: Experiment A: Number of IMUs. Schematic of a spherical robot (black circle) including its BCS with (from left to right) increasing number of IMUs in the center.

- The second experiment, **Experiment B**, serves to determine the dependency of the orientation determination accuracy on the distance of the IMU from the center of the sphere. For this purpose, starting from the center of the sphere, we move the IMU gradually outward along a chosen axis by a predefined distance d to the edge of the sphere. Figure 5.7 illustrates the placement of the IMUs with continuously increasing distance to the center of the sphere.

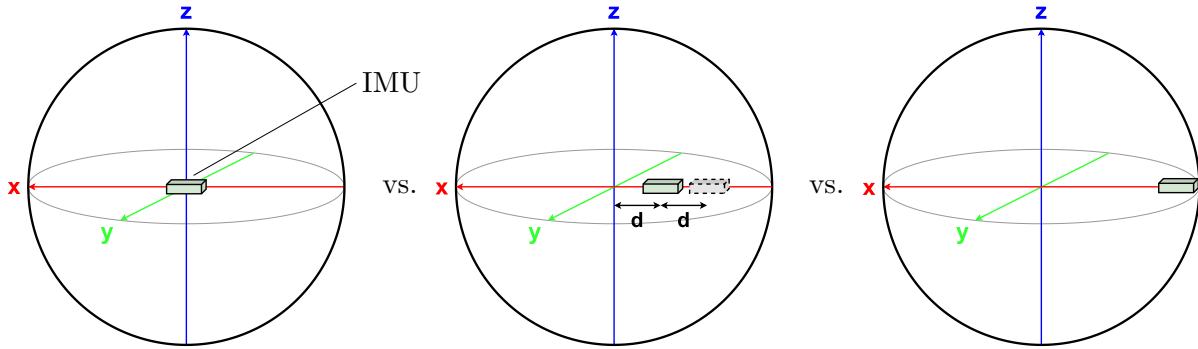


Figure 5.7: Experiment B: Distance from center. Schematic of a spherical robot (black circle) including its BCS with (from left to right) increasing distance of one IMU from the center.

- **Experiment C** evaluates how the symmetry in the placement of IMUs affects the orientation determination accuracy. For this experiment we have two configurations. For the first configuration, we place both IMUs on the same side of the sphere's center at a predefined distance. For the second configuration, we place the IMUs with the same distance but this time on opposite sides of the center of the sphere. Figure 5.8 shows both configurations schematically. For the distance, we take the results of Experiment B regarding the distance from the center of the sphere already into account. If the orientation accuracy is independent of the distance from the center, we chose the maximum distance from the center of the sphere. Otherwise, if the IMUs give a more accurate orientation in the center, in which case no testing of symmetry is possible, we chose the next best distance from the center of the sphere.

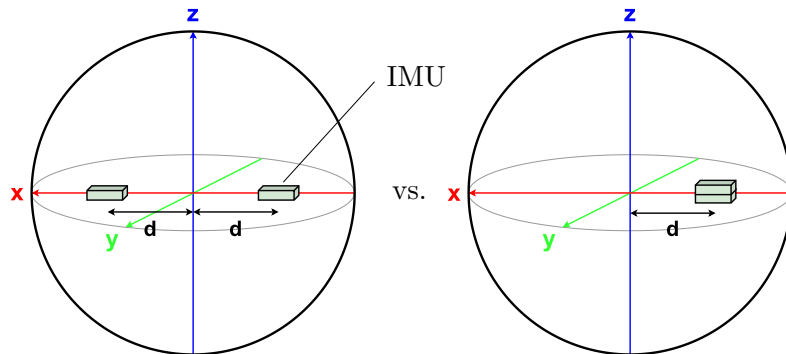


Figure 5.8: Experiment C: Symmetry in placement. Schematic of a spherical robot (black circle) including its BCS. Configuration with two IMUs on opposite sides in distance d from the center (left) and two IMUs on the same side of the center in distance d (right).

• In the last experiment, **Experiment D**, we determine the influence of axial placement of the IMUs on the orientation determination accuracy. We compare the orientation determination under the following scenarios: First, we place multiple IMUs in the center of the sphere. We then compare this configuration to the configuration of one IMU on each axis. We take the result of Experiment A into account for the choosing the number of IMUs, which we place in the sphere's center. To avoid a possible advantage for this configuration by using more IMUs, the maximum number of IMUs is three for this comparison. If Experiment C shows that the symmetrical placement of the sensors on the axes is advantageous, we also test configuration with two IMUs per axis on opposite sides of the sphere's center. In this case, we set the maximum number of IMUs in the center of the sphere to six. We compare these configurations with the combination of them, i.e. one IMU in the center and one per axis.

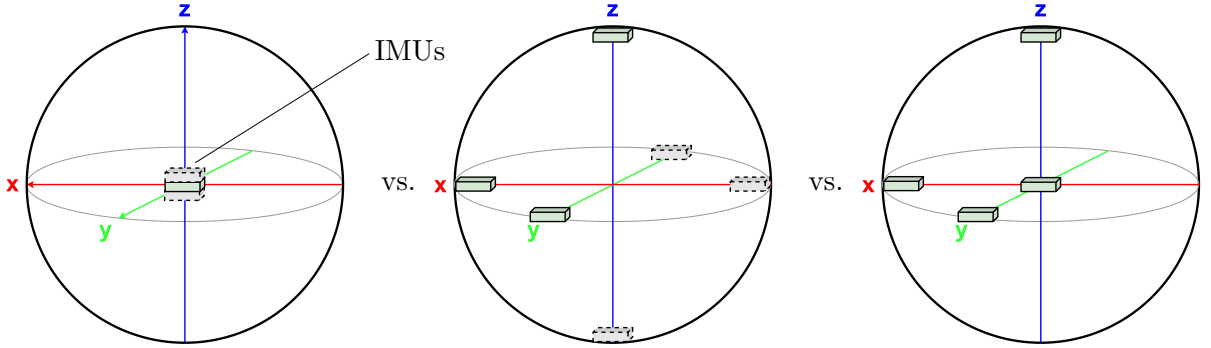


Figure 5.9: Experiment D: Axis assignment. Schematic of a spherical robot (black circle) including its BCS. Configuration with up to three IMUs located in the center (left). Configuration with one IMU on each rotational axis, extendable by one more IMU on each axis on the opposite side of the center (middle). Combination of the two previous configurations (right).

To compare the individual configurations, we calculate the RMSE for each experiment. Let $\alpha_{opti,t}$ be the Euler angle around axis k determined by the Optitrack system at time t , $\alpha_{imu,t}$ be the Euler angle around axis k determined by the IMUs at time t , Δt be the time step between the samples and n be the number of gathered samples, then we calculate the RMSE around axis k with equation 25. Using the $RMSE_k$ of each axis k , we calculate the total, or merged, RMSE of an experiment with equation 26.

$$RMSE_k = \sqrt{\frac{\sum_{t=0}^{n \cdot \Delta t} (\alpha_{opti,t} - \alpha_{imu,t})^2}{n}} \quad (25)$$

$$RMSE = \sqrt{\frac{\sum_{k=1}^3 (RMSE_k)^2}{3}} \quad (26)$$

For more statistical robustness against outlier values due to bad recordings, we run several experiments for each configuration. To combine the RMSEs from all experiments for one configuration to one final value, we reuse equation 26. But we replace the $RMSE_k$ of each axis k

with the RMSE of each experiment for the configuration and set the limit of the sum, as well as the denominator, to the number of experiments performed for each configuration. To decide when to choose one configuration over another, we calculate the relative error, called improvement in this thesis, between the configurations. Let RMSE_{ref} be the merged RMSE of a chosen configuration, which serves as a reference, and RMSE_j be the merged RMSE of configuration j , then we calculate the improvement IMP_j with

$$\text{IMP}_j = \frac{\text{RMSE}_j - \text{RMSE}_{ref}}{\text{RMSE}_{ref}} \cdot 100 [\%]. \quad (27)$$

Due to this calculation of the improvement a positive improvement means that the configuration j is less accurate than the chosen reference configuration. And vice versa, if the improvement is negative the configuration j is more accurate than the reference configuration. We define a significant improvement to be greater than 5%. In order to obtain comparable results for each experiment, each individual experiment is performed in one session. This ensures similar performance of the Optitrack due to similar light conditions, and also similar power supply of the IMUs. E.g. a freshly charged powerbank might alter the performance of an IMU. However, we are not able to compare the results (RMSE) of the different experiments, because we record them under different conditions.

5.2.1 Experiment A: Number of IMUs

The first experiment, Experiment A, as described in Chapter 5.2, evaluates the relationship between the number of IMUs and the accuracy of orientation determination. We test and compare the following configurations:

- A1) One IMU in the center of the sphere,
- A2) Two IMUs in the center of the sphere,
- A3) Three IMUs in the center of the sphere,
- A4) Four IMUs in the center of the sphere,
- A5) Five IMUs in the center of the sphere,
- A6) Six IMUs in the center of the sphere.

Before the first experiment, we connect the Optitrack system to the laptop and teach the Motive:Tracker software the rigid body of the sphere. Since we glued the plates together for stabilization, it is possible to use the same rigid body for each experiment and leave the Optitrack balls on the construction for all experiments. Furthermore, we only need to remove and reattach the Raspberry Pi, when we attach an IMU to the positive y -axis of the sphere. The following rest of the procedure applies for all upcoming experiments. First, we attach the IMUs to the specified positions. Since we perform three experiments for each configuration, the IMUs remain screwed on until we start testing a new configuration. We start the Motive:Tracker software to check whether the Optitrack registers our robot as a rigid body. Each experiment, we set a new

name for the rigid body and set the “Stream Rigid Bodies“ option to “True“. After connecting the Raspberry with a 5 V powerbank, we connect to the Raspberry Pi via SSH. First, we start the VRPN Client ROS then the orientation determination program. For the first experiment of each configuration, we use the save configuration option to save the dynamically determined axis allocation for each IMU of the new configurations. For the two following experiments, we just load the configuration, in order to avoid a reallocation and thus to save time. After the axis allocation, we begin to record a rosbag file with all published topics and start rotating the sphere.

In the first experiment, we close the shell and rotate the sphere almost 360° around the z -axis. During the experiment, we record the orientation from the IMU and the Optitrack system. Figure 5.10 shows both orientations as Euler angles and the absolute error between them.

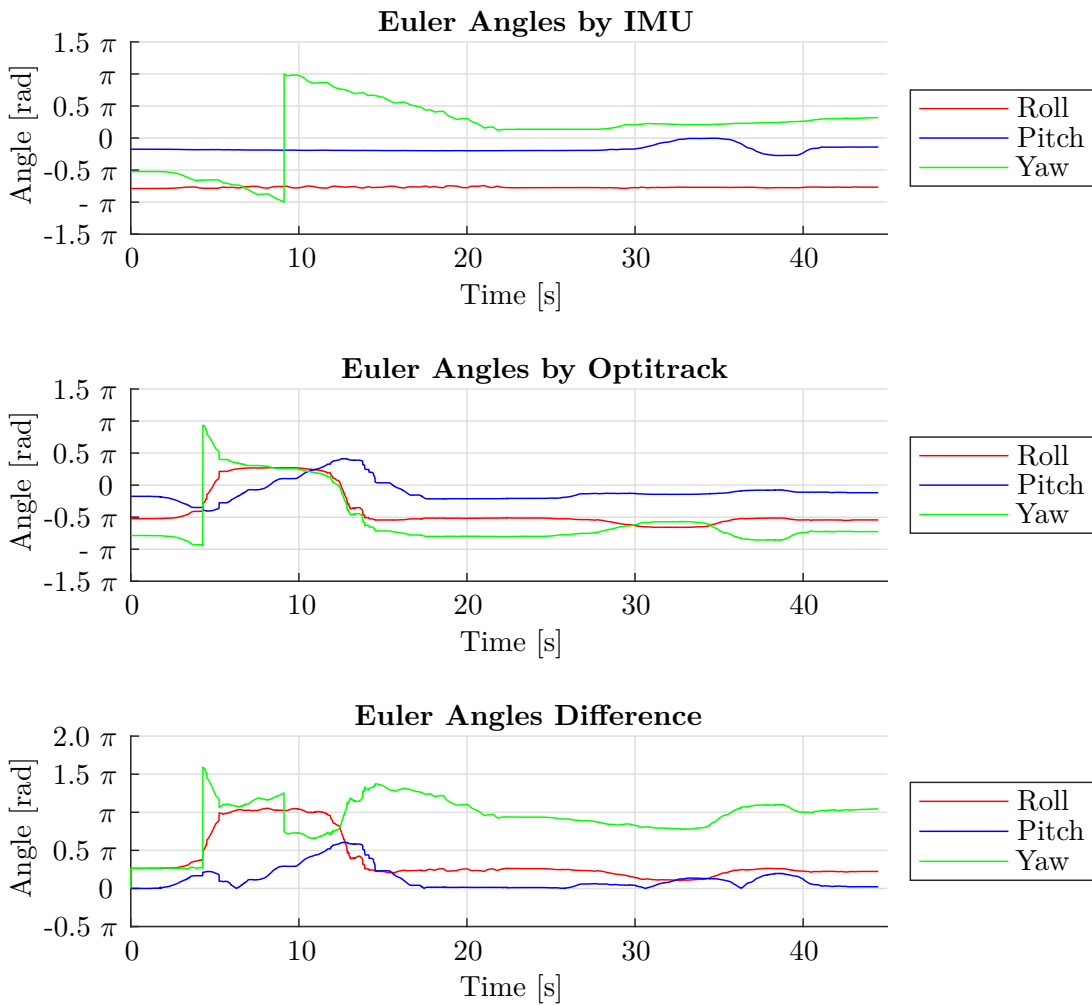
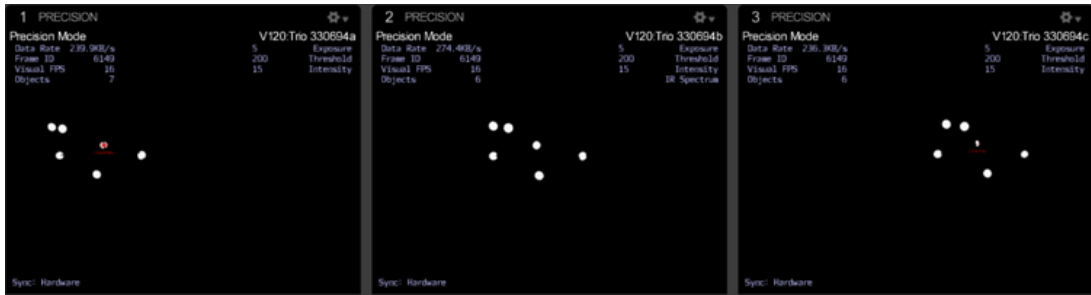


Figure 5.10: Euler Angles obtained during the first experiment of Experiment A Configuration 1. Yaw rotation with one IMU in the center. Top: Euler Angles determined with the IMU data and the filter. Middle: Orientation recorded from the Optitrack system. Bottom: Absolute Euler Angles difference (Ground truth minus IMU). The Euler Angles are Roll (red), Pitch (blue) and Yaw (green).



(a) Display of the recognition of the balls with the sphere closed. In addition to the six attached balls, there are three little dots.



(b) Display of the recognition of the balls with the sphere open. Only the six attached balls recognizable.

Figure 5.11: Display of the balls recognized by the three cameras of the Optitrack system (detail of the Motive:Tracker software).

We recognize that the orientation from the IMU data is consistent with the rotation performed. However, this is not the case for the data of the Optitrack system, our ground truth. The Yaw rotation is identifiable, but seems not consistently accurate. We performed the rotation with an rotation velocity as constant as possible by hand, which we recognize in the data of the IMU but not in the data from the Optitrack system. We also observe movement around Roll and Pitch, that were not actually performed. These obtained data are useless for our evaluation. We see on Motive that the shell casts a reflection. Figure 5.11 shows that reflection of the shell on Motive. It seems that the shell of the sphere distorts the orientation determination of the Optitrack system. We perform the same experiment, but this time we leave the shell open and just place the mounting inside the bottom half of the sphere to test whether the ground truth orientation by the Optitrack system becomes more accurate. Figure 5.12 shows the result.

In Figure 5.12 and Figure 5.10, we observe that the Yaw angle error slowly increases over time, because the Yaw angle of the IMU for Figure 5.12 from time $t \approx 26$ and for Figure 5.10 from time $t \approx 22$ is steadily growing even during standstill. This drift in Yaw is due to the fact that we do not use a magnetometer for orientation determination. We can determine Roll and Pitch angles using the accelerometer [68, 69]. But the accelerometer cannot provide Yaw information if the sensor frame is aligned with the earth frame. Because here, the acceleration in the z -axis does not change when the robot turns right or left [70]. So for this case, we only use gyroscopes that merge into one virtual gyroscope using the function for combining the raw

data. The gyroscope can reach the actual value of the Yaw for a short time, but the results on a longer period lead to a drift, as explained in 3.3 under challenges, which the filter addresses. Briefly explained, the drift results from the accumulation of the bias offset error and the noise of gyroscope measurements by integration over time. This integration leads to unacceptable orientation results. Many scientists [71–82] have been researching the drift phenomenon and drift correction of gyroscopes. Due to this drift, we will not consider the Yaw angle from here on. Therefore, we change the upper limit of the sum and the denominator in equation 26 from 3 to 2.

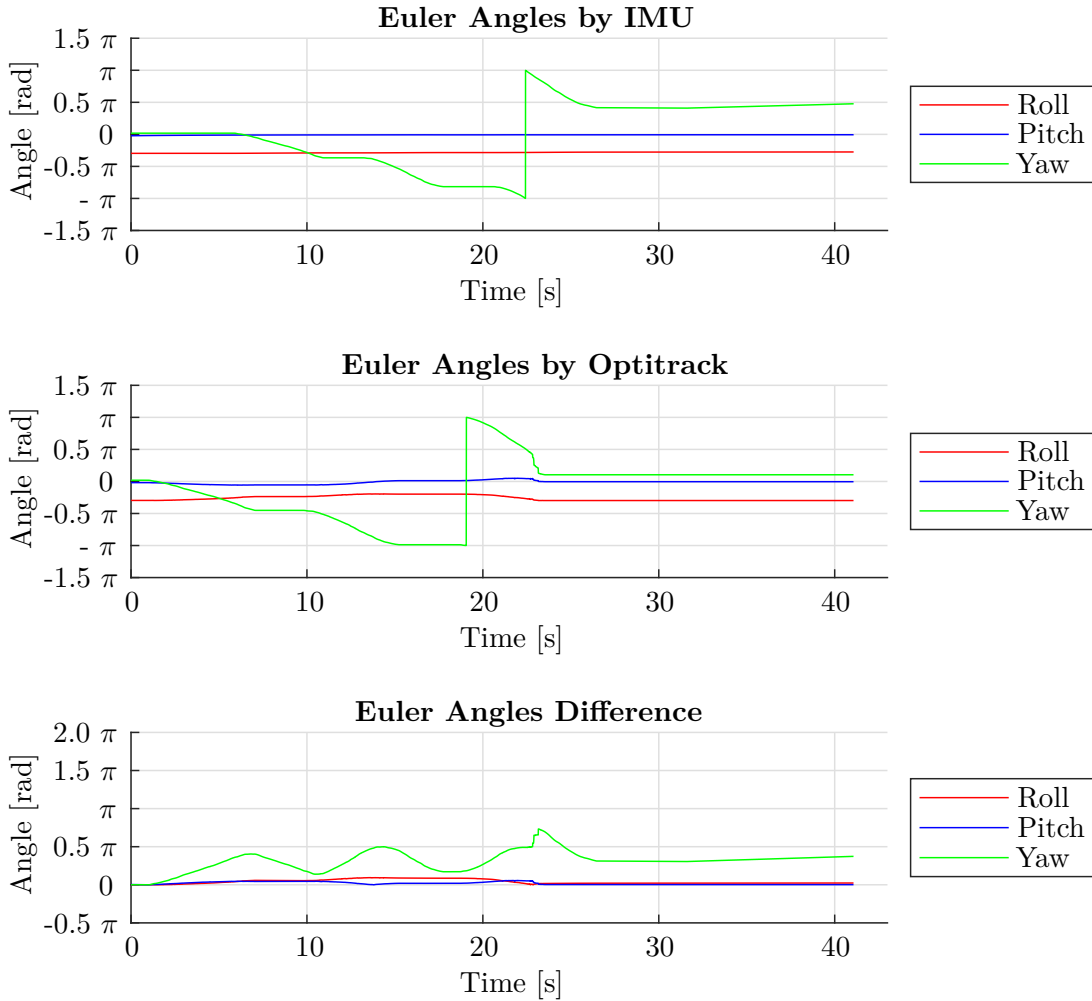


Figure 5.12: Euler Angles obtained during the second experiment of Experiment A Configuration 1. Almost a whole Yaw rotation with one IMU in the center. Top: Euler Angles determined with the IMU data and the filter. Middle: Orientation recorded from the Optitrack system. Bottom: Absolute Euler Angles difference (Ground truth minus IMU). The Euler Angles are Roll (red), Pitch (blue) and Yaw (green) all plotted against time.

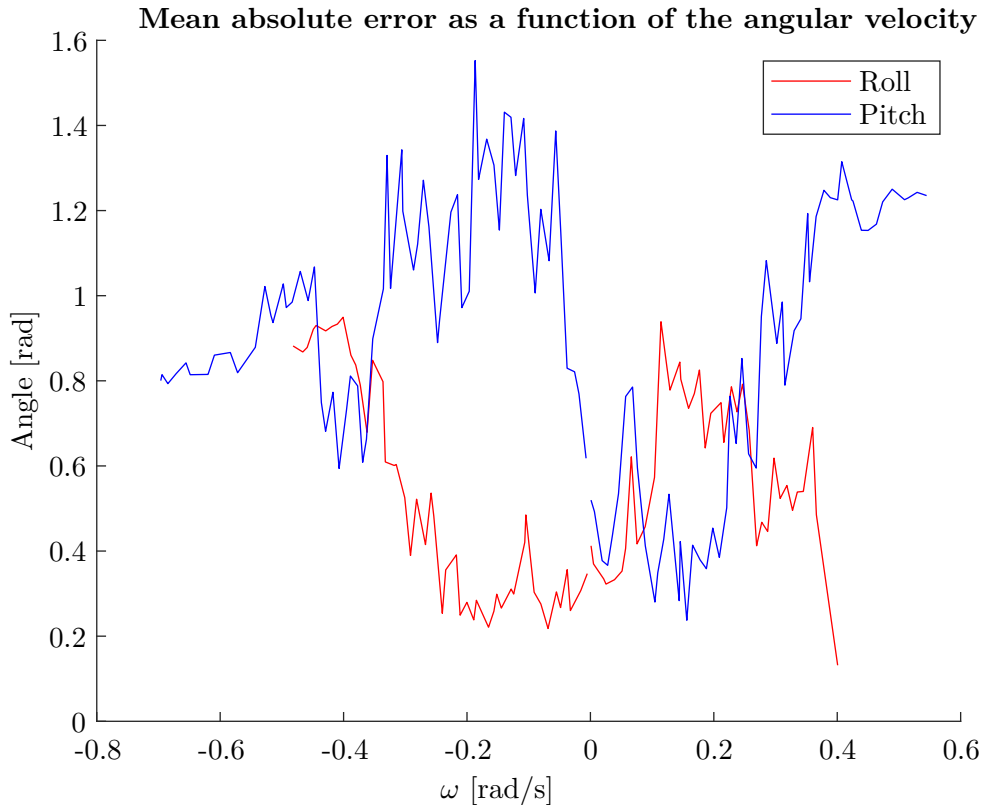


Figure 5.13: Mean absolute error of Roll (red) and Pitch (blue) as a function of the angular velocity around their respective rotational axis. Plot from the second experiment of the first configuration, with one IMU in the center, from the Experiment A.

The absolute error as a function of the rotational speed can be seen in Figure 5.13. Here we already only consider Roll and Pitch. We cannot recognize any significant correlation from this, and will therefore not refer to it further for the evaluation.

We conduct three experiments for each configuration. The first experiment is a Roll movement (rotation back and forth) and the second one a Pitch movement. For the third experiment, we first perform a slight rotation around the x -axis and then rotate a little back and forth around the new y -axis in the tilted state and then return to the initial position. We repeat this in the opposite direction of roll rotation. Figures A.1–A.18 show the results of the individual experiments of Experiment A as Euler Angles (orientation determined by the IMUs and orientation determined by the Optitrack system) and the absolute error between them.

Results

Table 5.1 tabulates the RMSE for each of the performed experiments and the merged RMSE for each configuration, calculated with equations 25 and 26. Figure 5.14 shows the RMSE values graphically as a bar chart. Based on the merged RMSE values for each configuration, we calculate the relative improvement for each configuration compared to the merged RMSE from

configuration A1, refer to equation 27. Table 5.2 lists these relative improvements.

From the gathered data, we can observe an improvement in the orientation determination accuracy when we place more IMUs. More precisely, we have an improvement of 21.49% if we place two instead of one IMU in the center of the sphere. For three IMUs in the sphere's center the accuracy of orientation determination improves by 34.72%, for four IMUs by 48.71%, for five IMUs by 51.68% and for six IMUs by 50.66%. Based on the performed experiments, we determine that two IMUs are significantly more accurate regarding the orientation determination than one IMU in the sphere's center. The same applies for three, up to six, IMUs located in the center of the sphere in comparison with one IMU in the center of the sphere.

Experiment	RMSE Roll	RMSE Pitch	RMSE Merged
A1 Roll	0.4045	0.5775	0.4986
A1 Pitch	0.7453	0.4187	0.6045
A1 Both	0.4243	0.9964	0.7658
A1	0.7075	0.5475	0.6326
A2 Roll	0.4369	0.3472	0.3946
A2 Pitch	0.6398	0.2580	0.4878
A2 Both	0.5992	0.5773	0.5884
A2	0.4165	0.5655	0.4966
A3 Roll	0.3491	0.2429	0.3007
A3 Pitch	0.2045	0.2901	0.2510
A3 Both	0.4636	0.7080	0.5984
A3	0.4635	0.3553	0.4129
A4 Roll	0.2239	0.3583	0.2988
A4 Pitch	0.3474	0.1025	0.2561
A4 Both	0.2579	0.5053	0.4011
A4	0.3625	0.2813	0.3244
A5 Roll	0.0709	0.3001	0.2180
A5 Pitch	0.2658	0.1278	0.2085
A5 Both	0.2576	0.5586	0.4350
A5	0.3735	0.2176	0.3056
A6 Roll	0.1582	0.3939	0.3002
A6 Pitch	0.2861	0.1511	0.2288
A6 Both	0.1621	0.5227	0.3870
A6	0.3878	0.2107	0.3121

Table 5.1: Results of Experiment A. Specification of the RMSE in rad. RMSE in x (Roll) and y (Pitch) direction and merged RMSE for each of the performed experiments. Merged RMSE for each configuration (gray rows).

Experiment	A1	A2	A3	A4	A5	A6
Improvement [%]	–	-21.4934	-34.7212	-48.7105	-51.6831	-50.6637

Table 5.2: Results of Experiment A. Relative Improvement compared to the first experiment (here A1).

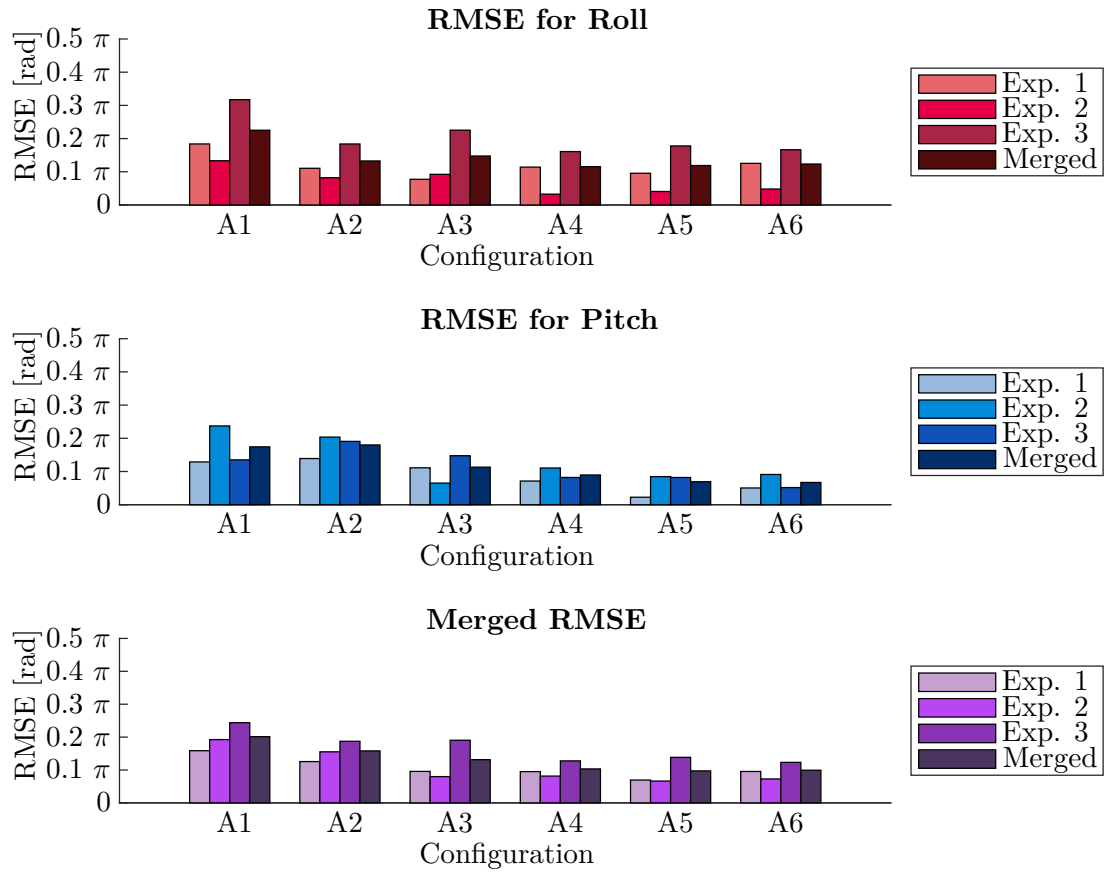


Figure 5.14: RMSE for each of the performed experiments and the merged RMSE for each configuration of Experiment A. RMSE divided into Roll (red), Pitch (blue) and Merged (Purple), whereas the darkness of the color represents the single experiments and the darkest tone of each color the merged RMSE. The darkest purple represents the final result for each configuration.

5.2.2 Experiment B: Distance from Center

The second experiment, Experiment B, as described in Chapter 5.2, evaluates the dependency of the orientation determination accuracy on the distance of the IMU from the sphere's center. For this experiment, we first determine the distance d by which we can move the IMU uniformly from the center to the edge of the sphere. For this experiment, we will use only the x -axis of the base plate, since this allows the same orientation of the IMU during attachment and also has the smallest distance between the rails. In the following, we always indicate all distances from the center of the (semi) circles of the rails. The holes for attaching the IMU are 2.794 cm apart. The rail on the base plate for mounting the IMU in the center of the sphere has a length of 2.840 cm and is 1.353 cm far away from the long rail. The long rail on the x -axis is 10.172 cm long. Therefore, we can attach the IMU on the long rail with a minimum distance from the IMU's center to the sphere's center of 4.170 cm and a maximum distance of 11.548 cm. The difference between the maximum and the minimum distance is 7.378 cm. That difference divided by the minimum distance is 1.77. To move the IMU by evenly distances, we set the distances d_i from the IMU's center to the sphere's center to $d_1 = 0$ cm, $d_2 = 4.170$ cm, $d_3 = 7.859$ cm and $d_4 = 11.548$ cm. Thus, we test and compare the following configurations:

- B1) One IMU in the center of the sphere (at the distance of 0 cm from the center of the sphere),
- B2) One IMU at the distance of 4.170 cm from the center of the sphere,
- B3) One IMU at the distance of 7.859 cm from the center of the sphere,
- B4) One IMU at the edge of the sphere (at the distance of 11.548 cm from the center of the sphere).

Analogous to Experiment A, we conduct three experiments for each configuration. The first experiment is a Roll movement (rotation back and forth) and the second one a Pitch movement. For the third experiment, we first perform a slight rotation around the x -axis and then rotate a little back and forth around the new y -axis in the tilted state and then return to the initial position. We repeat this in the opposite direction of roll rotation. Figures A.19–A.30 show the results of the individual experiments of Experiment B as Euler Angles (orientation determined by the IMUs and orientation determined by the Optitrack system) and the absolute error between them.

Results

Table 5.3 tabulates the RMSE for each of the performed experiments and the merged RMSE for each configuration, calculated with equations 25 and 26. Figure 5.15 shows the RMSE values graphically as a bar chart. Based on the merged RMSE values for each configuration, we calculate the relative improvement for each configuration compared to the merged RMSE from configuration B1, refer to equation 27. Table 5.4 lists these relative improvements.

From the improvements, we recognize that an IMU placed in the center of the sphere is significantly better than one placed further out regarding the orientation determination accuracy. Compared to an IMU placed in the center of the sphere, one shifted by $d = 4.170$ cm from the center of the sphere, as well as one at the edge of the sphere, with $d = 11.548$ cm from the sphere's

center, are approximately 10.6% less accurate in orientation determination. The configuration with a distance $d = 7.859$ cm from the sphere's center shows a deterioration of 11.2%.

Experiment	RMSE Roll	RMSE Pitch	RMSE Merged
B1 Roll	0.0815	0.3564	0.2585
B1 Pitch	0.4666	0.2083	0.3613
B1 Both	0.4877	0.5133	0.5007
B1	0.3803	0.3925	0.3865
B2 Roll	0.2145	0.5423	0.4124
B2 Pitch	0.4989	0.1524	0.3689
B2 Both	0.2687	0.6423	0.4923
B2	0.4932	0.3498	0.4276
B3 Roll	0.2088	0.4206	0.3320
B3 Pitch	0.6011	0.3724	0.5000
B3 Both	0.4639	0.4153	0.4403
B3	0.4033	0.4547	0.4298
B4 Roll	0.2970	0.5450	0.4389
B4 Pitch	0.5317	0.1940	0.4002
B4 Both	0.4552	0.4287	0.4421
B4	0.4157	0.4390	0.4275

Table 5.3: Results of Experiment B. Specification of the RMSE in rad. RMSE in x (Roll) and y (Pitch) direction and merged RMSE for each of the performed experiments. Merged RMSE for each configuration (gray rows).

Experiment	B1	B2	B3	B4
Improvement [%]	–	10.6423	11.2060	10.6216

Table 5.4: Results of Experiment B. Relative Improvement compared to the first experiment (here B1).

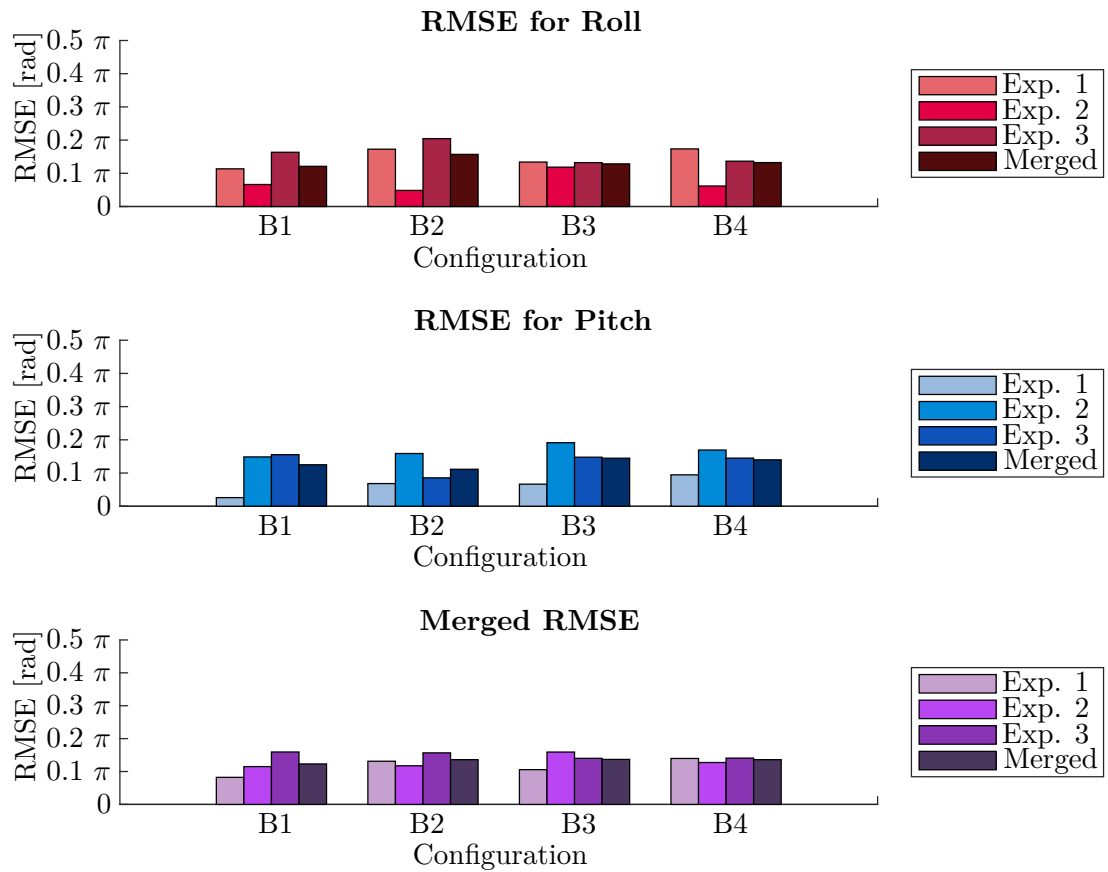


Figure 5.15: RMSE for each of the performed experiments and the merged RMSE for each configuration of Experiment B. RMSE divided into Roll (red), Pitch (blue) and Merged (Purple), whereas the darkness of the color represents the single experiments and the darkest tone of each color the merged RMSE. The darkest purple represents the final result for each configuration.

5.2.3 Experiment C: Symmetry in Placement

In Experiment C, as described in Chapter 5.2, we determine the relation between the accuracy of orientation determination and symmetry in the placement of the IMUs. We examine and compare the following configurations:

- C1) Two IMUs on the same side of the sphere's center,
- C2) Two IMUs on opposite sides of the sphere's center.

For the distance between IMUs and the center of the sphere, we refer to the result of Experiment B. In this experiment, we find that an IMU at the sphere's center gives better results for orientation than an IMU placed further out. Therefore, we chose the next best distance from the center of the sphere. However, the distance to the sphere's center does not seem to have any effect on the accuracy of the orientation determination. For this reason, we choose the minimum distance between the center of the sphere and our IMUs, here $d = 4.170$ cm.

We conduct the same three experiments for each configuration as in Experiment A and Experiment B. The first experiment is a Roll movement (rotation back and forth) and the second one a Pitch movement. For the third experiment, we first perform a slight rotation around the x -axis and then rotate a little back and forth around the new y -axis in the tilted state and then return to the initial position. We repeat this in the opposite direction of roll rotation. Figures A.31–A.36 show the results of the individual experiments of Experiment C as Euler Angles (orientation determined by the IMUs and orientation determined by the Optitrack system) and the absolute error between them.

Results

Table 5.6 tabulates the RMSE for each of the performed experiments and the merged RMSE for each configuration, calculated with equations 25 and 26. Figure 5.16 shows the RMSE values graphically as a bar chart. Based on the merged RMSE values for each configuration, we calculate the relative improvement for each configuration compared to the merged RMSE from configuration C1, refer to equation 27. Table 5.5 lists these relative improvements.

The orientation determination of configuration C2, two IMUs on opposite sides of the sphere's center, is 1.40 % less accurate than the orientation determination of configuration C1, two IMUs on the same side of the sphere's center. From this result, we conclude that a symmetrical placement of IMUs around the center of the sphere does not significantly improve, nor worsen, the accuracy of orientation determination.

Experiment	C1	C2
Improvement [%]	–	1.3965

Table 5.5: Results of Experiment C. Relative Improvement compared to the first experiment (here C1).

Experiment	RMSE Roll	RMSE Pitch	RMSE Merged
C1 Roll	0.3540	0.3584	0.3562
C1 Pitch	0.3605	0.2192	0.2983
C1 Both	0.3753	0.4080	0.3920
C1	0.3381	0.3634	0.3510
C2 Roll	0.3588	0.3930	0.3763
C2 Pitch	0.2908	0.1615	0.2352
C2 Both	0.2081	0.5681	0.4278
C2	0.4096	0.2925	0.3559

Table 5.6: Results of Experiment C. Specification of the RMSE in rad. RMSE in x (Roll) and y (Pitch) direction and merged RMSE for each of the performed experiments. Merged RMSE for each configuration (gray rows).

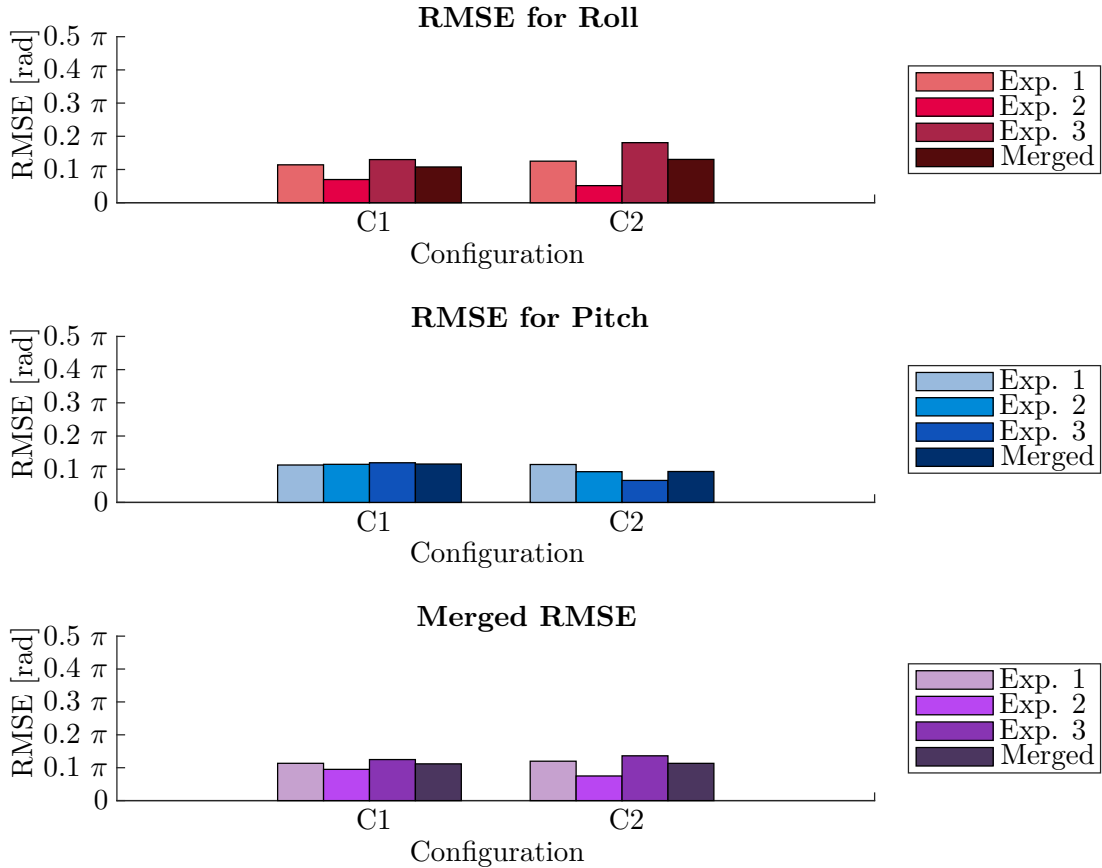


Figure 5.16: RMSE for each of the performed experiments and the merged RMSE for each configuration of Experiment C. RMSE divided into Roll (red), Pitch (blue) and Merged (Purple), whereas the darkness of the color represents the single experiments and the darkest tone of each color the merged RMSE. The darkest purple represents the final result for each configuration.

5.2.4 Experiment D: Axial Placement

In Experiment D, we evaluate the influence of axial placement of the IMUs on the orientation determination accuracy. Since we show in Experiment A that more IMUs lead to more accurate orientations, we set the number of IMUs in the sphere's center for the first configuration (D1) to three. In Experiment C, we show that a symmetrical placement of IMUs is not beneficial for a more accurate orientation determination. Therefore, we do not perform experiments for the following configurations: two IMUs on each axis, and six IMUs in the sphere's center. In this experiment we test and compare the following configurations:

- D1) Three IMUs in the center of the sphere,
- D2) Three IMUs each on one rotational axis,
- D3) One IMU in the sphere's center and three IMUs each on one rotational axis.

We set the distances (IMUs to the sphere's center) of configuration D2 to the maximum distance 11.548 cm, because the distance to the sphere's center seems to have no effect on the accuracy of the orientation determination.

Likewise to the previous experiments, we conduct three experiments for each configuration. The first experiment is a Roll movement (rotation back and forth) and the second one a Pitch movement. For the third experiment, we first perform a slight rotation around the x -axis and then rotate a little back and forth around the new y -axis in the tilted state and then return to the initial position. We repeat this in the opposite direction of roll rotation. Figures A.37–A.45 show the results of the individual experiments of Experiment A as Euler Angles (orientation determined by the IMUs and orientation determined by the Optitrack system) and the absolute error between them.

Results

Table 5.7 tabulates the RMSE for each of the performed experiments and the merged RMSE for each configuration, calculated with equations 25 and 26. Figure 5.17 shows the RMSE values graphically as a bar chart. Based on the merged RMSE values for each configuration, we calculate the relative improvement for each configuration compared to the merged RMSE from configuration D1, refer to equation 27. Table 5.8 lists these relative improvements.

From the improvements, we recognize that the most accurate configuration regarding orientation determination is D1 (three IMUs in the center of the sphere), followed by the configuration D3 (One IMU in the sphere's center and three IMUs each on one rotational axis). The configuration D2 with one IMU on each rotational axis has the largest RMSE and gives therefore the least accurate orientation. Both configurations (D2 and D3) are significantly worse than D1 regarding the accuracy of the orientation determination.

Experiment	RMSE Roll	RMSE Pitch	RMSE Merged
D1 Roll	0.1447	0.2358	0.1956
D1 Pitch	0.2603	0.1614	0.2166
D1 Both	0.4501	0.5523	0.5038
D1	0.3590	0.3116	0.3361
D2 Roll	0.2338	0.3159	0.2779
D2 Pitch	0.5353	0.4030	0.4738
D2 Both	0.4619	0.4276	0.4451
D2	0.3852	0.4299	0.4082
D3 Roll	0.1145	0.3045	0.2300
D3 Pitch	0.4039	0.1634	0.3081
D3 Both	0.5537	0.4852	0.5206
D3	0.3439	0.4012	0.3736

Table 5.7: Results of Experiment D. Specification of the RMSE in rad. RMSE in x (Roll) and y (Pitch) direction and merged RMSE for each of the performed experiments. Merged RMSE for each configuration (gray rows).

Experiment	D1	D2	D3
Improvement [%]	–	21.4251	11.1554

Table 5.8: Results of Experiment D. Relative Improvement compared to the first experiment (here D1).

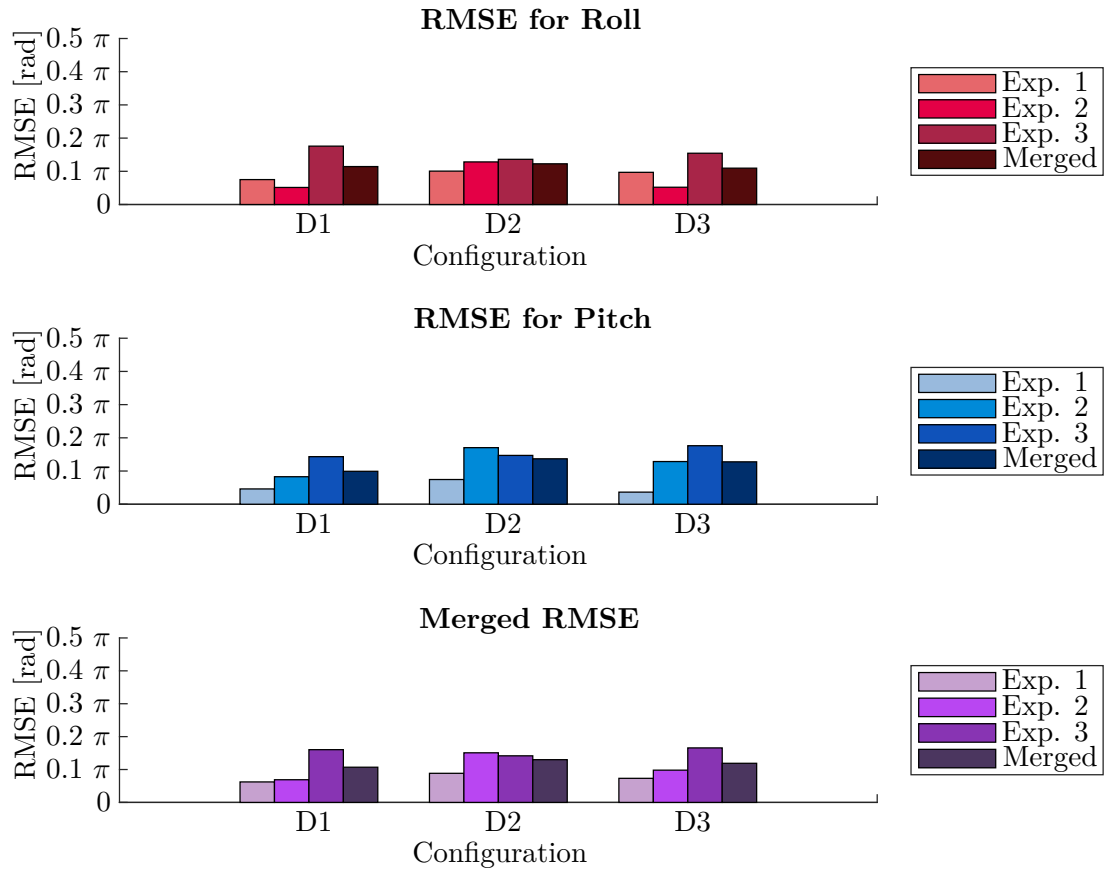


Figure 5.17: RMSE for each of the performed experiments and the merged RMSE for each configuration of Experiment D. RMSE divided into Roll (red), Pitch (blue) and Merged (Purple), whereas the darkness of the color represents the single experiments and the darkest tone of each color the merged RMSE. The darkest purple represents the final result for each configuration.

5.3 Comparison and Discussion

In this Chapter, we compare the results of the experiments and discuss the significance. Subsequently, we transfer our findings and establish optimal IMU configurations, or approaches for IMU placement, for the individual robot types.

In **Experiment A** we determine the relationship between the number of IMUs and the orientation determination accuracy. Table 5.1 and Table 5.2 fully list the results of the performed experiments. Table 5.9 lists the end results for each tested configuration. As we already state in Chapter 5.2.1, adding more IMUs in the sphere's center significantly improves the orientation determination accuracy. By taking the mean of the measurements to combine the measurements of all IMUs we average the independent stochastic error out, refer to [12]. Furthermore, we detect that the difference between the improvements compared to one IMU in the center decreases with increasing number of IMUs. In Chapter 4.1 we assume, that the RMSE shows an exponential downward trend, refer to equation 21. Figure 5.18 visualizes the RMSEs plotted against the number of IMUs. As expected, we observe that exponential downward trend in Figure 5.18. We observe this exponential downward of the RMSE values also in the relative improvement values for an increasing numbers of sensors.

Experiment	A1	A2	A3	A4	A5	A6
RMSE [rad]	0.6326	0.4966	0.4129	0.3244	0.3056	0.3121

Table 5.9: End results of Experiment A. Merged RMSE for each configuration.

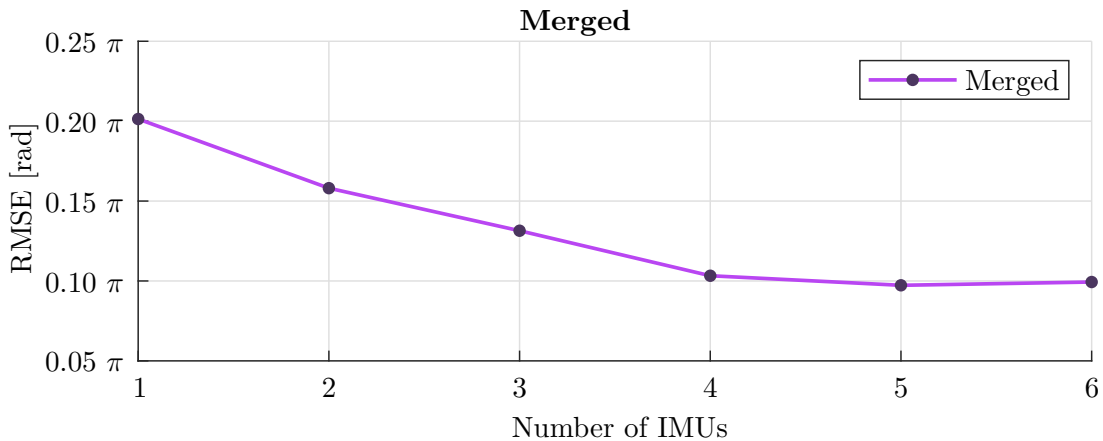


Figure 5.18: End results of Experiment A. Merged RMSE [rad] for each configuration plotted against the number of IMUs.

To compare the configurations more closely, we calculate for each configuration the improvement in reference to the previous configuration with one IMU less in the center of the sphere. Table 5.10 shows the relative improvements for each configuration compared to the previous one. For six IMUs in the center of the sphere, we have only an improvement of 2.1099% in comparison with five IMUs in the center of the sphere. Ergo, for a number of five IMUs and

above, the improvement in the accuracy of the orientation determination is no longer significant. Thus, the application of more than five IMUs is not profitable for the accuracy of orientation determination.

Experiment	A1	A2	A3	A4	A5	A6
Improvement [%]	–	-21.4934	-16.8493	-21.4302	-5.7956	2.1099

Table 5.10: Results of Experiment A. Relative Improvement compared to previous configuration (improvement for A2 in reference to A1, and improvement for A3 in reference to A2, etc.).

In **Experiment B** we determine the dependency of the orientation determination accuracy on the distance of the IMU from the sphere’s center. Table 5.3 and Table 5.4 fully list the results of the performed experiments. Table 5.11 lists the end results for each tested configuration. From the gathered data, we conclude that one IMU placed in the sphere’s center is significantly better than one placed further out regarding the orientation determination accuracy. This confirms our previous presumption in Chapter 4.1, that placing the IMU outside the center of the sphere leads to a rotational movement, and thus an additional acceleration, of the IMU, which disturbs the accelerometer data. If we compare the RMSE from the configuration B2 with an RMSE of 0.4276 with the RMSE of configuration B4 0.4275, we recognize that the results for both of them are nearly identical. Both configurations show a deterioration of approximately 10.6 % compared to one IMU in the center of the sphere. The result of configuration B3 with an RMSE of 0.4298 results into deterioration of 11.2 %, which is still very close to the result of configurations B2 and B4. The improvement of configuration B3 in reference to B2 or B4 (here we choose B2) is 0.5095 %. Thus, the difference between the orientation determination accuracy for configuration B3 and B2 or B4 is insignificant. Figure 5.19 visualizes the RMSEs plotted against the distance d of the IMU from the center of the sphere. When we place an IMU off centered, the distance to the sphere’s center seems to have no effect on the accuracy of the orientation determination.

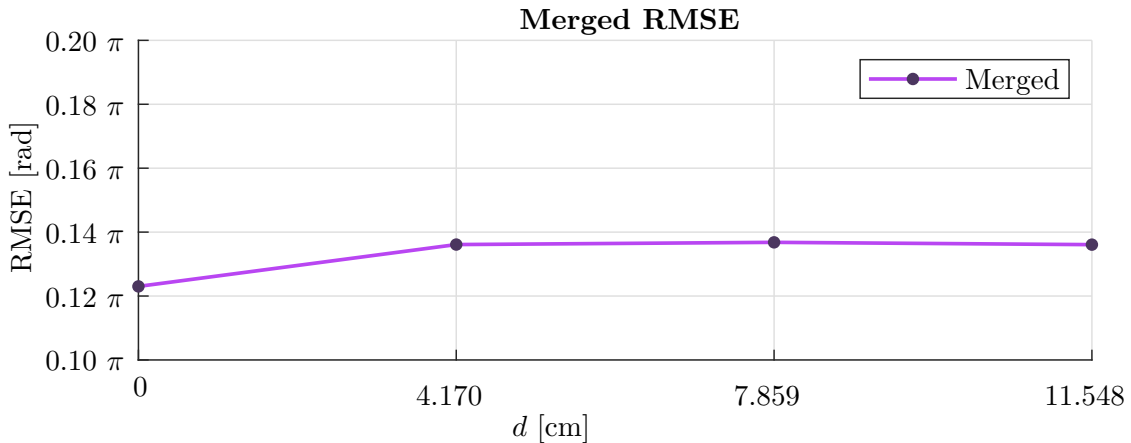


Figure 5.19: End results of Experiment B. Merged RMSE [rad] for each configuration plotted against the distance d from the center of the sphere.

Experiment	B1	B2	B3	B4
RMSE [rad]	0.3865	0.4276	0.4298	0.4275

Table 5.11: End results of Experiment B. Merged RMSE for each configuration.

In **Experiment C** we determine the relation between the accuracy of orientation determination and symmetry in the placement of the IMUs. Table 5.6 and Table 5.5 fully list the results of the performed experiments. Table 5.12 lists the end results for each tested configuration. The RMSEs from both configurations are very similar with an RMSE of 0.3510 for configuration C1 and RMSE of 0.3559 for configuration C2. The improvement of configuration C2 in reference to configuration C1 is with 1.3965% insignificant. From the results, we see that symmetrically placing two IMUs around the sphere's center on one axis provides an as accurate orientation as placing two IMUs on the same side of the sphere's center on the axis.

Experiment	C1	C2
RMSE [rad]	0.3510	0.3559

Table 5.12: End results of Experiment C. Merged RMSE for each configuration.

In **Experiment D** we determine the influence of axial placement of the IMUs on the orientation determination accuracy. Table 5.7 and Table 5.8 fully list the results of the performed experiments. Table 5.13 lists the end results for each tested configuration. As we already state in Chapter 5.2.4, the most accurate configuration regarding orientation determination is D1 (three IMUs in the center of the sphere) with an RMSE of 0.3361, followed by the configuration D3 (One IMU in the sphere's center and three IMUs each on one rotational axis) with an RMSE of 0.3736. The configuration D2 with one IMU on each rotational axis has the largest RMSE of 0.4082 and gives therefore the least accurate orientation. If we compare D2 and D3 directly, we get an improvement of -8.46% with D2 being the reference configuration (equation 27). Ergo, adding an additional IMU in the sphere's center improves the orientation determination accuracy significantly. Based on the results of the previous Experiments A and B, we can confirm this result. From Experiment A, we know that four IMUs provide significantly more accurate orientations, and in Experiment B we show that IMUs placed in the center are better for orientation determination accuracy than off centered IMUs. From this we conclude that because of the fourth IMU (and thus one more IMU) configuration D3 provides significantly more accurate orientation than configuration D2. However, configuration D3 is not more accurate than configuration D1 (three IMUs in the center of the sphere), despite the one more IMU, since the three IMUs placed on the outside provide worse results for the orientation determination accuracy.

Experiment	D1	D2	D3
RMSE [rad]	0.3361	0.4082	0.3736

Table 5.13: End results of Experiment D. Merged RMSE for each configuration.

From the results, we derive the following configurations for the individual robot types. For **pendulum based robots** we recommend placing five IMUs in the shell anywhere on the rotational axes and/or on the pendulum's axis. Since the distance between an off centered IMU and the center of the sphere, as well as symmetrical placement of the IMUs, does not affect the orientation determination accuracy, it does not matter whether we place the IMUs on the pendulum's axis or on the very outside, and how we attach them to the axes of rotation. By using five IMUs, however, we get a more precise orientation than if we used fewer, for example, only three IMUs (one on each axis of rotation). If we need a well balanced robot, we recommend using six IMUs, because six IMUs are better to evenly distribute than five IMUs and the mechanical and electrical overhead by using one more IMU is low. This approach for a well balanced robot applies for all following types, where we recommend using five off centered IMUs. For **spherical robots with an IDU** we suggest placing five IMUs on the rotational axes in the sphere's shell. The distribution of the IMUs on the rotational axes does not matter, because symmetrical placement of the IMUs, does not affect the orientation determination accuracy. A similar situation applies for **robots with shifting masses**. Here, too, we follow the approach of using five IMUs, because for more than five IMUs the improvement in the accuracy of the orientation determination is no longer significant. Since the off centered IMUs distances to the sphere's center seems to have no effect on the accuracy of the orientation determination, we place them anywhere on the rotational axes outside the shifting masses' reach, which is most likely in the shell. For **rod-driven robots including DAEDALUS**, it is best to place five IMUs in the sphere's center, because the orientation determination of an IMU is most accurate when we place them in the center of the sphere. Again, we use the approach of using five IMUs based on the results of Experiment A. The same approach applies for **robots using reaction wheels including L.U.N.A. or shell transformation**, where an individual placement for each specific robot is necessary. For L.U.N.A. it is not possible to place the IMUs in the center of the sphere due to the laser scanner, and also for DAEDALUS the scanner is best placed in the center. Therefore, the next best configuration for them is to place five IMUs off centered anywhere along the rotational axes. That configuration is not as accurate regarding orientation determination as placing them in the center of the sphere, but it allows the placement of the scanner in the center.

Chapter 6

Conclusions

In this thesis, we evaluated the quantity and positioning of IMUs for different spherical robot types regarding the orientation determination. We performed four experiments to test different aspects of number and positioning of the IMUs. We have answered how the following aspects affect the accuracy of the orientation determination:

- A) number of IMUs,
- B) distance of an IMU from the sphere's center,
- C) symmetrical placement of IMUs,
- D) and axial placement compared to centered placement of the IMUs.

From this we derived configurations for the different spherical robot types.

The results show the expected trends, but the reference value (RMSE) is very high for all performed experiments. In comparison to e.g. [13] our RMSEs are two orders of magnitude higher. This is due to the performance of the movements of the open sphere by hand, which we tried to carry out as equal as possible but were never truly the same. Furthermore, the movements were restricted due to the open shell. It seems better to use a machine, such as a robotic arm, to move the construction for further research. Also, the Optitrack system provided more imprecise orientations for the ground truth than expected. By using a robotic arm to rotate the construction, the ground truth becomes the exact programmed rotation and therefore more accurate than the orientation provided by the Optitrack system. Furthermore, it would not require a coordinate transformation of the ground truth data, which reduces the workload. The basic conclusions were found, but e.g. the exact connection between the distance of an off centered IMU and the center of the sphere and the orientation determination accuracy should be reestablished with a more precise ground truth. It is possible that the exact dependency is hidden behind the large error and that we are not able to evaluate it with this imprecise ground truth. Further research may also include the usage of different IMUs to elaborate the possible advantages due to temporal diversity and redundancy for FDIR.

Appendix A

Raw Data Plots

A.1 Experiment A

Configuration A1: One IMU in the center of the sphere

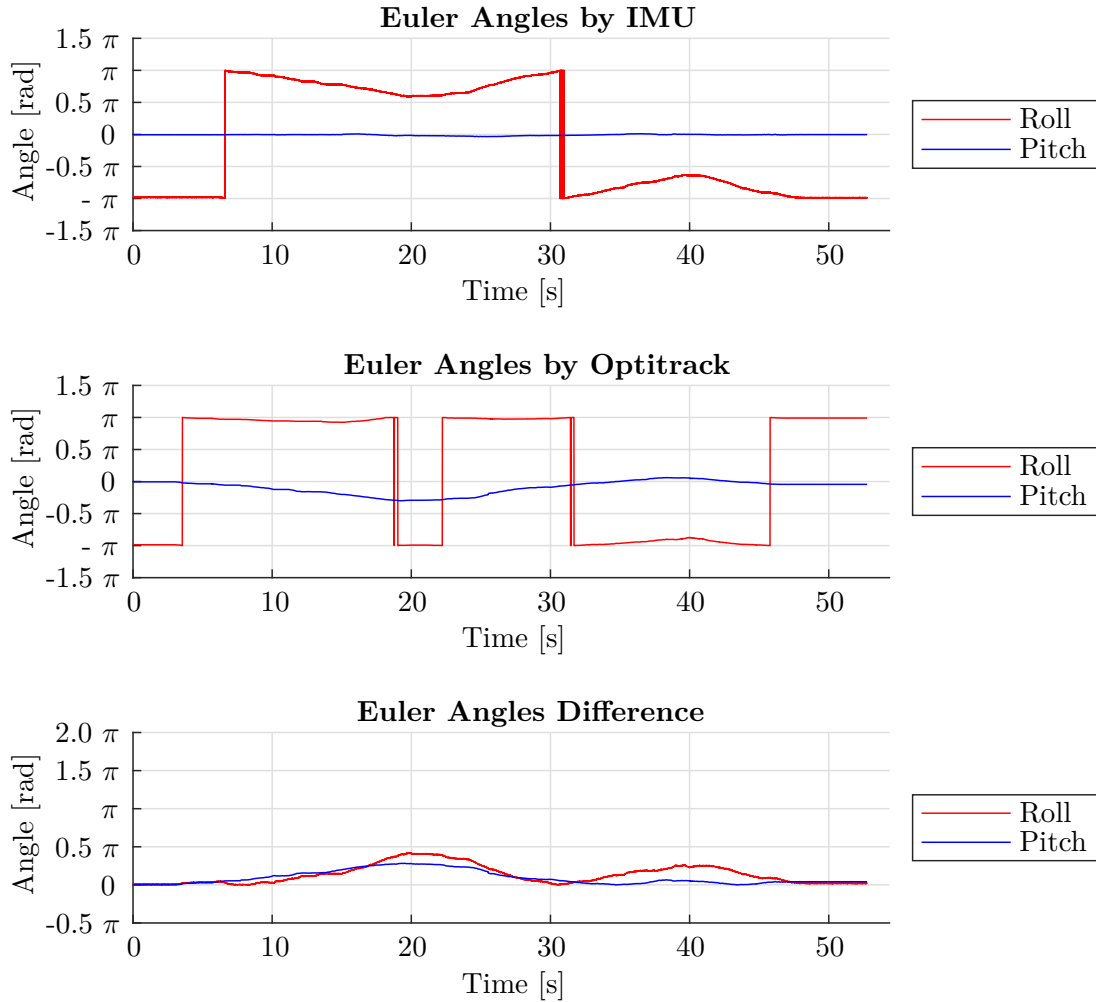


Figure A.1: Euler Angles obtained during the first experiment of Experiment A Configuration 1. Roll rotation with one IMU in the center of the sphere. Top: Euler Angles determined with the IMU data and the filter. Middle: Orientation recorded from the Optitrack system. Bottom: Absolute Euler Angles difference (Ground truth minus IMU). The Euler Angles are Roll (red), Pitch (blue) and Yaw (green) plotted against time.

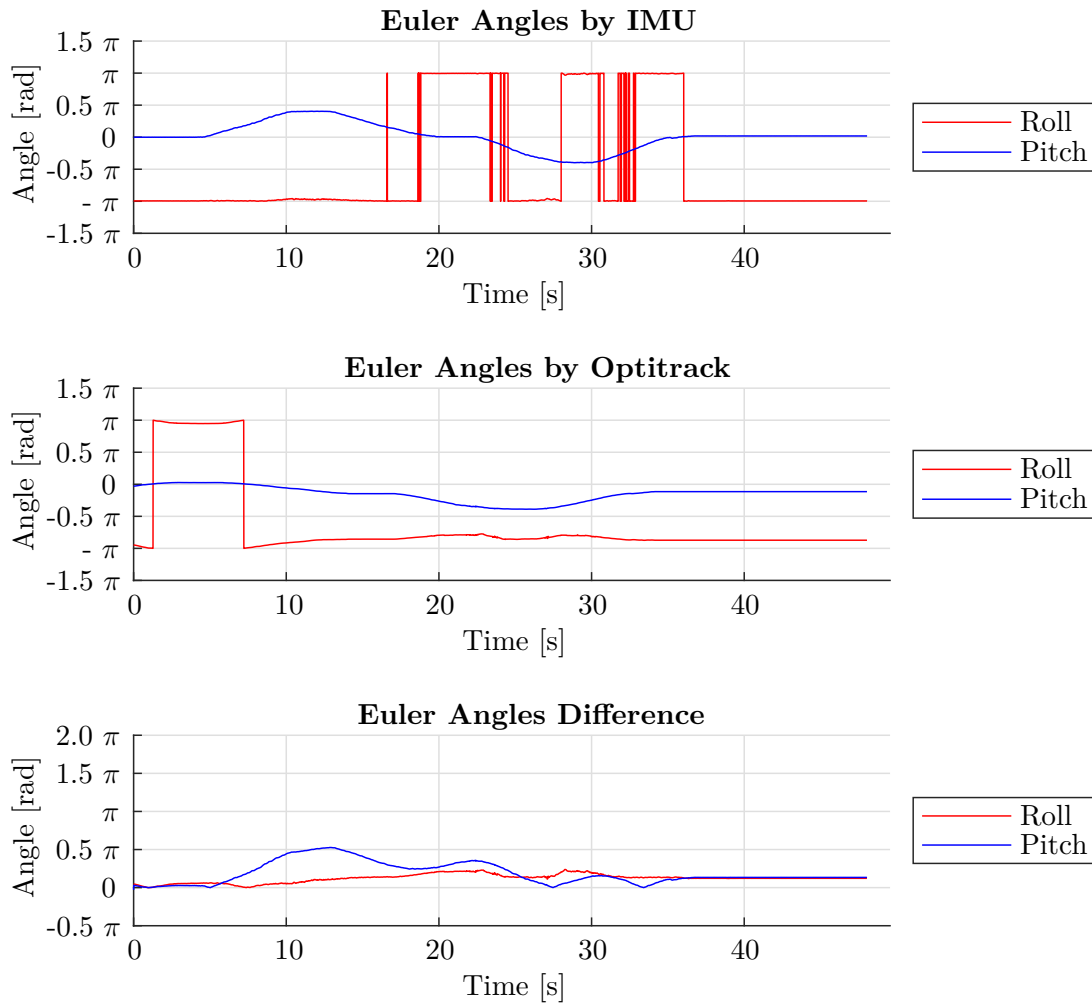


Figure A.2: Euler Angles obtained during the second experiment of Experiment A Configuration 1. Pitch rotation with one IMU in the center of the sphere. Top: Euler Angles determined with the IMU data and the filter. Middle: Orientation recorded from the Optitrack system. Bottom: Absolute Euler Angles difference (Ground truth minus IMU). The Euler Angles are Roll (red), Pitch (blue) and Yaw (green) plotted against time.

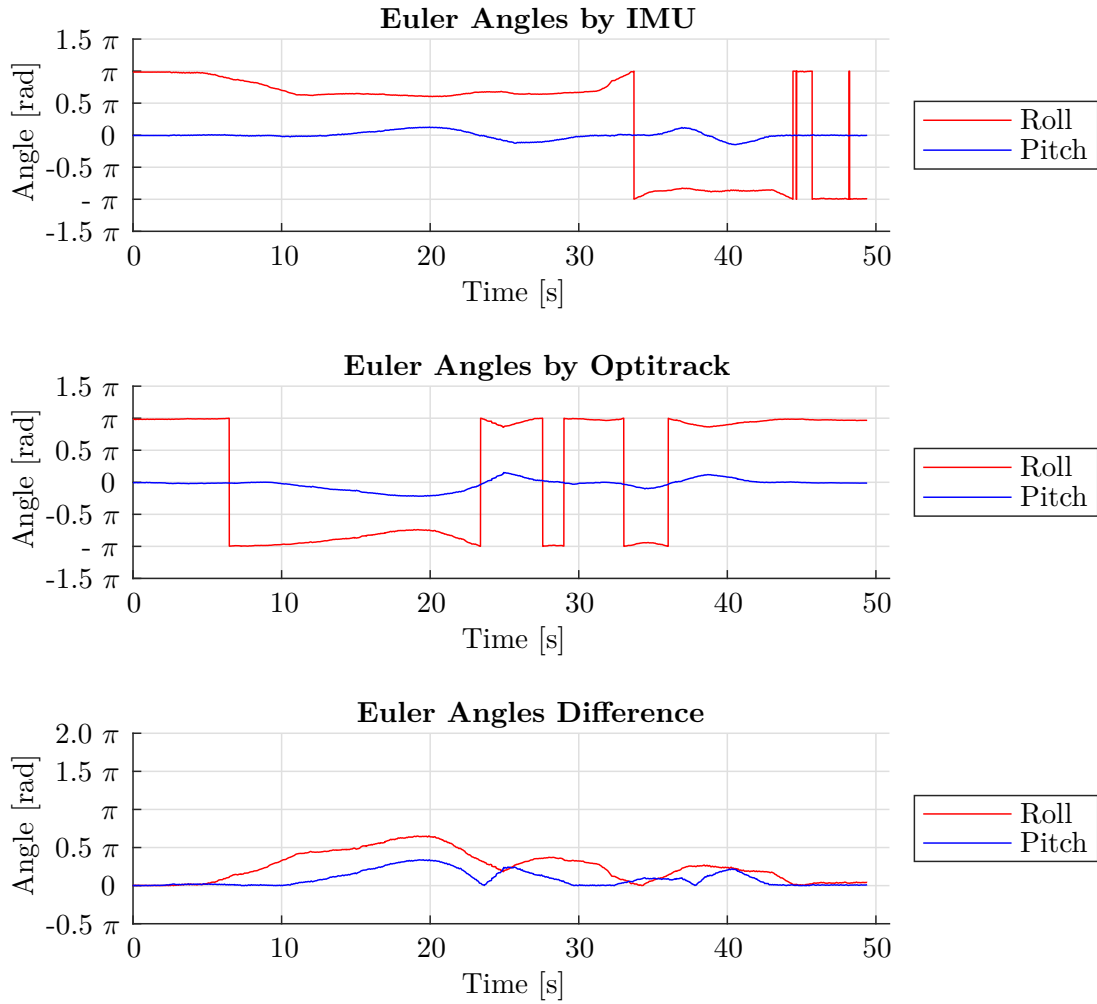


Figure A.3: Euler Angles obtained during the third experiment of Experiment A Configuration 1. Roll and Pitch rotation with one IMU in the center of the sphere. Top: Euler Angles determined with the IMU data and the filter. Middle: Orientation recorded from the Optitrack system. Bottom: Absolute Euler Angles difference (Ground truth minus IMU). The Euler Angles are Roll (red), Pitch (blue) and Yaw (green) plotted against time.

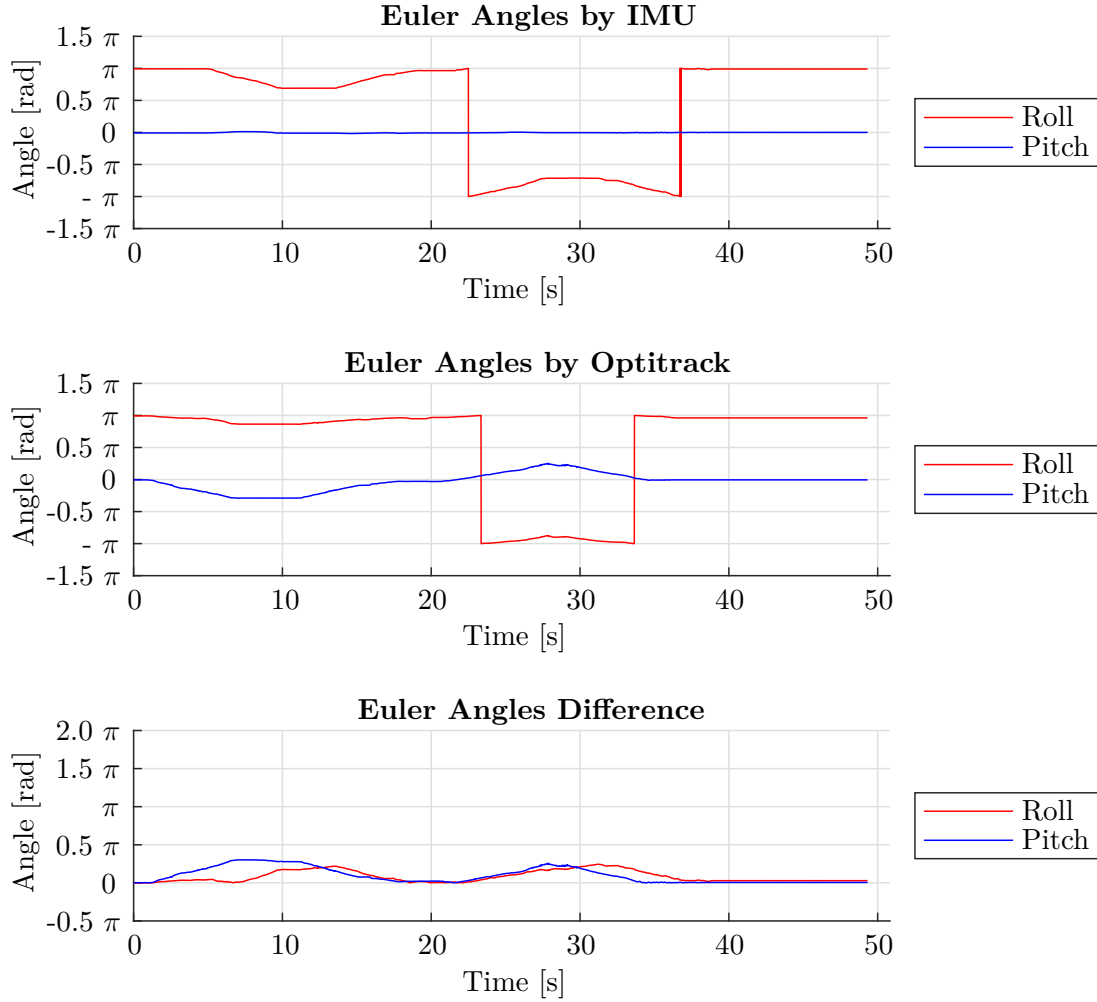
Configuration A2: Two IMUs in the center of the sphere

Figure A.4: Euler Angles obtained during the first experiment of Experiment A Configuration 2. Roll rotation with two IMUs in the center of the sphere. Top: Euler Angles determined with the IMU data and the filter. Middle: Orientation recorded from the Optitrack system. Bottom: Absolute Euler Angles difference (Ground truth minus IMU). The Euler Angles are Roll (red), Pitch (blue) and Yaw (green) plotted against time.

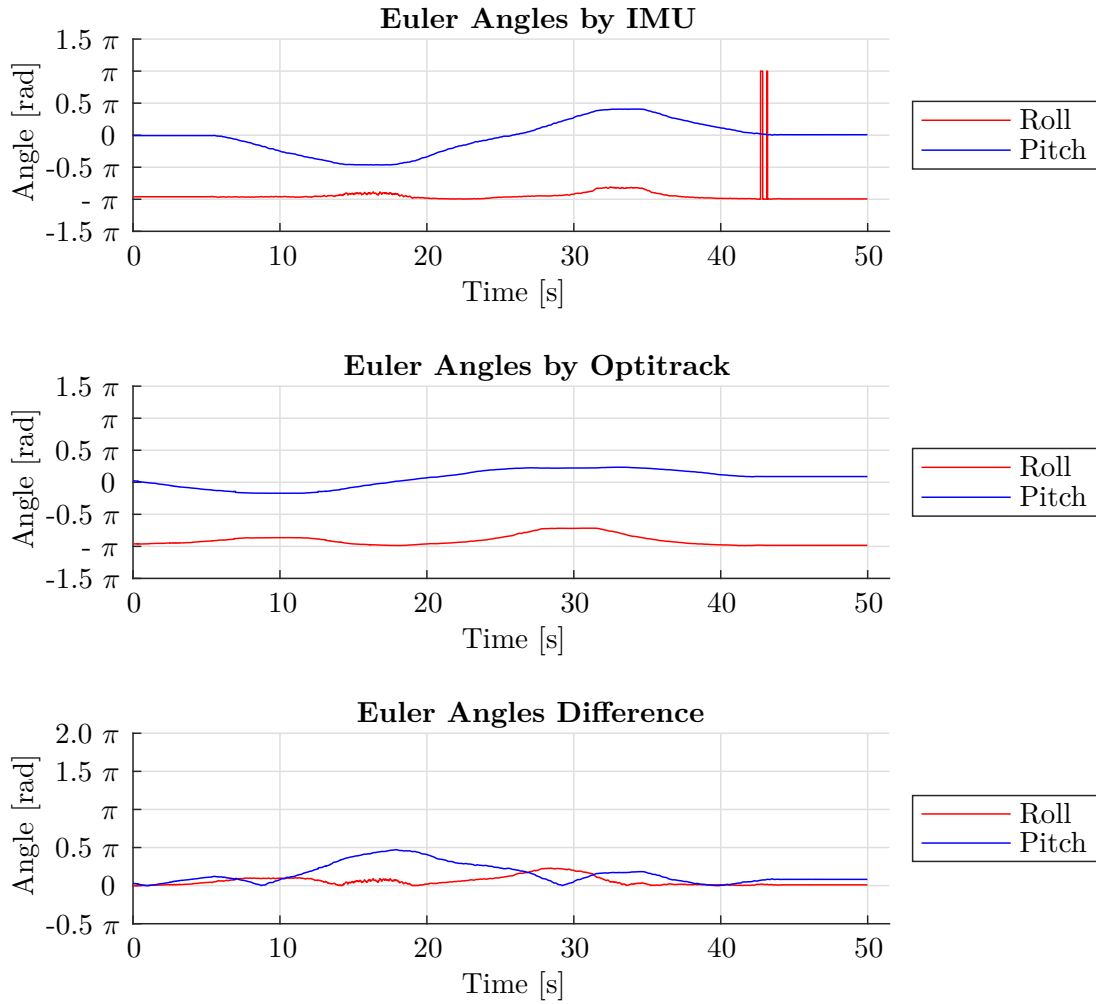


Figure A.5: Euler Angles obtained during the second experiment of Experiment A Configuration 2. Pitch rotation with two IMUs in the center of the sphere. Top: Euler Angles determined with the IMU data and the filter. Middle: Orientation recorded from the Optitrack system. Bottom: Absolute Euler Angles difference (Ground truth minus IMU). The Euler Angles are Roll (red), Pitch (blue) and Yaw (green) plotted against time.

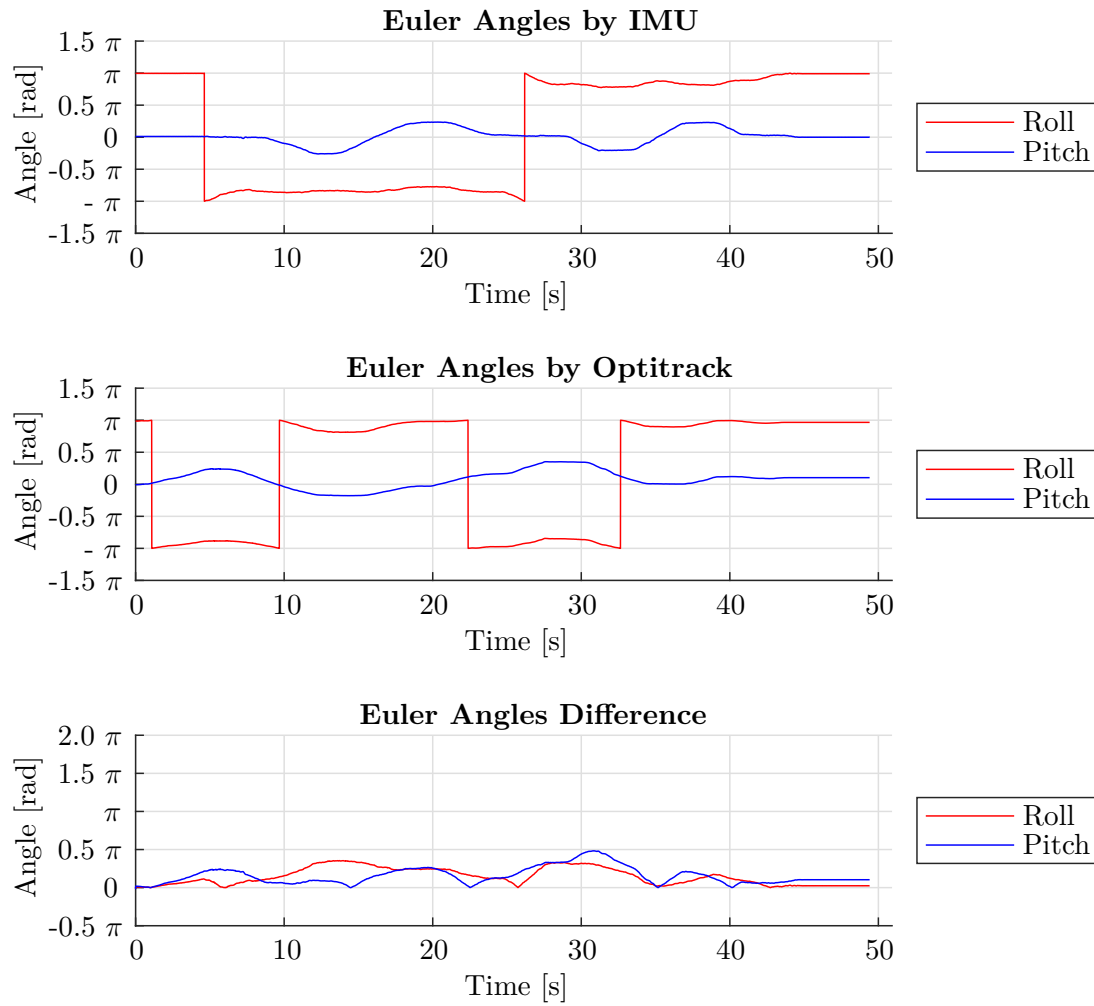


Figure A.6: Euler Angles obtained during the third experiment of Experiment A Configuration 2. Roll and Pitch rotation with two IMUs in the center of the sphere. Top: Euler Angles determined with the IMU data and the filter. Middle: Orientation recorded from the Optitrack system. Bottom: Absolute Euler Angles difference (Ground truth minus IMU). The Euler Angles are Roll (red), Pitch (blue) and Yaw (green) plotted against time.

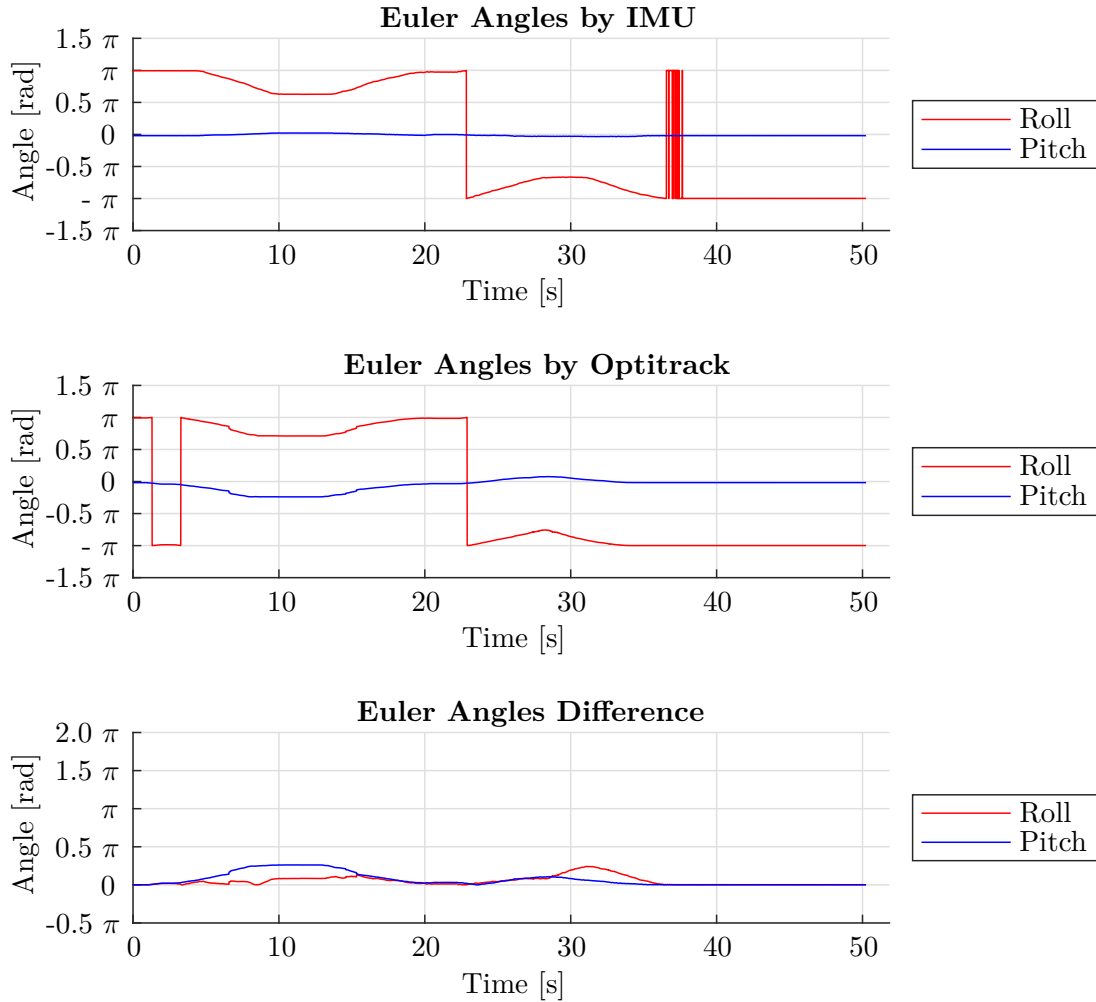
Configuration A3: Three IMUs in the center of the sphere

Figure A.7: Euler Angles obtained during the first experiment of Experiment A Configuration 3. Roll rotation with three IMUs in the center of the sphere. Top: Euler Angles determined with the IMU data and the filter. Middle: Orientation recorded from the Optitrack system. Bottom: Absolute Euler Angles difference (Ground truth minus IMU). The Euler Angles are Roll (red), Pitch (blue) and Yaw (green) plotted against time.

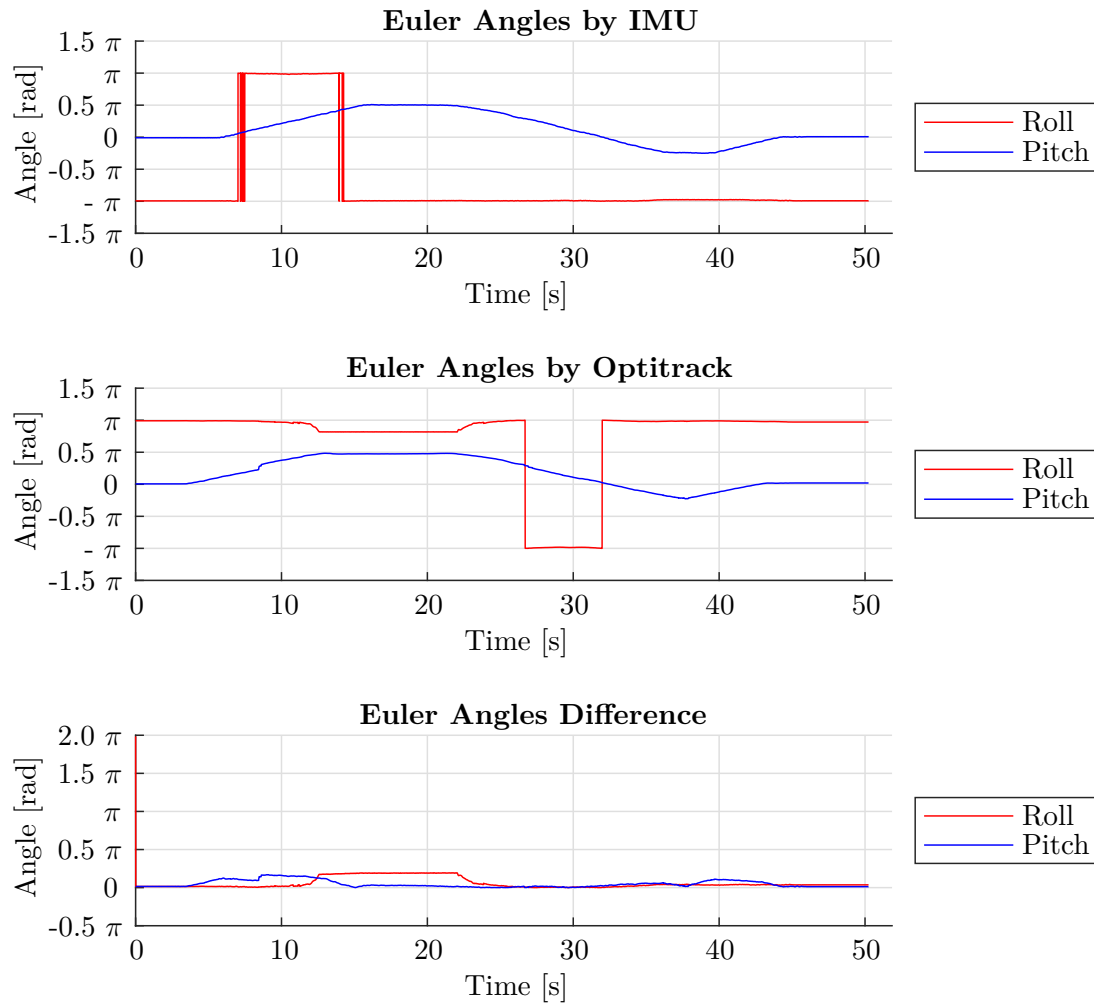


Figure A.8: Euler Angles obtained during the second experiment of Experiment A Configuration 3. Pitch rotation with three IMUs in the center of the sphere. Top: Euler Angles determined with the IMU data and the filter. Middle: Orientation recorded from the Optitrack system. Bottom: Absolute Euler Angles difference (Ground truth minus IMU). The Euler Angles are Roll (red), Pitch (blue) and Yaw (green) plotted against time.

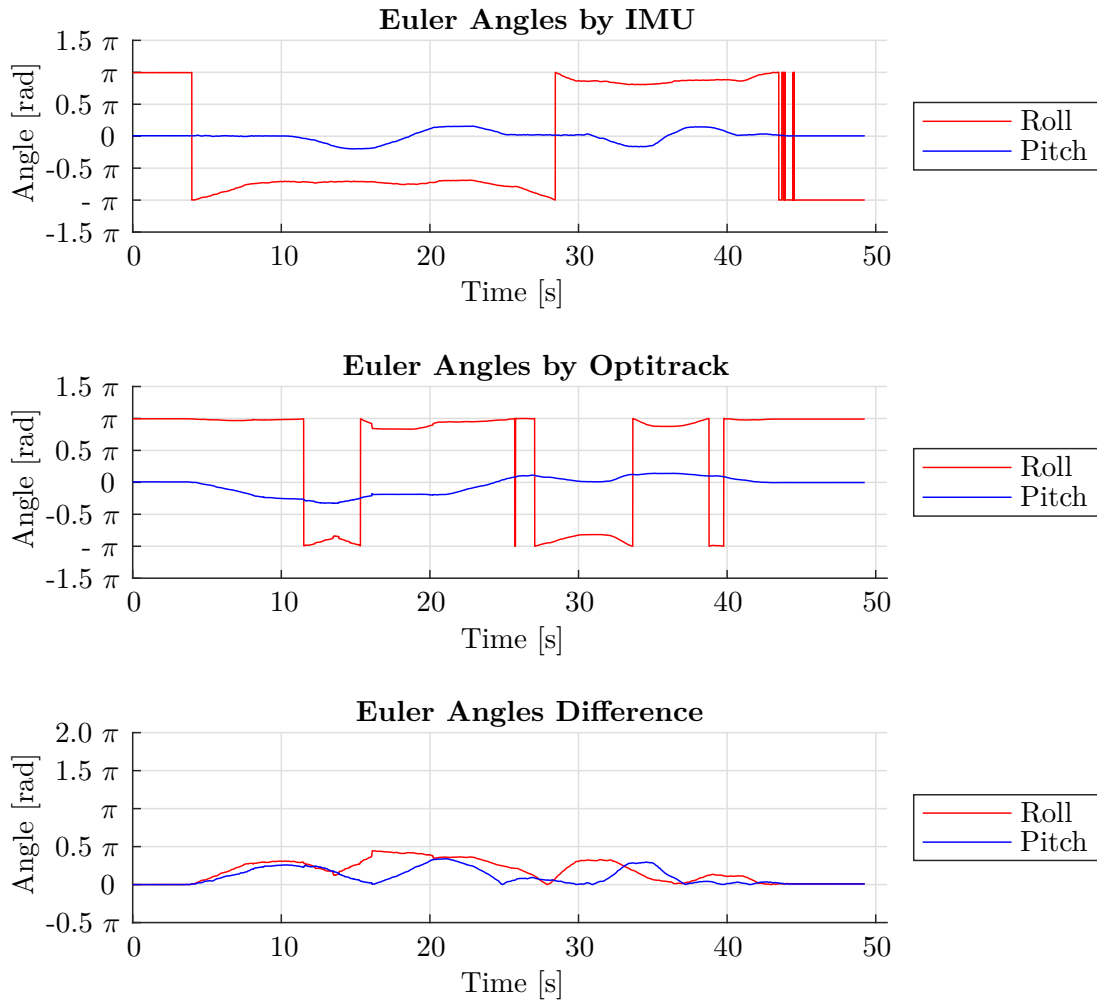


Figure A.9: Euler Angles obtained during the third experiment of Experiment A Configuration 3. Roll and Pitch rotation with three IMUs in the center of the sphere. Top: Euler Angles determined with the IMU data and the filter. Middle: Orientation recorded from the Optitrack system. Bottom: Absolute Euler Angles difference (Ground truth minus IMU). The Euler Angles are Roll (red), Pitch (blue) and Yaw (green) plotted against time.

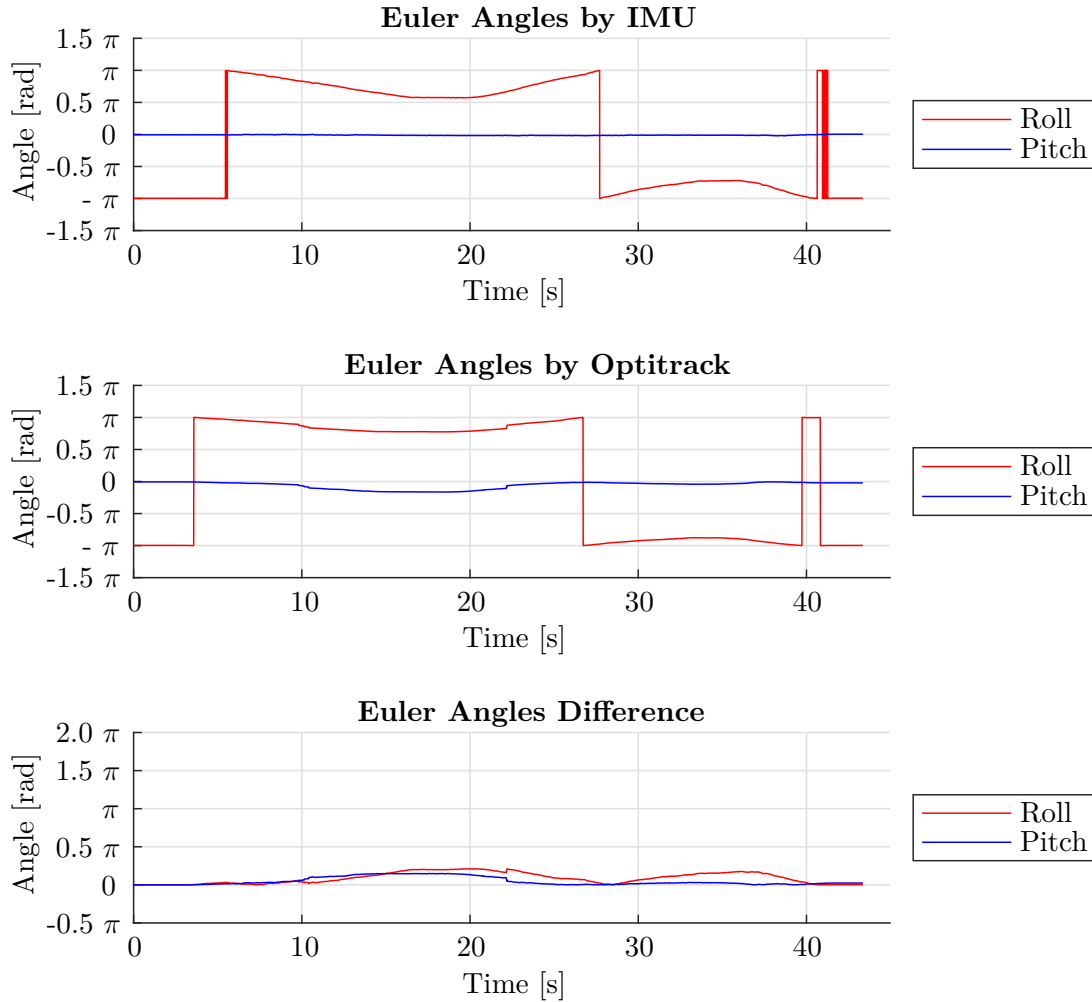
Configuration A4: Four IMUs in the center of the sphere

Figure A.10: Euler Angles obtained during the first experiment of Experiment A Configuration 4. Roll rotation with four IMUs in the center of the sphere. Top: Euler Angles determined with the IMU data and the filter. Middle: Orientation recorded from the Optitrack system. Bottom: Absolute Euler Angles difference (Ground truth minus IMU). The Euler Angles are Roll (red), Pitch (blue) and Yaw (green) plotted against time.

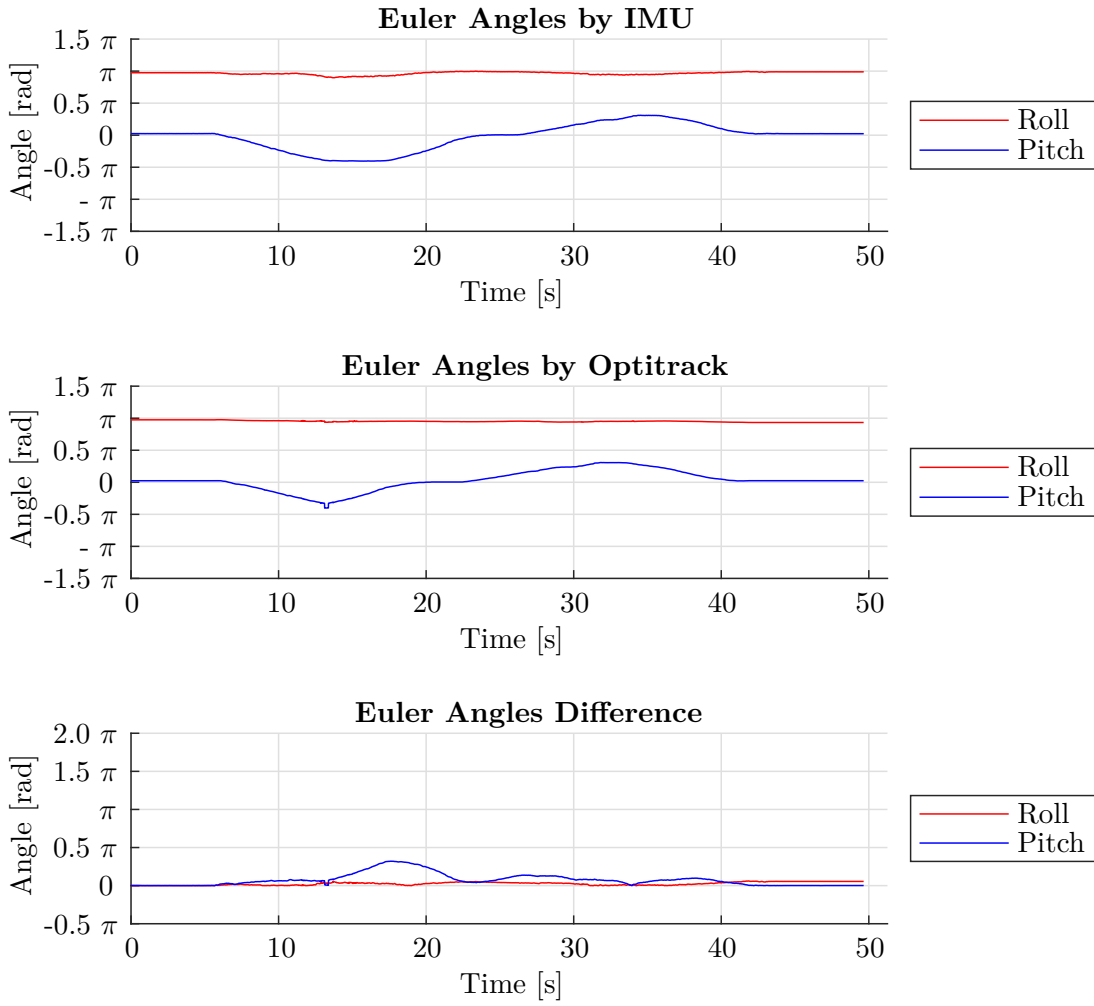


Figure A.11: Euler Angles obtained during the second experiment of Experiment A Configuration 4. Pitch rotation with four IMUs in the center of the sphere. Top: Euler Angles determined with the IMU data and the filter. Middle: Orientation recorded from the Optitrack system. Bottom: Absolute Euler Angles difference (Ground truth minus IMU). The Euler Angles are Roll (red), Pitch (blue) and Yaw (green) plotted against time.

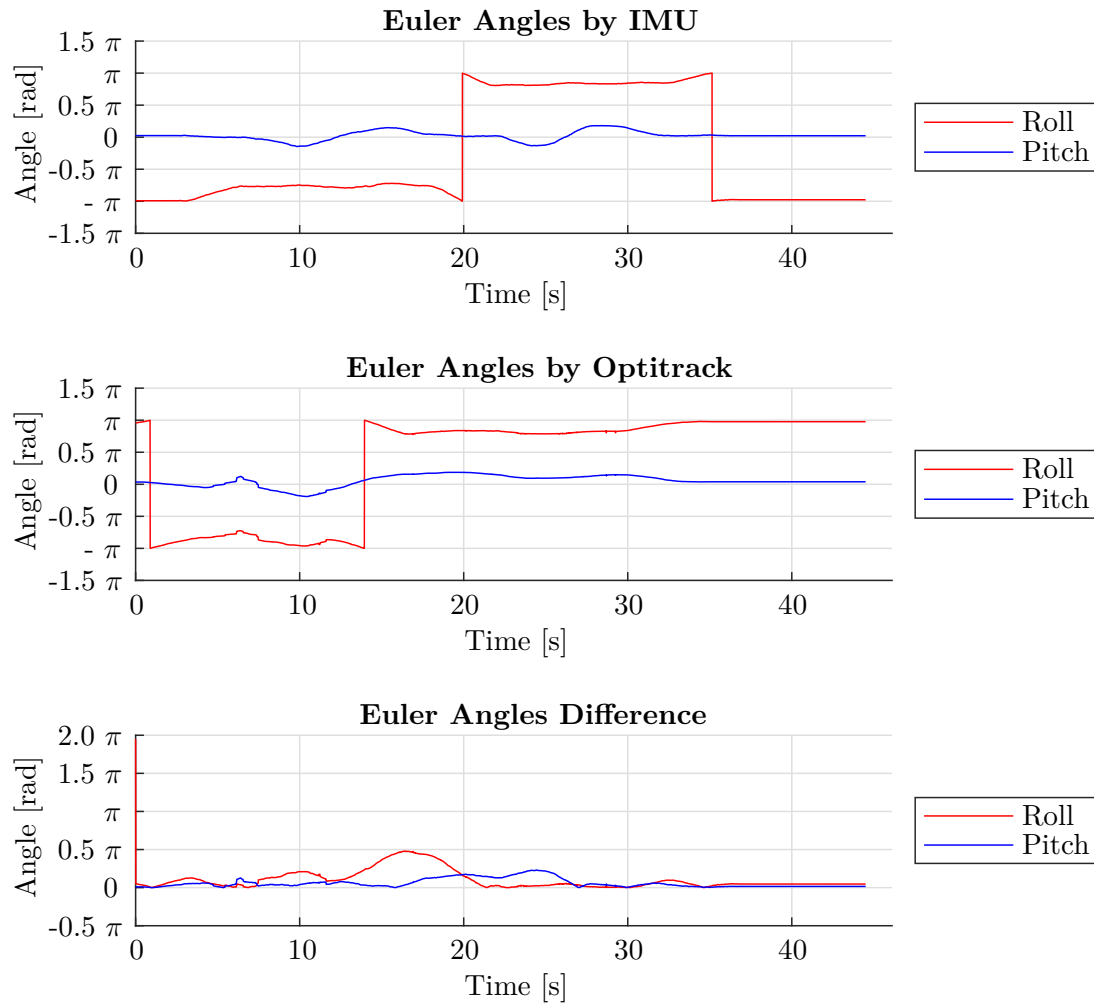


Figure A.12: Euler Angles obtained during the third experiment of Experiment A Configuration 4. Roll and Pitch rotation with four IMUs in the center of the sphere. Top: Euler Angles determined with the IMU data and the filter. Middle: Orientation recorded from the Optitrack system. Bottom: Absolute Euler Angles difference (Ground truth minus IMU). The Euler Angles are Roll (red), Pitch (blue) and Yaw (green) plotted against time.

Configuration A5: Five IMUs in the center of the sphere

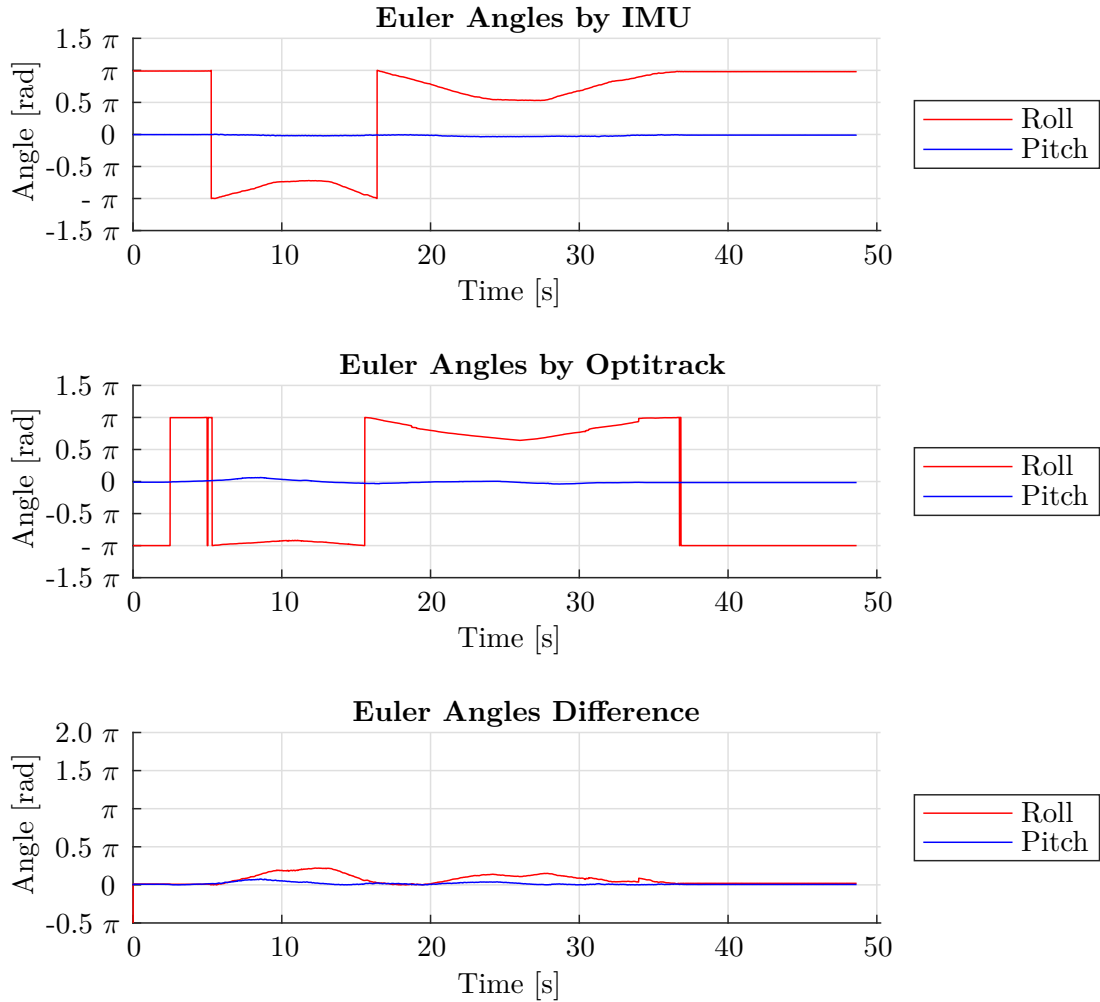


Figure A.13: Euler Angles obtained during the first experiment of Experiment A Configuration 5. Roll rotation with five IMUs in the center of the sphere. Top: Euler Angles determined with the IMU data and the filter. Middle: Orientation recorded from the Optitrack system. Bottom: Absolute Euler Angles difference (Ground truth minus IMU). The Euler Angles are Roll (red), Pitch (blue) and Yaw (green) plotted against time.

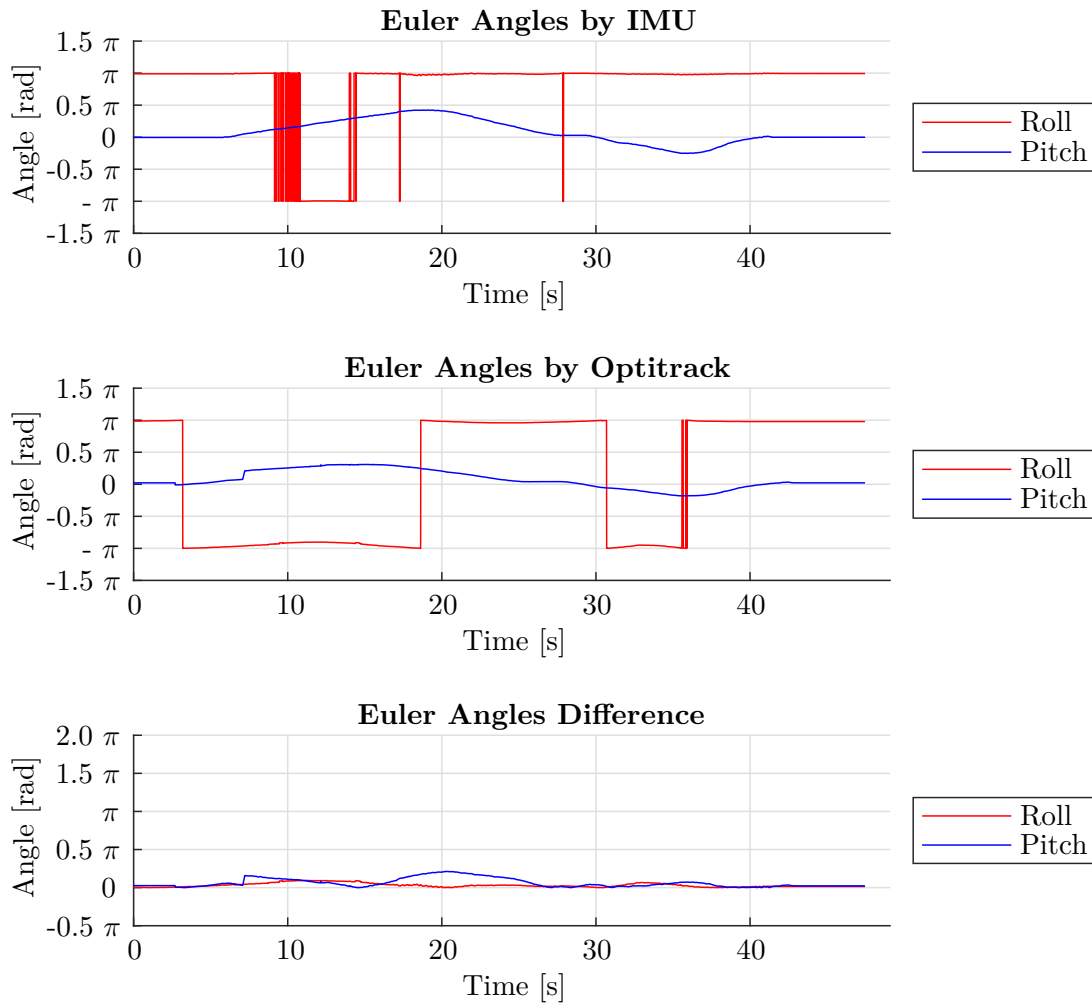


Figure A.14: Euler Angles obtained during the second experiment of Experiment A Configuration 5. Pitch rotation with five IMUs in the center of the sphere. Top: Euler Angles determined with the IMU data and the filter. Middle: Orientation recorded from the Optitrack system. Bottom: Absolute Euler Angles difference (Ground truth minus IMU). The Euler Angles are Roll (red), Pitch (blue) and Yaw (green) plotted against time.

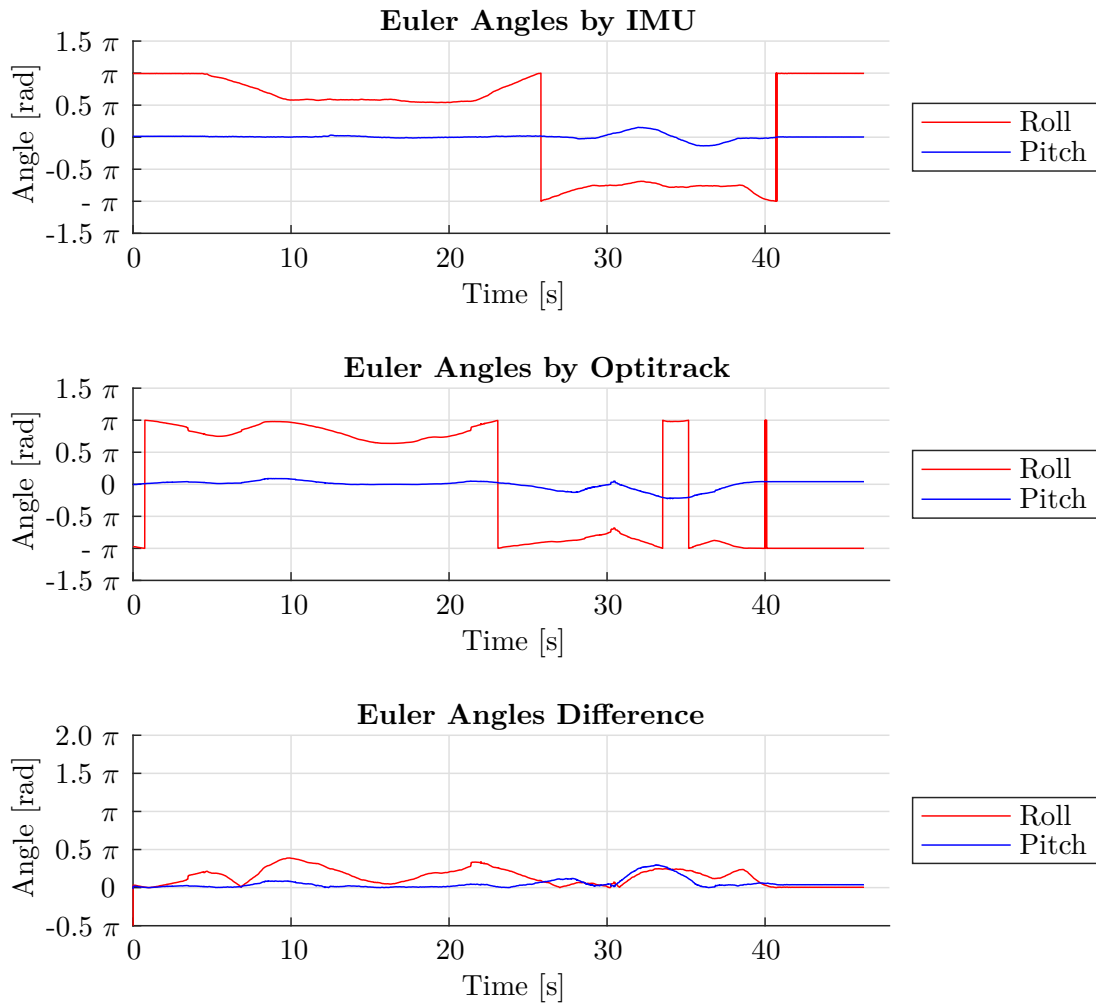


Figure A.15: Euler Angles obtained during the third experiment of Experiment A Configuration 5. Roll and Pitch rotation with five IMUs in the center of the sphere. Top: Euler Angles determined with the IMU data and the filter. Middle: Orientation recorded from the Optitrack system. Bottom: Absolute Euler Angles difference (Ground truth minus IMU). The Euler Angles are Roll (red), Pitch (blue) and Yaw (green) plotted against time.

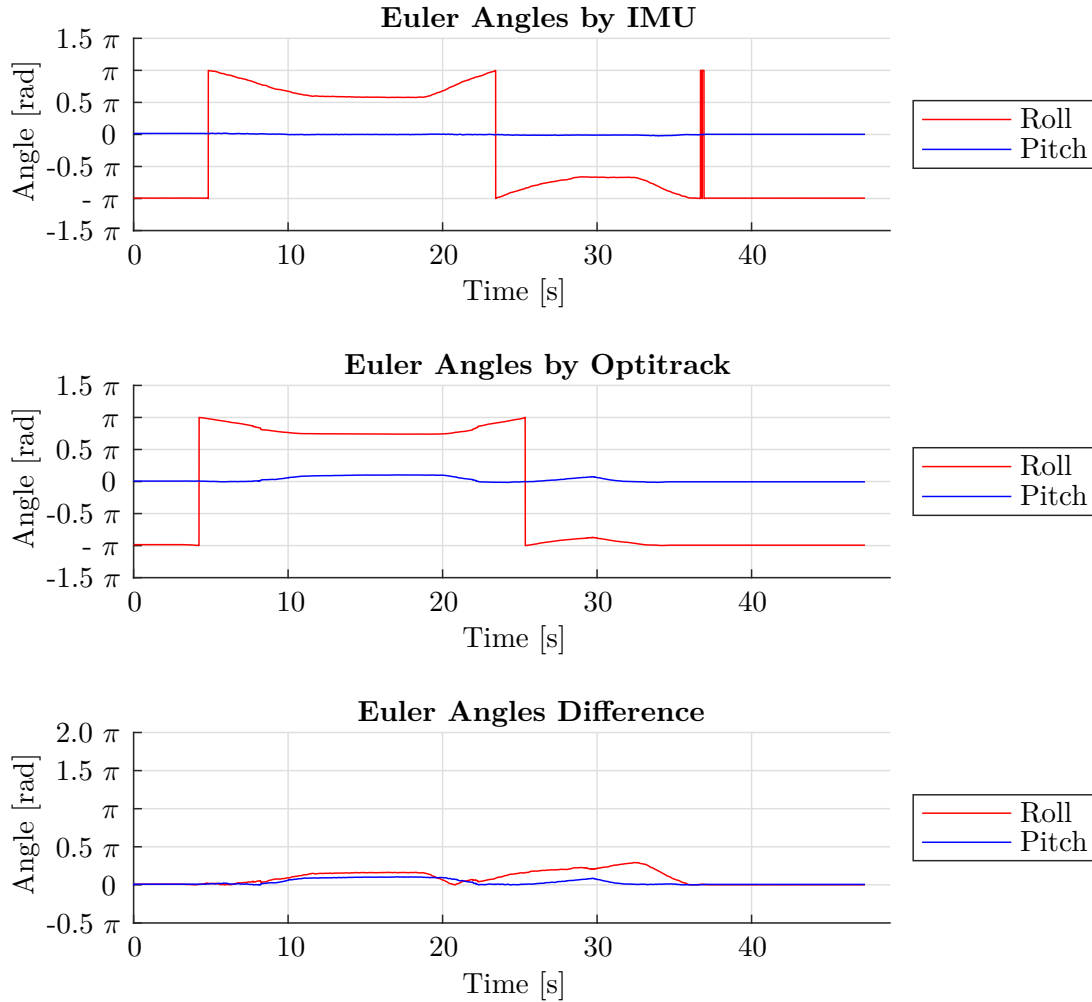
Configuration A6: Six IMUs in the center of the sphere

Figure A.16: Euler Angles obtained during the first experiment of Experiment A Configuration 6. Roll rotation with six IMUs in the center of the sphere. Top: Euler Angles determined with the IMU data and the filter. Middle: Orientation recorded from the Optitrack system. Bottom: Absolute Euler Angles difference (Ground truth minus IMU). The Euler Angles are Roll (red), Pitch (blue) and Yaw (green) plotted against time.

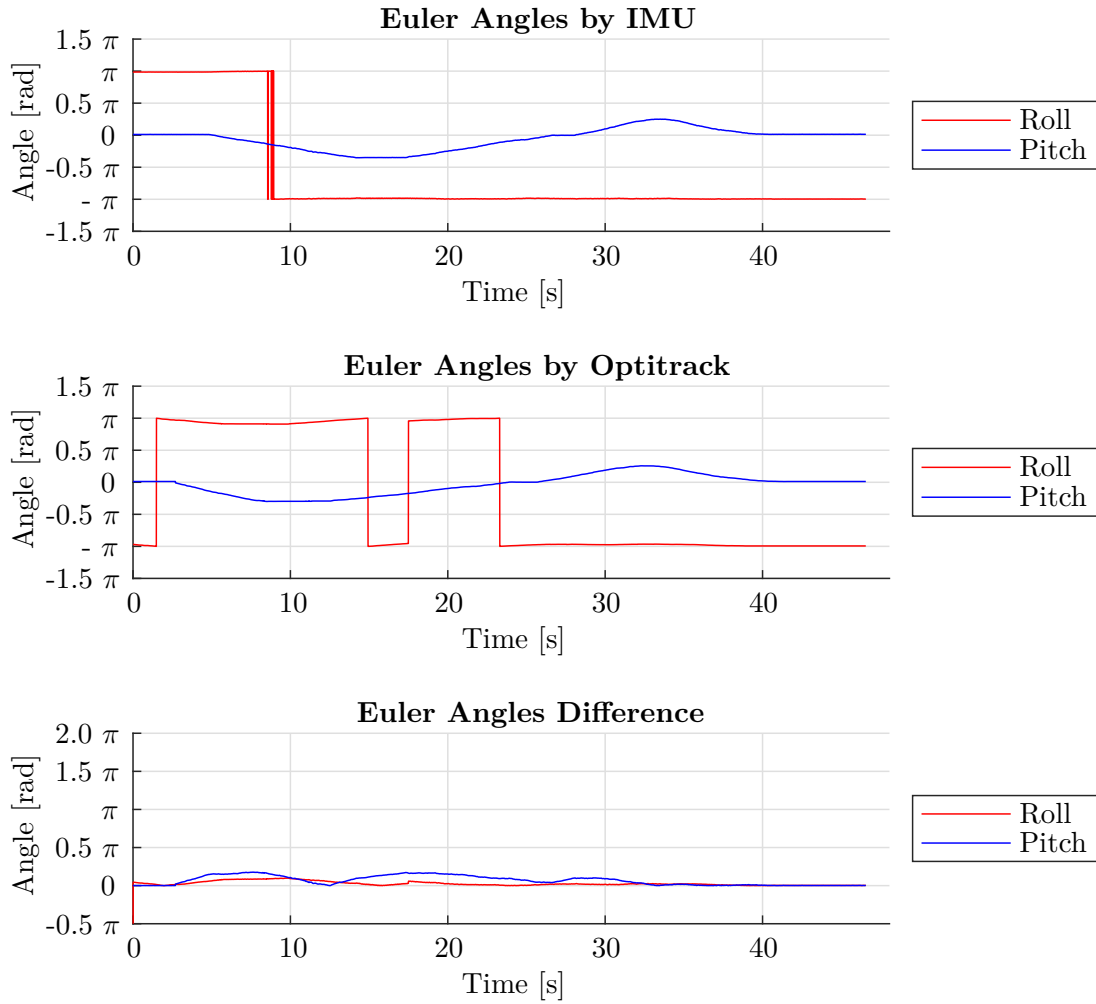


Figure A.17: Euler Angles obtained during the second experiment of Experiment A Configuration 6. Pitch rotation with six IMUs in the center of the sphere. Top: Euler Angles determined with the IMU data and the filter. Middle: Orientation recorded from the Optitrack system. Bottom: Absolute Euler Angles difference (Ground truth minus IMU). The Euler Angles are Roll (red), Pitch (blue) and Yaw (green) plotted against time.

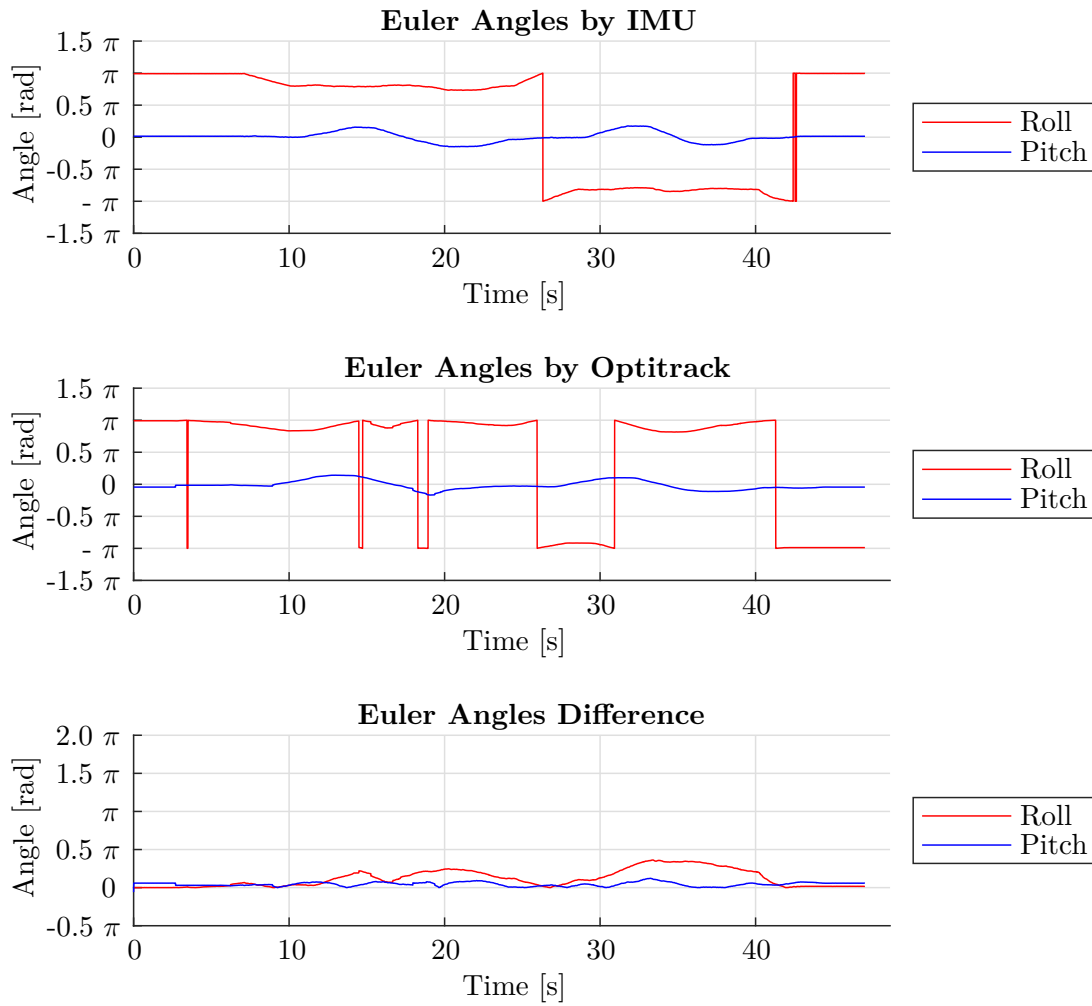


Figure A.18: Euler Angles obtained during the third experiment of Experiment A Configuration 6. Roll and Pitch rotation with six IMUs in the center of the sphere. Top: Euler Angles determined with the IMU data and the filter. Middle: Orientation recorded from the Optitrack system. Bottom: Absolute Euler Angles difference (Ground truth minus IMU). The Euler Angles are Roll (red), Pitch (blue) and Yaw (green) plotted against time.

A.2 Experiment B

Configuration B1: One IMU in the center of the sphere

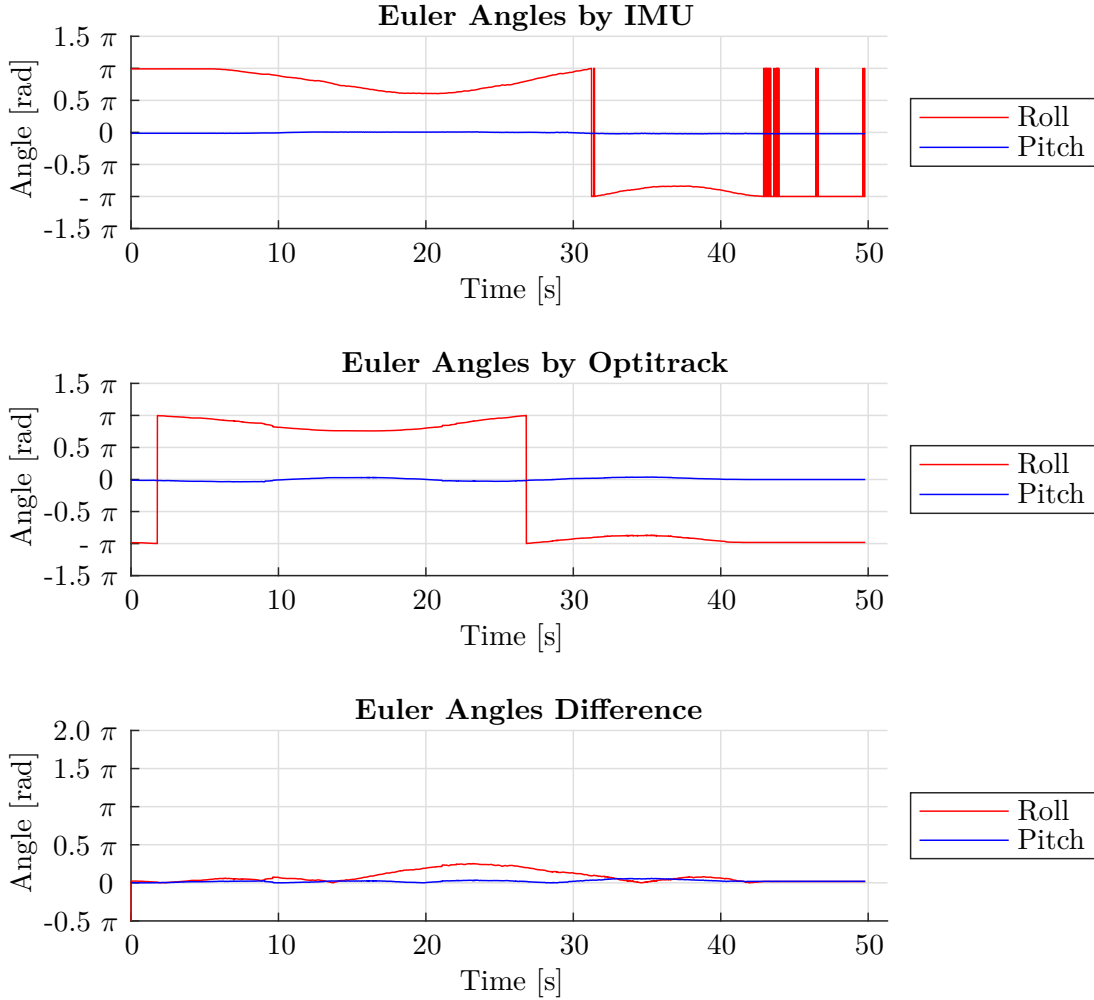


Figure A.19: Euler Angles obtained during the first experiment of Experiment B Configuration 1. Roll rotation with one IMU in the center of the sphere. Top: Euler Angles determined with the IMU data and the filter. Middle: Orientation recorded from the Optitrack system. Bottom: Absolute Euler Angles difference (Ground truth minus IMU). The Euler Angles are Roll (red), Pitch (blue) and Yaw (green) plotted against time.

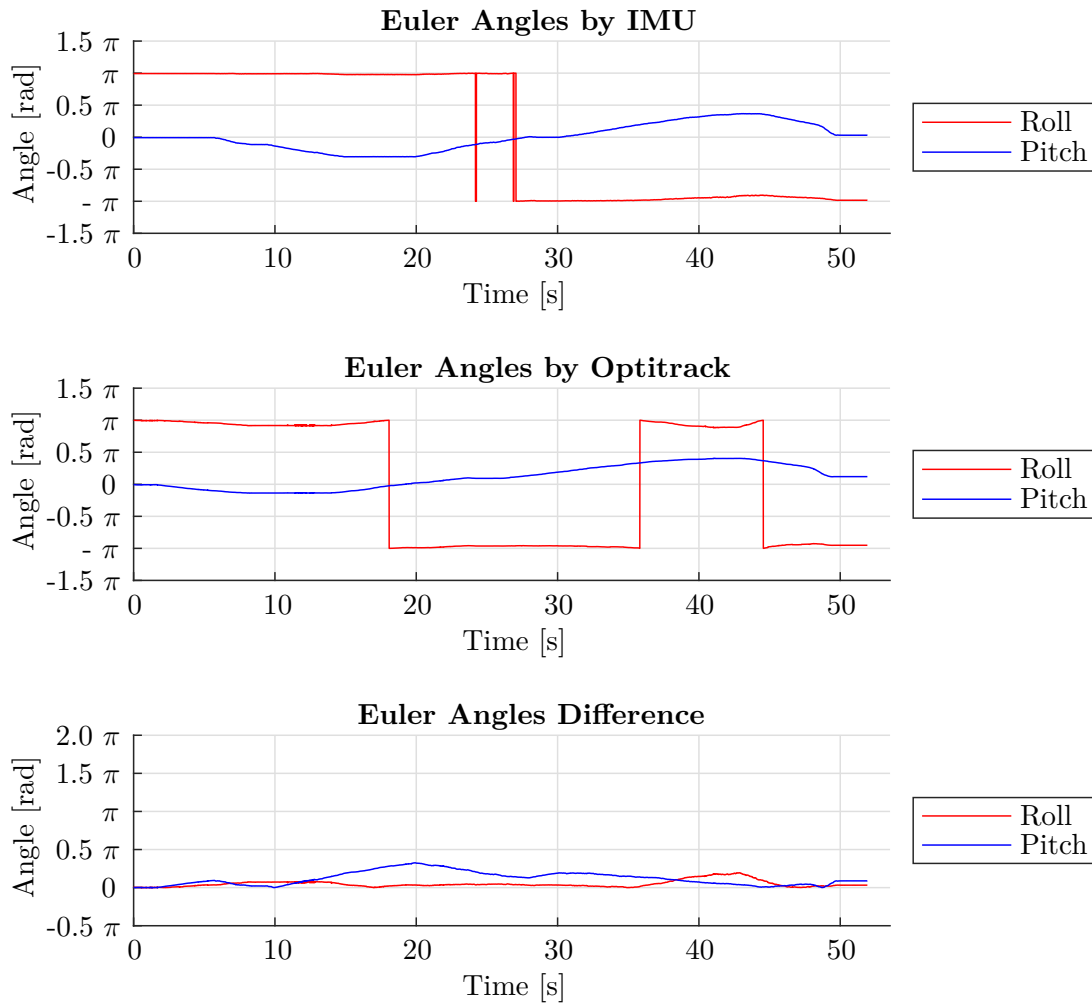


Figure A.20: Euler Angles obtained during the second experiment of Experiment B Configuration 1. Pitch rotation with one IMU in the center of the sphere. Top: Euler Angles determined with the IMU data and the filter. Middle: Orientation recorded from the Optitrack system. Bottom: Absolute Euler Angles difference (Ground truth minus IMU). The Euler Angles are Roll (red), Pitch (blue) and Yaw (green) plotted against time.

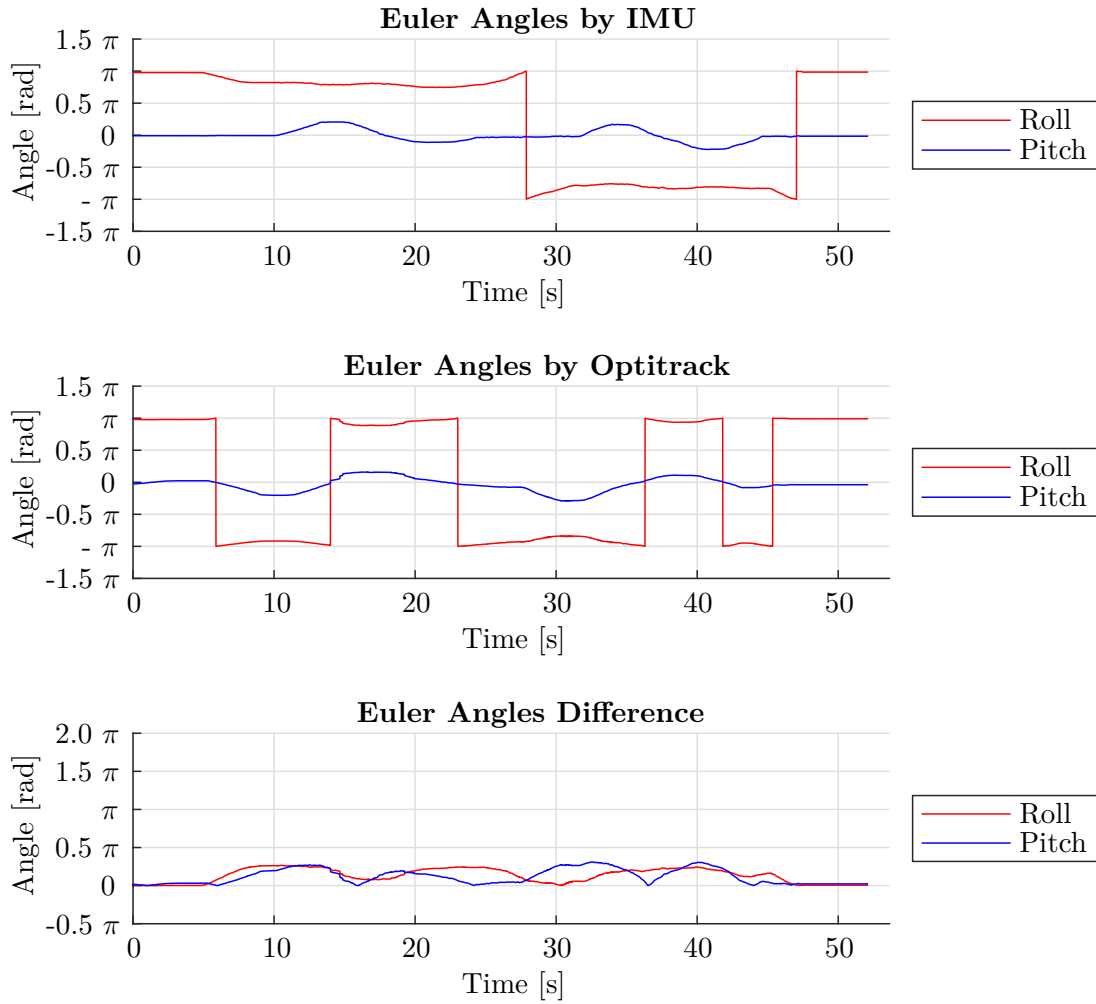


Figure A.21: Euler Angles obtained during the third experiment of Experiment B Configuration 1. Roll and Pitch rotation with one IMU in the center of the sphere. Top: Euler Angles determined with the IMU data and the filter. Middle: Orientation recorded from the Optitrack system. Bottom: Absolute Euler Angles difference (Ground truth minus IMU). The Euler Angles are Roll (red), Pitch (blue) and Yaw (green) plotted against time.

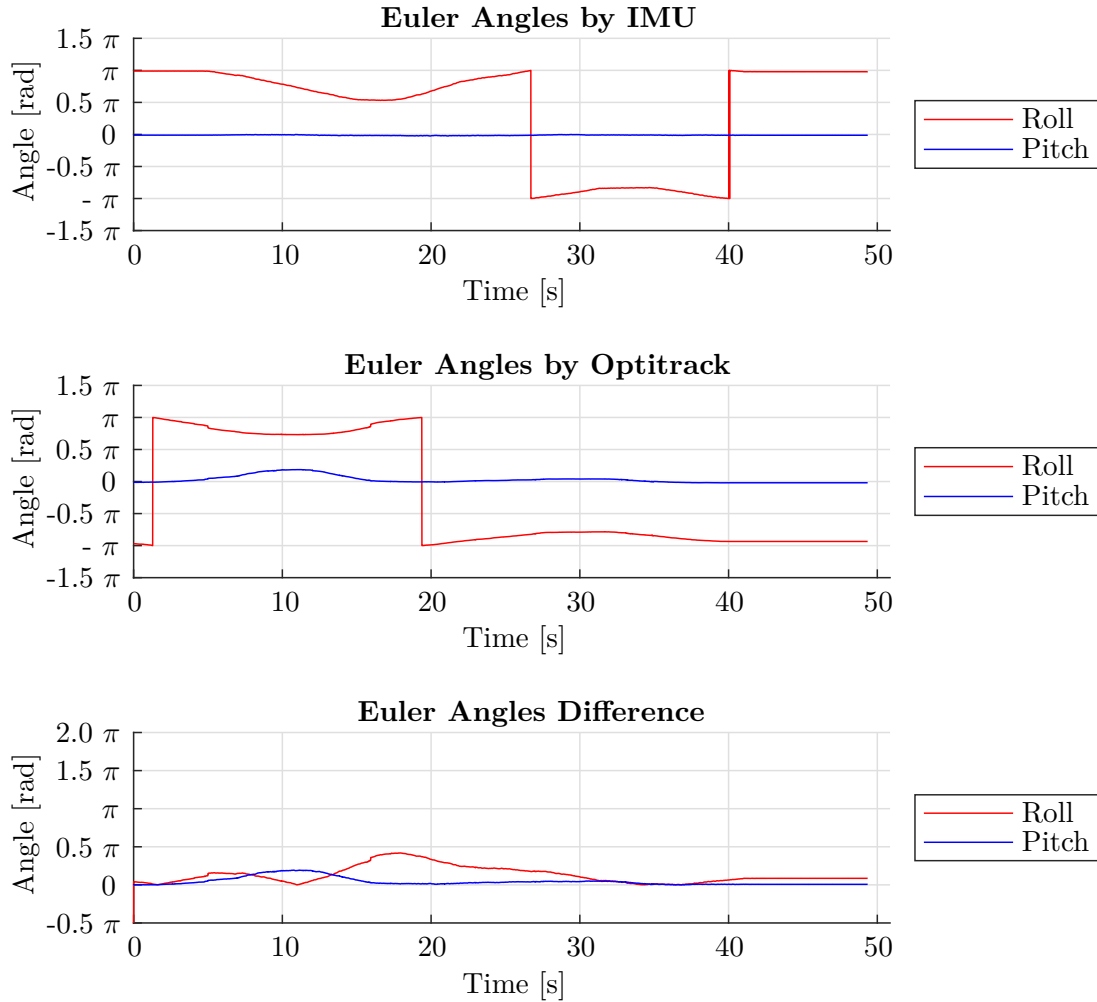
Configuration B2: One IMU at the distance of 4 cm from the center of the sphere

Figure A.22: Euler Angles obtained during the first experiment of Experiment B Configuration 2. Roll rotation with one IMU at the distance of 4 cm from the center of the sphere. Top: Euler Angles determined with the IMU data and the filter. Middle: Orientation recorded from the Optitrack system. Bottom: Absolute Euler Angles difference (Ground truth minus IMU). The Euler Angles are Roll (red), Pitch (blue) and Yaw (green) plotted against time.

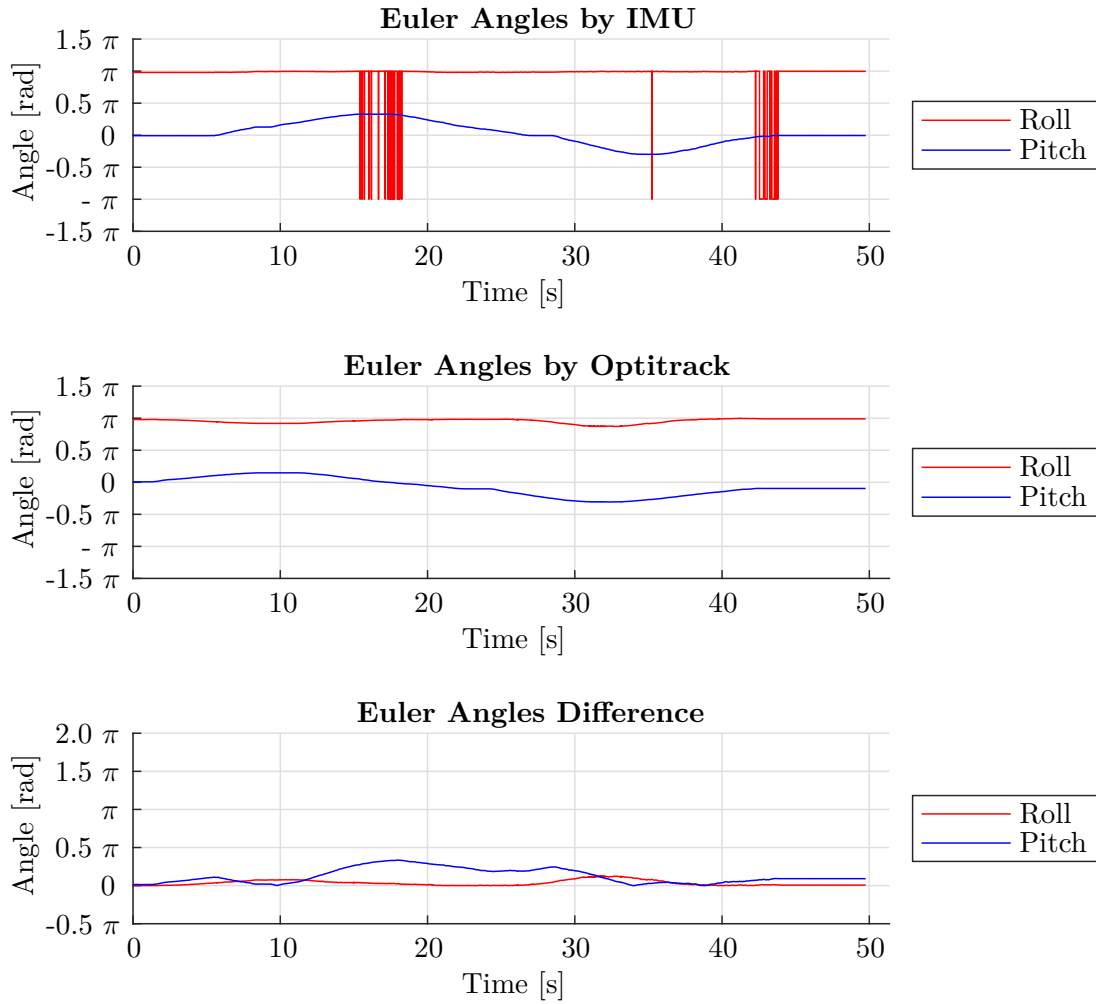


Figure A.23: Euler Angles obtained during the second experiment of Experiment B Configuration 2. Pitch rotation with one IMU at the distance of 4 cm from the center of the sphere. Top: Euler Angles determined with the IMU data and the filter. Middle: Orientation recorded from the Optitrack system. Bottom: Absolute Euler Angles difference (Ground truth minus IMU). The Euler Angles are Roll (red), Pitch (blue) and Yaw (green) plotted against time.

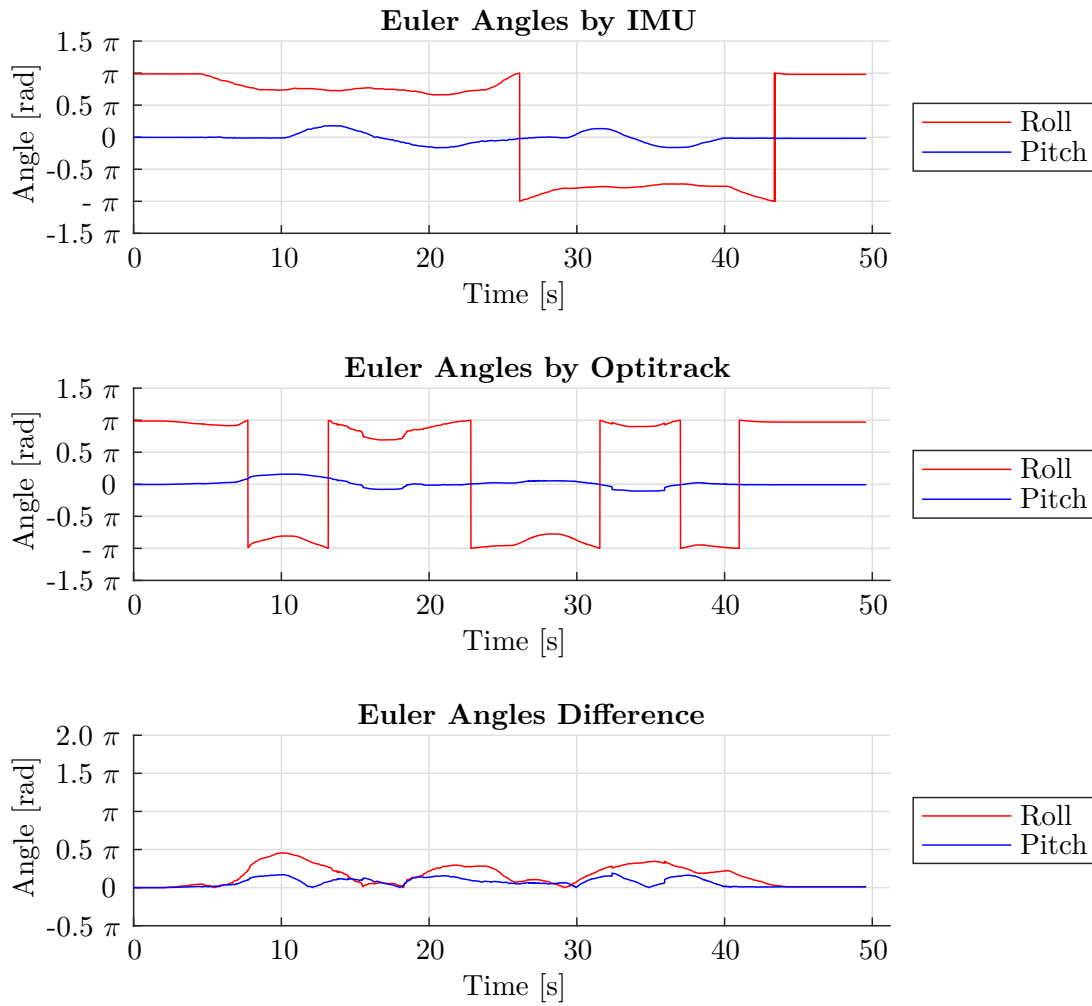


Figure A.24: Euler Angles obtained during the third experiment of Experiment B Configuration 2. Roll and Pitch rotation with one IMU at the distance of 4 cm from the center of the sphere. Top: Euler Angles determined with the IMU data and the filter. Middle: Orientation recorded from the Optitrack system. Bottom: Absolute Euler Angles difference (Ground truth minus IMU). The Euler Angles are Roll (red), Pitch (blue) and Yaw (green) plotted against time.

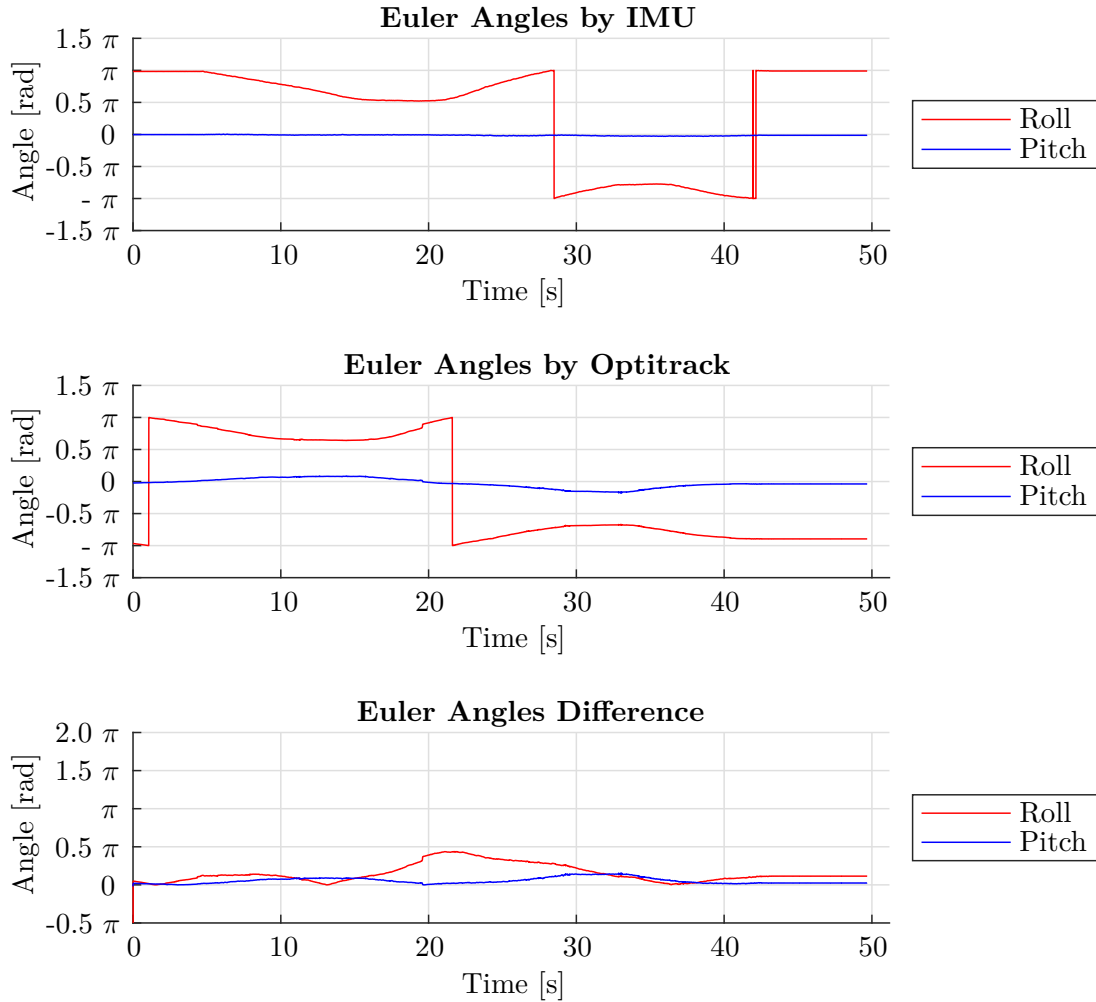
Configuration B3: One IMU at the distance of 8 cm from the center of the sphere

Figure A.25: Euler Angles obtained during the first experiment of Experiment B Configuration 3. Roll rotation with one IMU at the distance of 8 cm from the center of the sphere. Top: Euler Angles determined with the IMU data and the filter. Middle: Orientation recorded from the Optitrack system. Bottom: Absolute Euler Angles difference (Ground truth minus IMU). The Euler Angles are Roll (red), Pitch (blue) and Yaw (green) plotted against time.

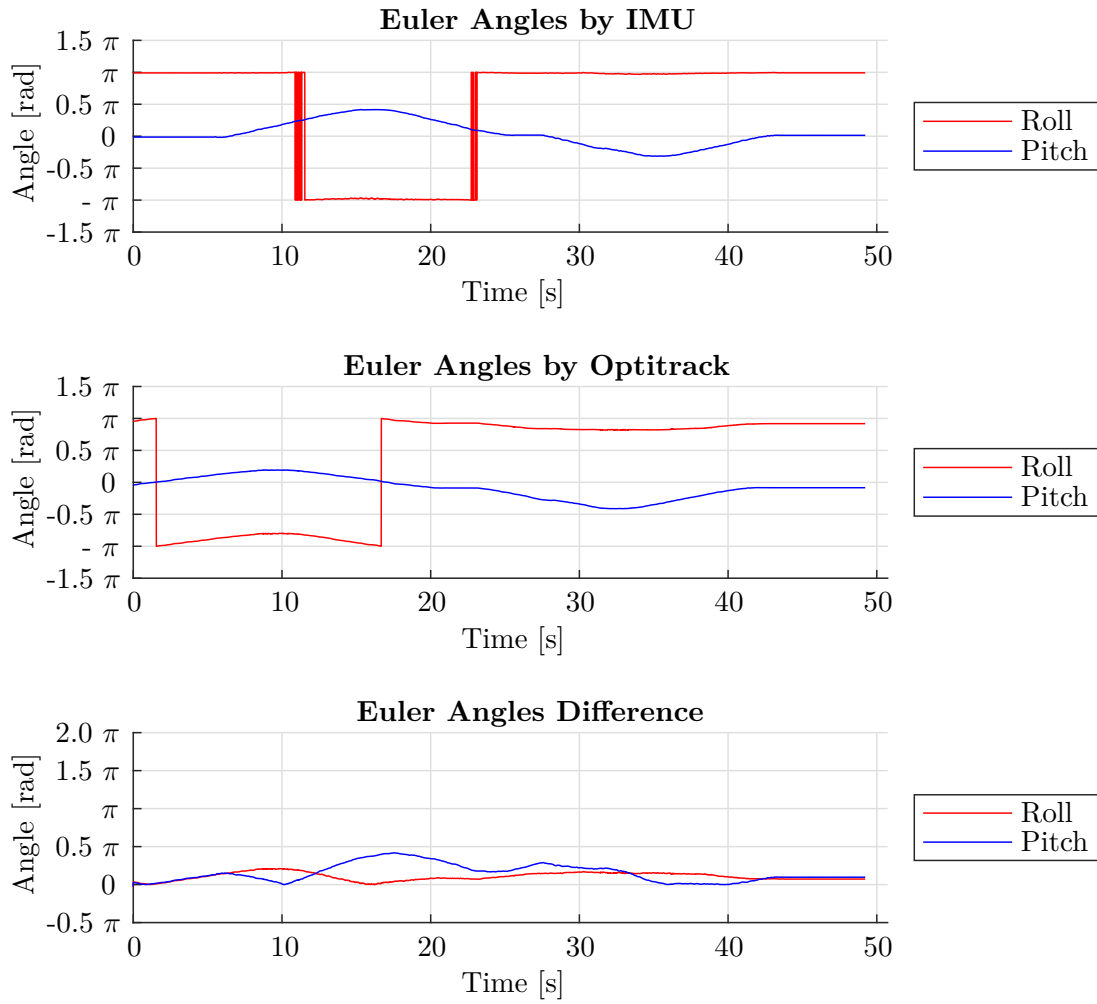


Figure A.26: Euler Angles obtained during the second experiment of Experiment B Configuration 3. Pitch rotation with one IMU at the distance of 8 cm from the center of the sphere. Top: Euler Angles determined with the IMU data and the filter. Middle: Orientation recorded from the Optitrack system. Bottom: Absolute Euler Angles difference (Ground truth minus IMU). The Euler Angles are Roll (red), Pitch (blue) and Yaw (green) plotted against time.

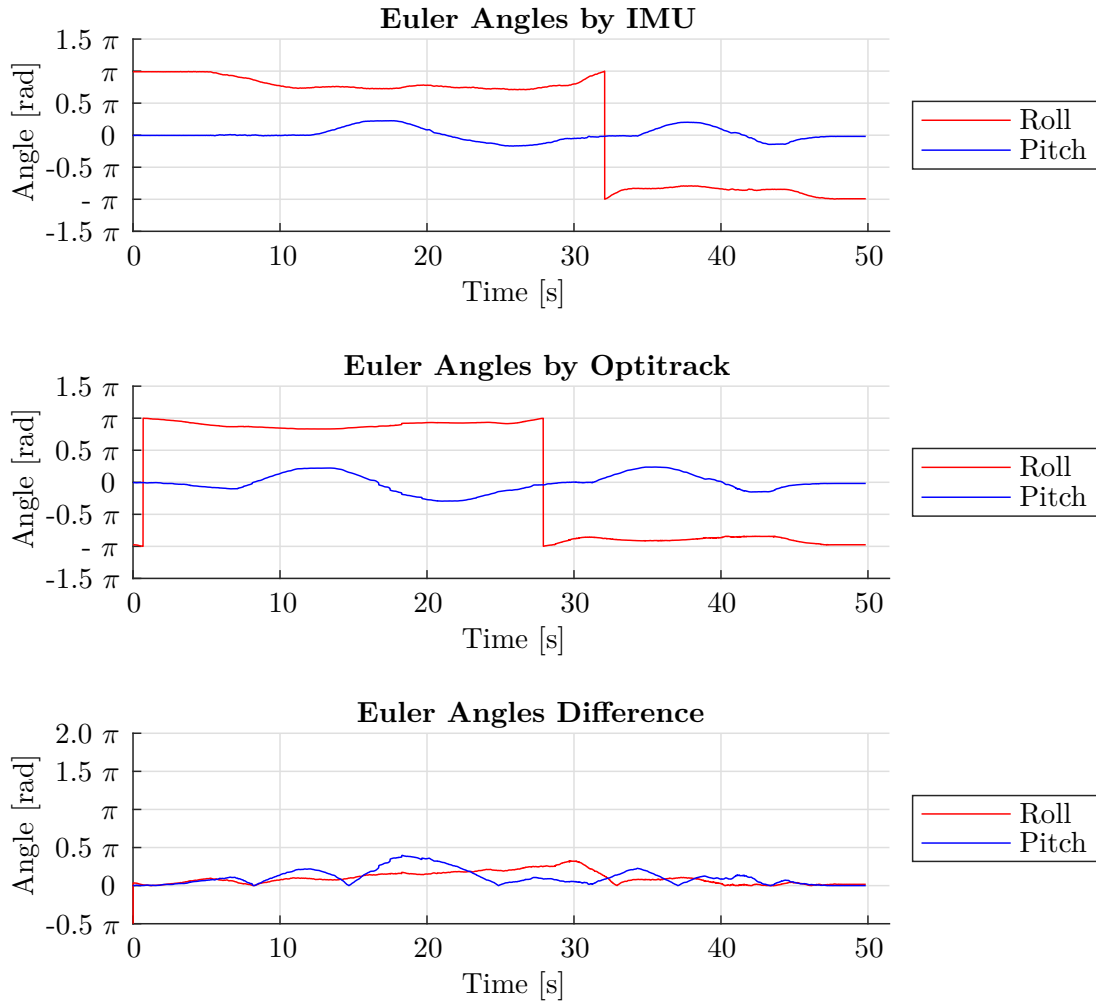


Figure A.27: Euler Angles obtained during the third experiment of Experiment B Configuration 3. Roll and Pitch rotation with one IMU at the distance of 8 cm from the center of the sphere. Top: Euler Angles determined with the IMU data and the filter. Middle: Orientation recorded from the Optitrack system. Bottom: Absolute Euler Angles difference (Ground truth minus IMU). The Euler Angles are Roll (red), Pitch (blue) and Yaw (green) plotted against time.

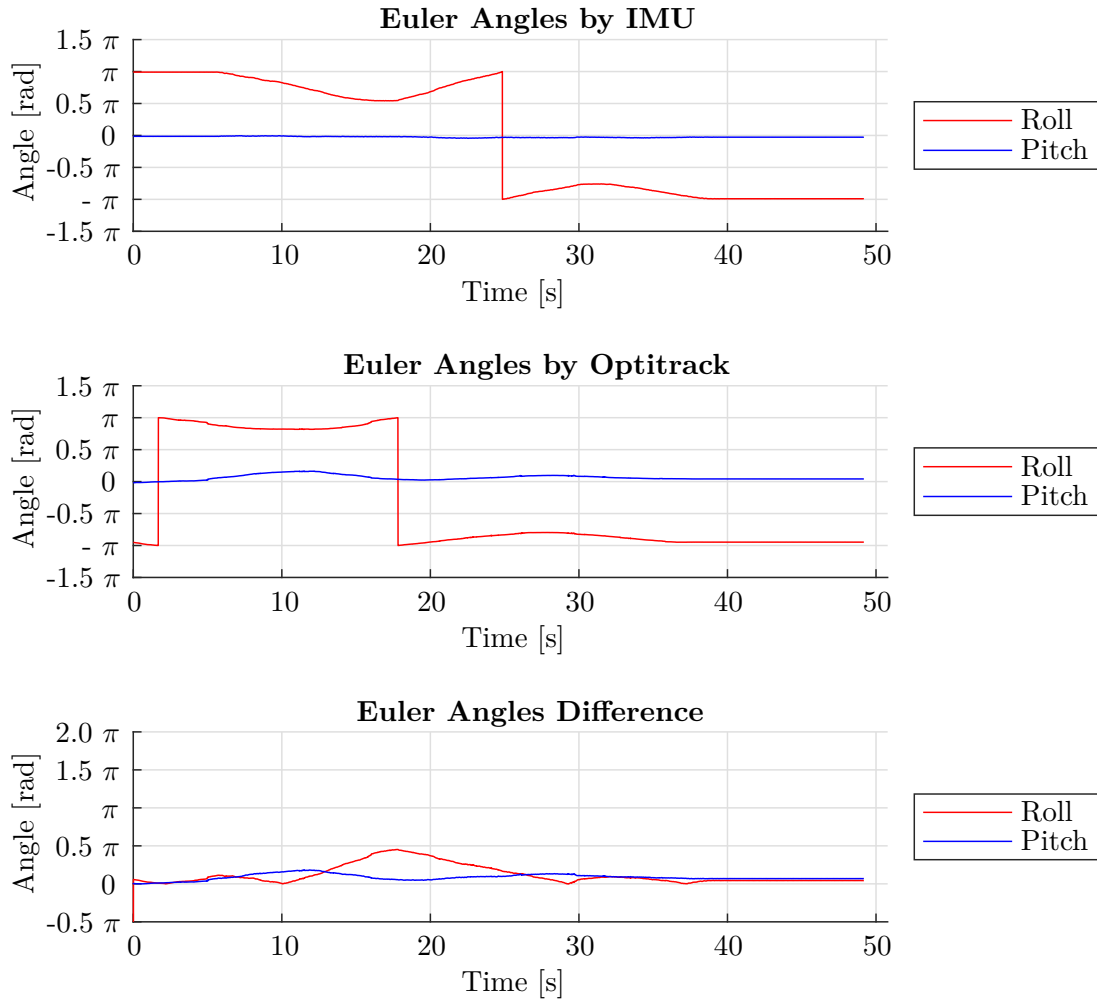
Configuration B4: One IMU at the edge of the sphere

Figure A.28: Euler Angles obtained during the first experiment of Experiment B Configuration 4. Roll rotation with one IMU at the edge of the sphere. Top: Euler Angles determined with the IMU data and the filter. Middle: Orientation recorded from the Optitrack system. Bottom: Absolute Euler Angles difference (Ground truth minus IMU). The Euler Angles are Roll (red), Pitch (blue) and Yaw (green) plotted against time.

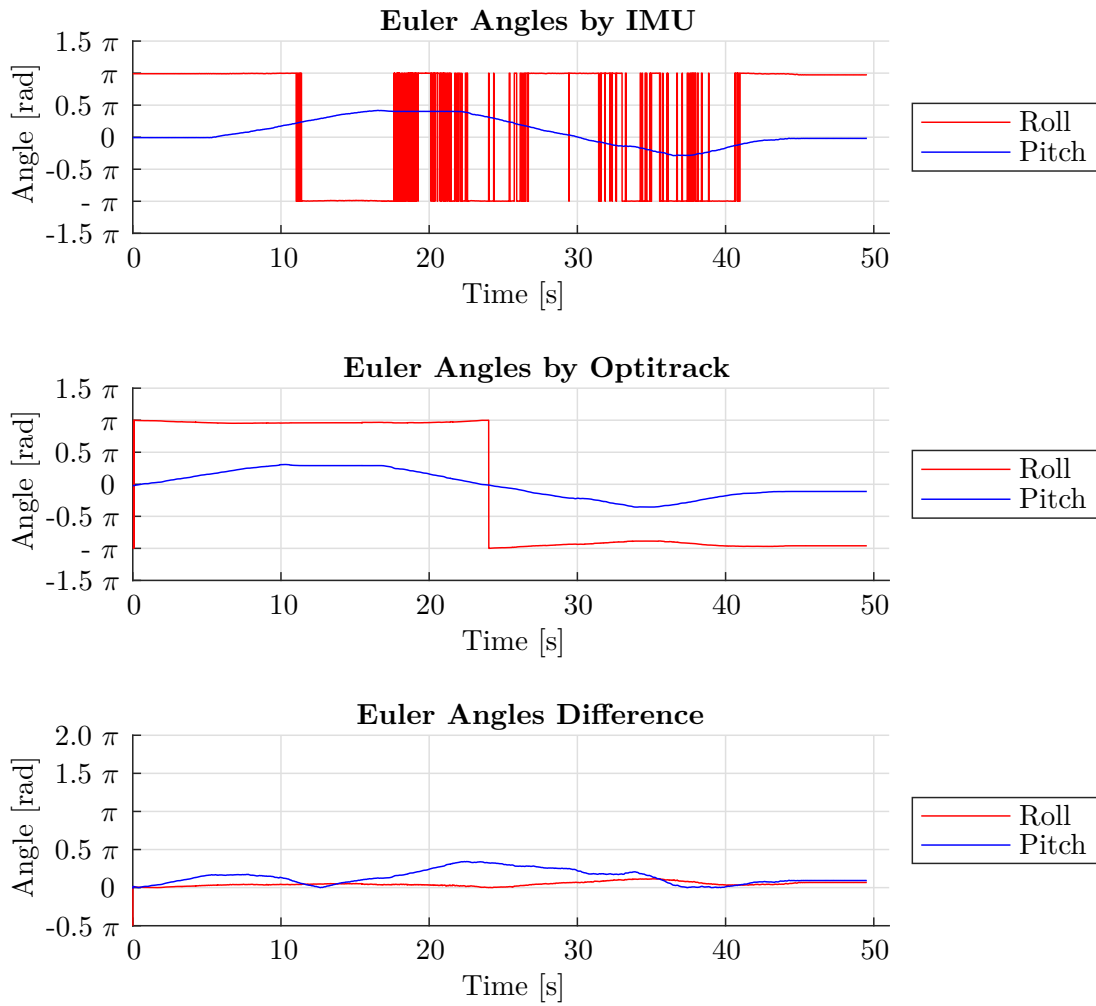


Figure A.29: Euler Angles obtained during the second experiment of Experiment B Configuration 4. Pitch rotation with one IMU at the edge of the sphere. Top: Euler Angles determined with the IMU data and the filter. Middle: Orientation recorded from the Optitrack system. Bottom: Absolute Euler Angles difference (Ground truth minus IMU). The Euler Angles are Roll (red), Pitch (blue) and Yaw (green) plotted against time.

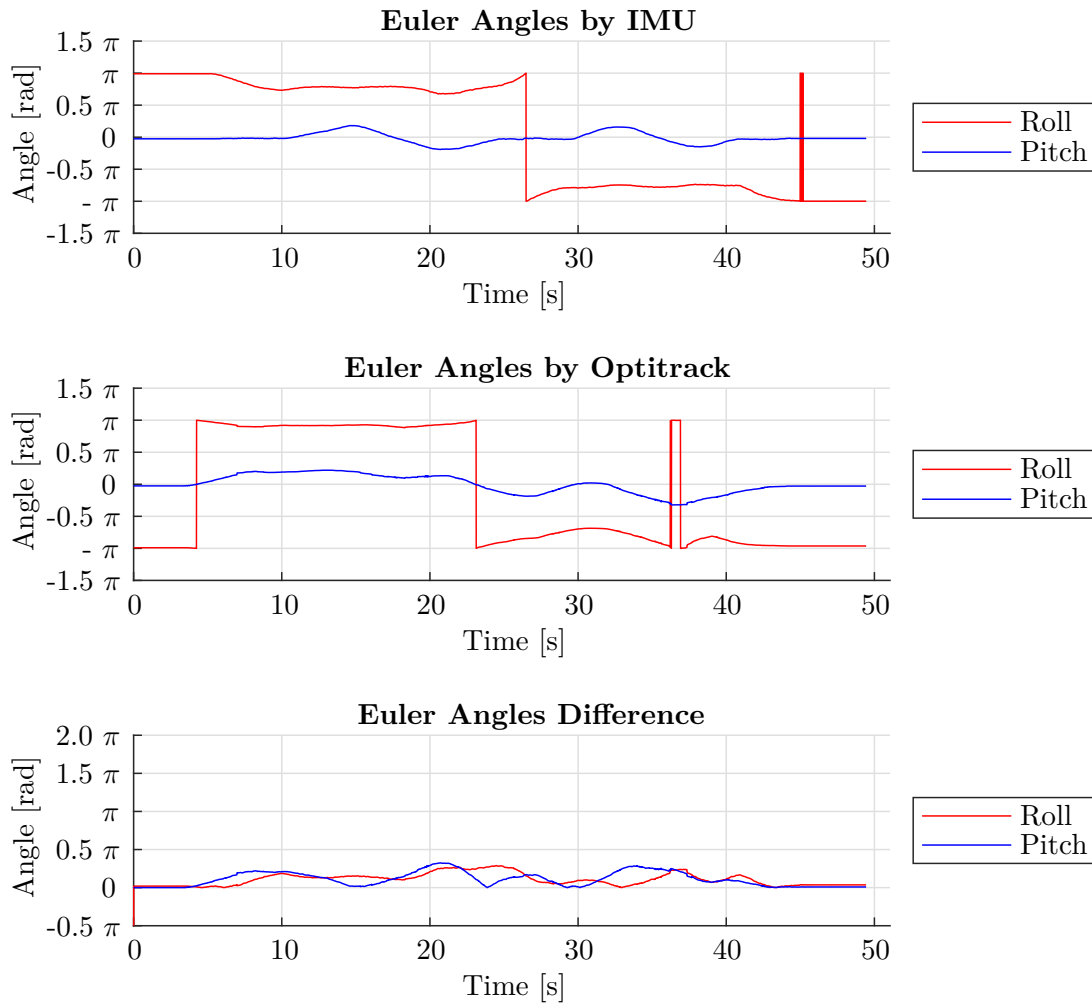


Figure A.30: Euler Angles obtained during the third experiment of Experiment B Configuration 4. Roll and Pitch rotation with one IMU at the edge of the sphere. Top: Euler Angles determined with the IMU data and the filter. Middle: Orientation recorded from the Optitrack system. Bottom: Absolute Euler Angles difference (Ground truth minus IMU). The Euler Angles are Roll (red), Pitch (blue) and Yaw (green) plotted against time.

A.3 Experiment C

Configuration C1: Two IMUs on the same side of the sphere's center

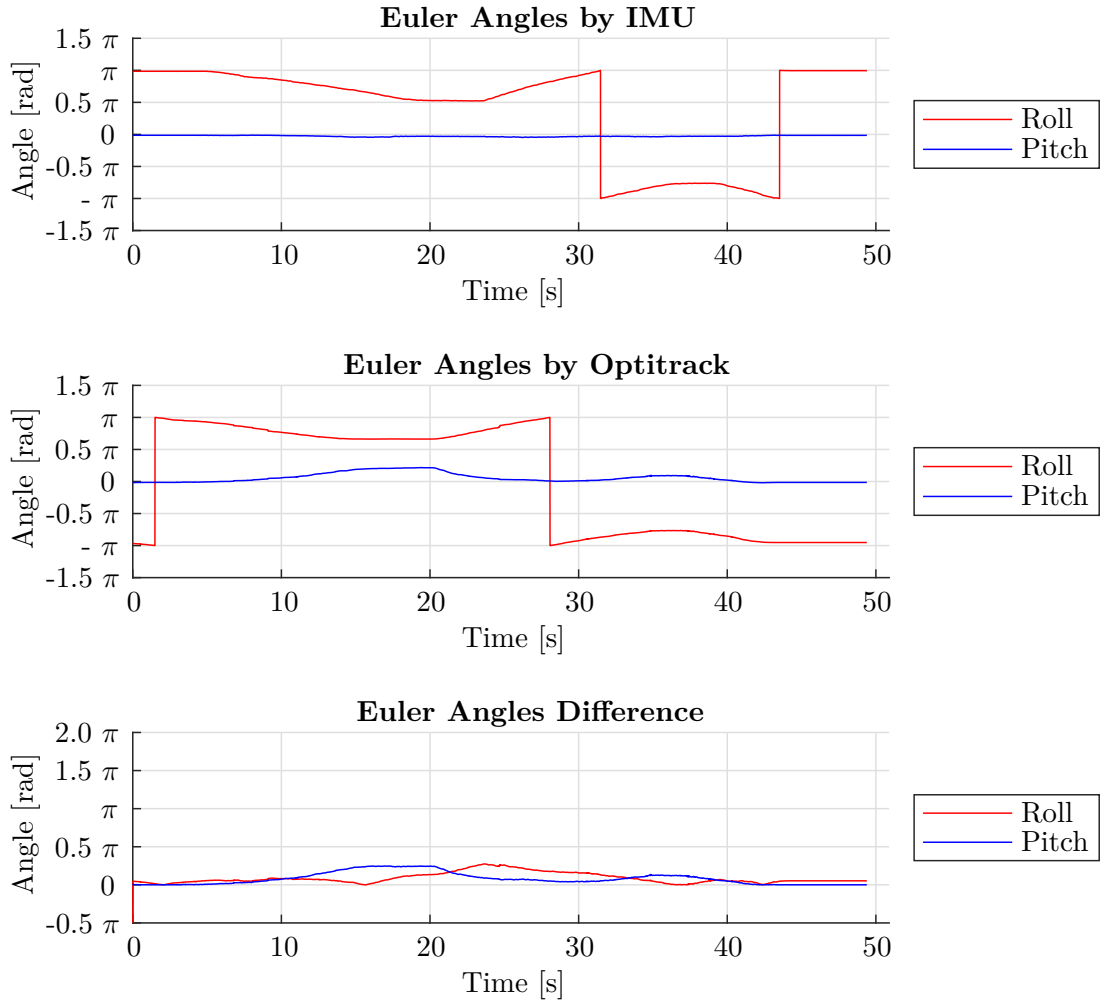


Figure A.31: Euler Angles obtained during the first experiment of Experiment C Configuration 1. Roll rotation with two IMUs on the same side of the sphere's center. Top: Euler Angles determined with the IMU data and the filter. Middle: Orientation recorded from the Optitrack system. Bottom: Absolute Euler Angles difference (Ground truth minus IMU). The Euler Angles are Roll (red), Pitch (blue) and Yaw (green) plotted against time.

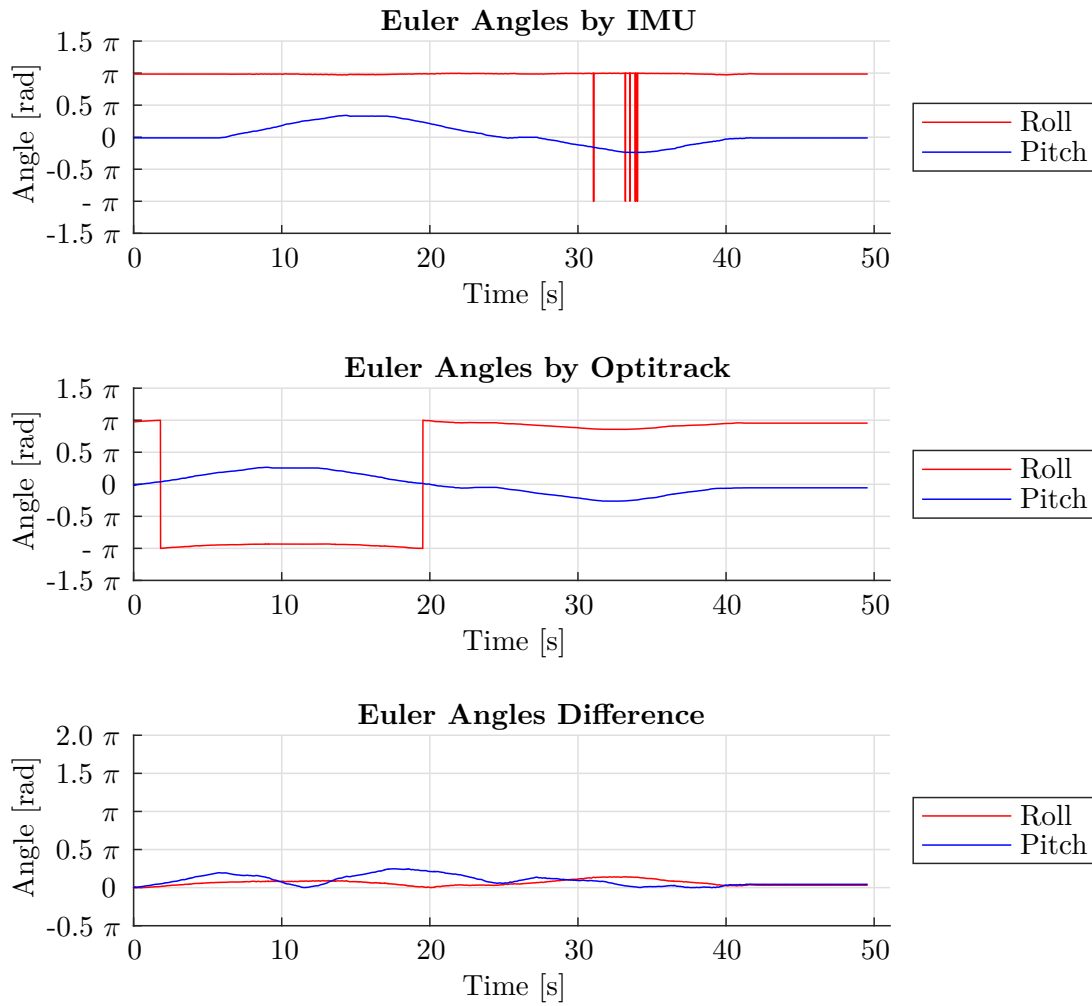


Figure A.32: Euler Angles obtained during the second experiment of Experiment C Configuration 1. Pitch rotation with two IMUs on the same side of the sphere's center. Top: Euler Angles determined with the IMU data and the filter. Middle: Orientation recorded from the Optitrack system. Bottom: Absolute Euler Angles difference (Ground truth minus IMU). The Euler Angles are Roll (red), Pitch (blue) and Yaw (green) plotted against time.

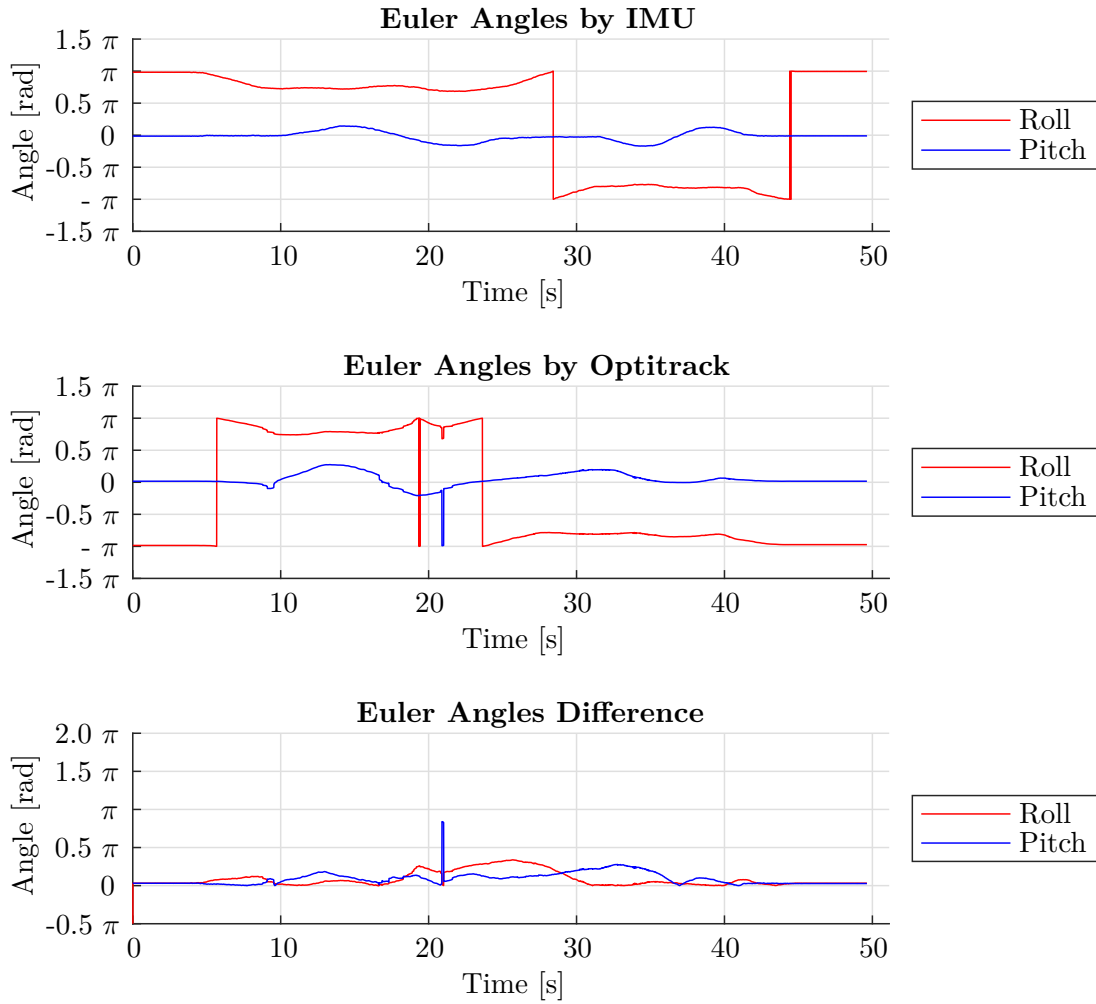


Figure A.33: Euler Angles obtained during the third experiment of Experiment C Configuration 1. Roll and Pitch rotation with two IMUs on the same side of the sphere's center. Top: Euler Angles determined with the IMU data and the filter. Middle: Orientation recorded from the Optitrack system. Bottom: Absolute Euler Angles difference (Ground truth minus IMU). The Euler Angles are Roll (red), Pitch (blue) and Yaw (green) plotted against time.

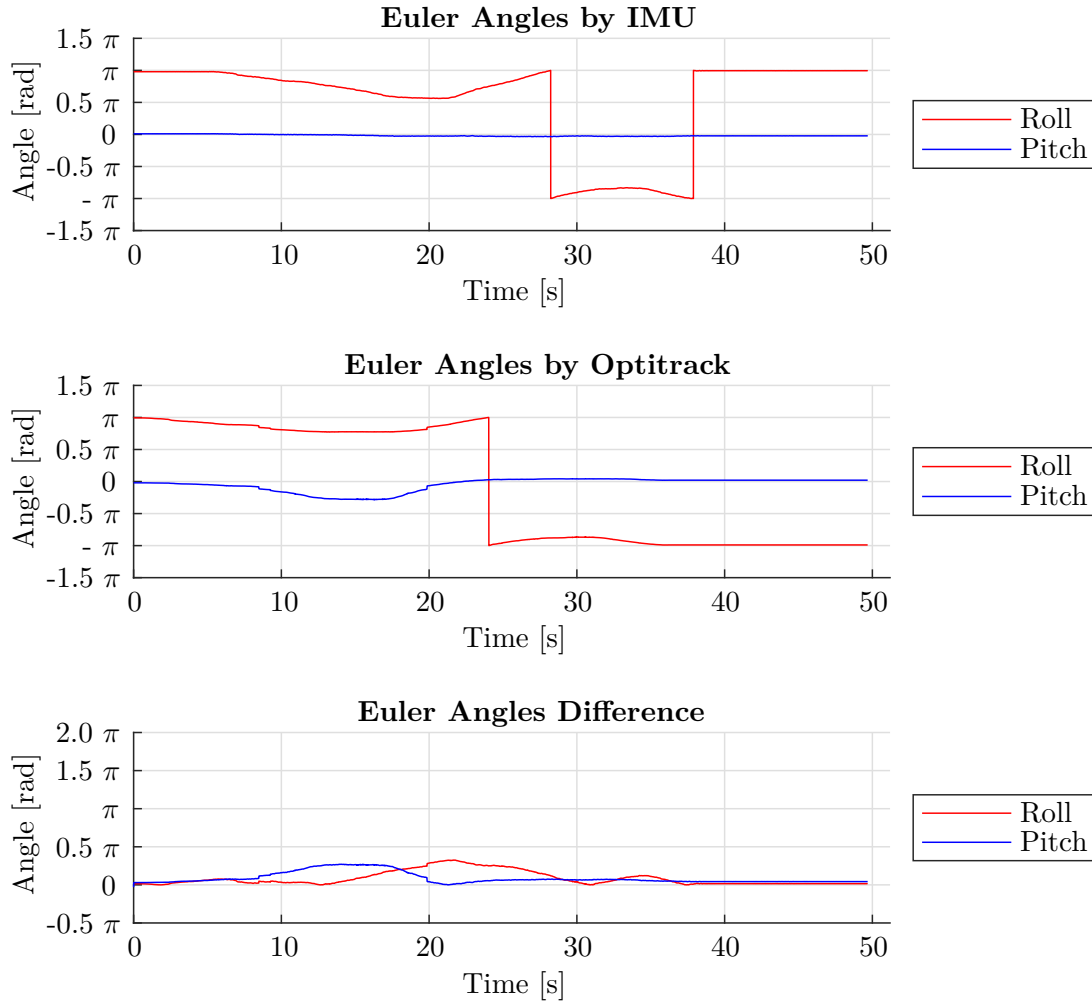
Configuration C2: Two IMUs on opposite sides of the sphere's center

Figure A.34: Euler Angles obtained during the first experiment of Experiment C Configuration 2. Roll rotation with two IMUs on opposite sides of the sphere's center. Top: Euler Angles determined with the IMU data and the filter. Middle: Orientation recorded from the Optitrack system. Bottom: Absolute Euler Angles difference (Ground truth minus IMU). The Euler Angles are Roll (red), Pitch (blue) and Yaw (green) plotted against time.

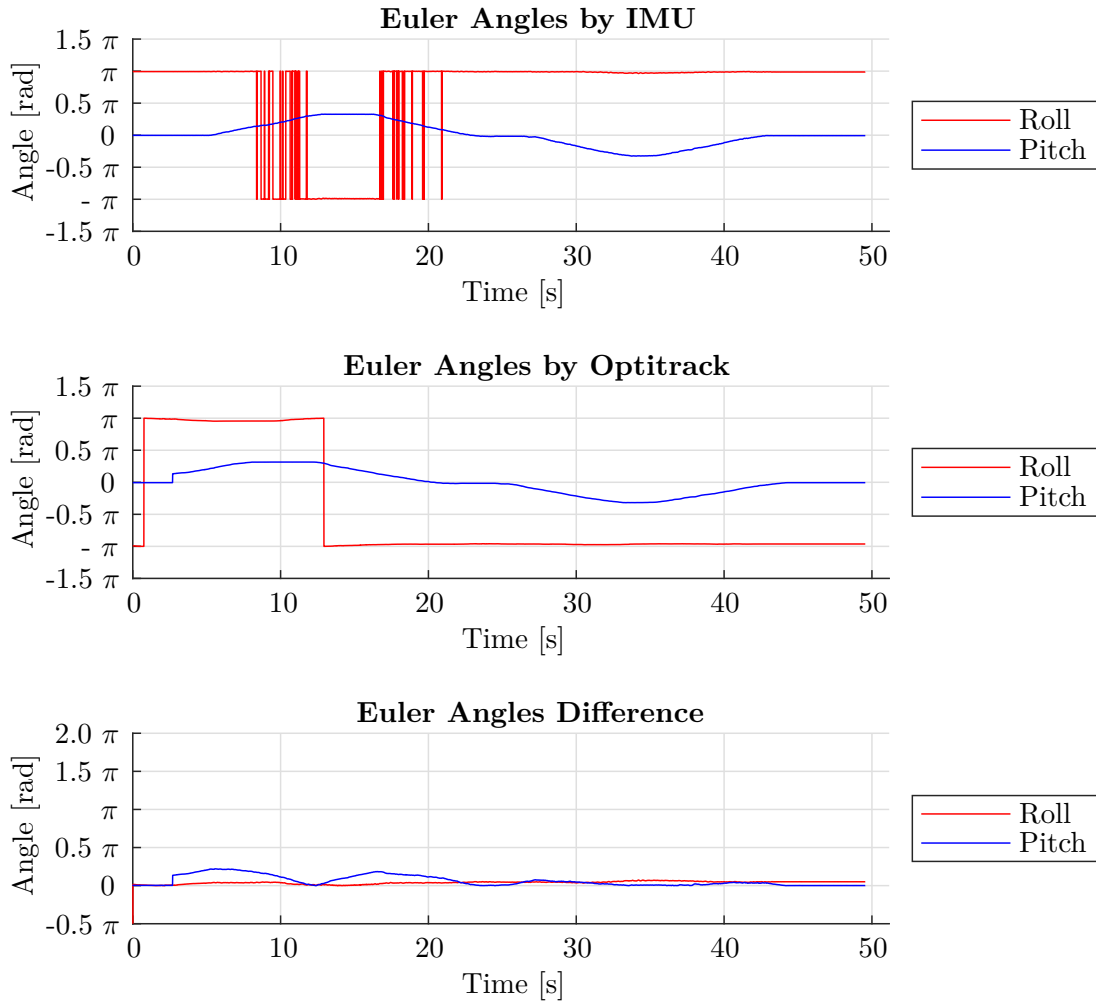


Figure A.35: Euler Angles obtained during the second experiment of Experiment C Configuration 2. Pitch rotation with two IMUs on opposite sides of the sphere's center. Top: Euler Angles determined with the IMU data and the filter. Middle: Orientation recorded from the Optitrack system. Bottom: Absolute Euler Angles difference (Ground truth minus IMU). The Euler Angles are Roll (red), Pitch (blue) and Yaw (green) plotted against time.

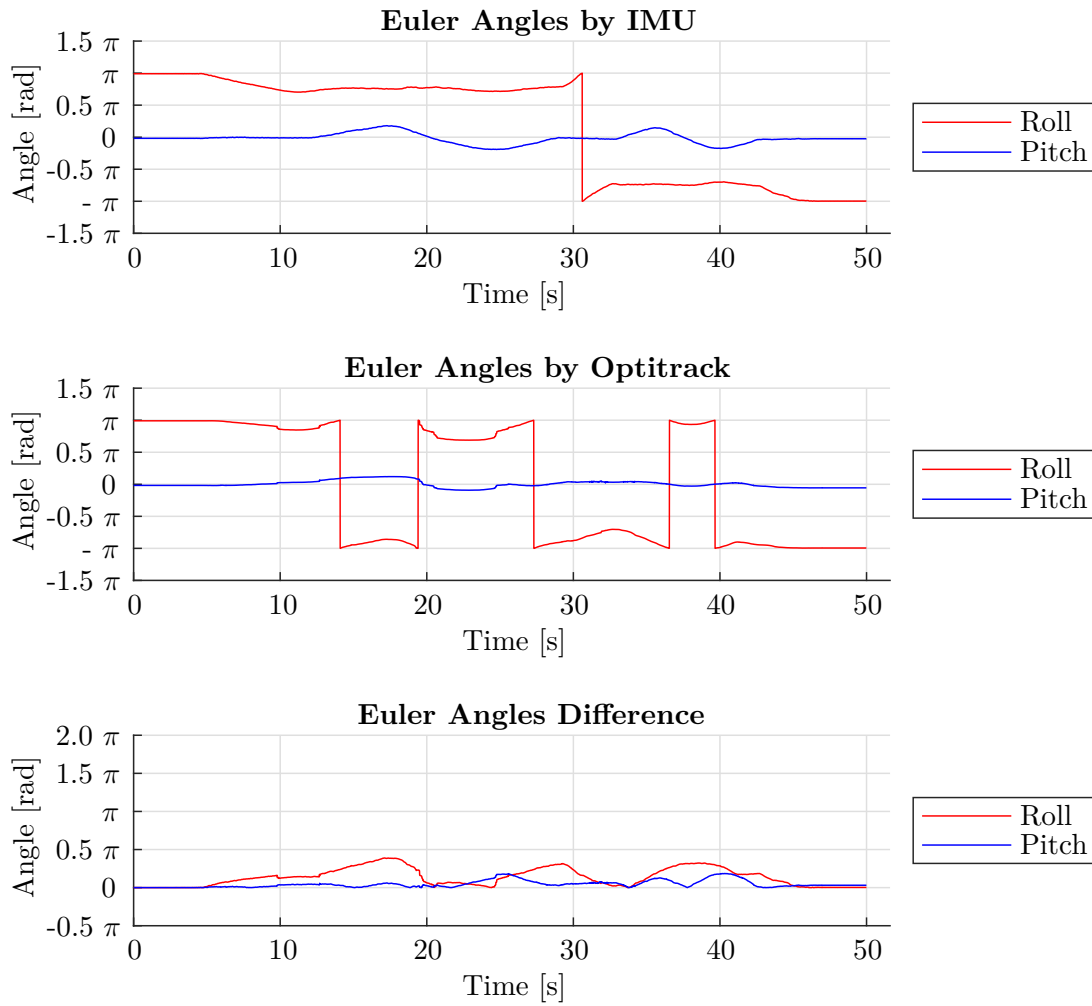


Figure A.36: Euler Angles obtained during the third experiment of Experiment C Configuration 2. Roll and Pitch rotation with two IMUs on opposite sides of the sphere's center. Top: Euler Angles determined with the IMU data and the filter. Middle: Orientation recorded from the Optitrack system. Bottom: Absolute Euler Angles difference (Ground truth minus IMU). The Euler Angles are Roll (red), Pitch (blue) and Yaw (green) plotted against time.

A.4 Experiment D

Configuration D1: Three IMUs in the center of the sphere

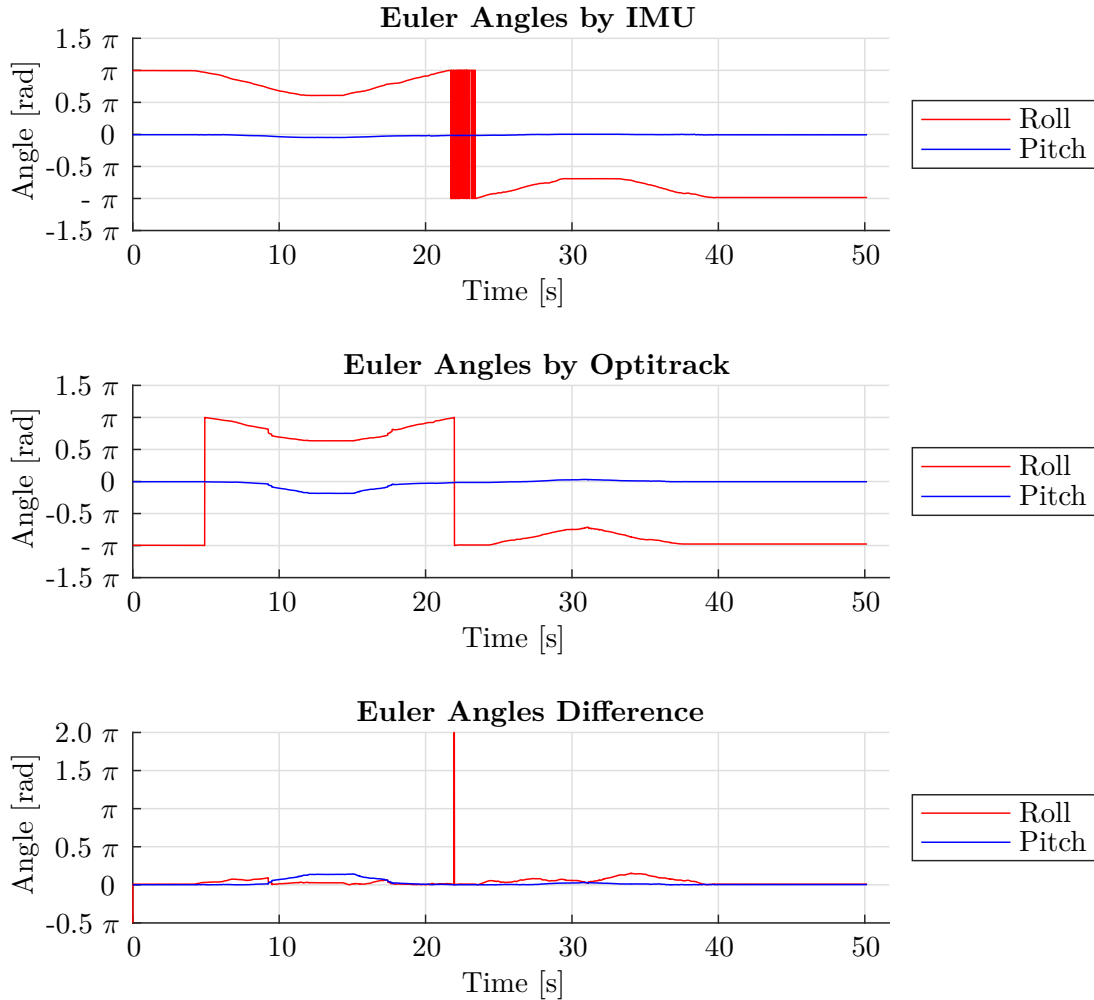


Figure A.37: Euler Angles obtained during the first experiment of Experiment D Configuration 1. Roll rotation with three IMUs in the center of the sphere. Top: Euler Angles determined with the IMU data and the filter. Middle: Orientation recorded from the Optitrack system. Bottom: Absolute Euler Angles difference (Ground truth minus IMU). The Euler Angles are Roll (red), Pitch (blue) and Yaw (green) plotted against time.

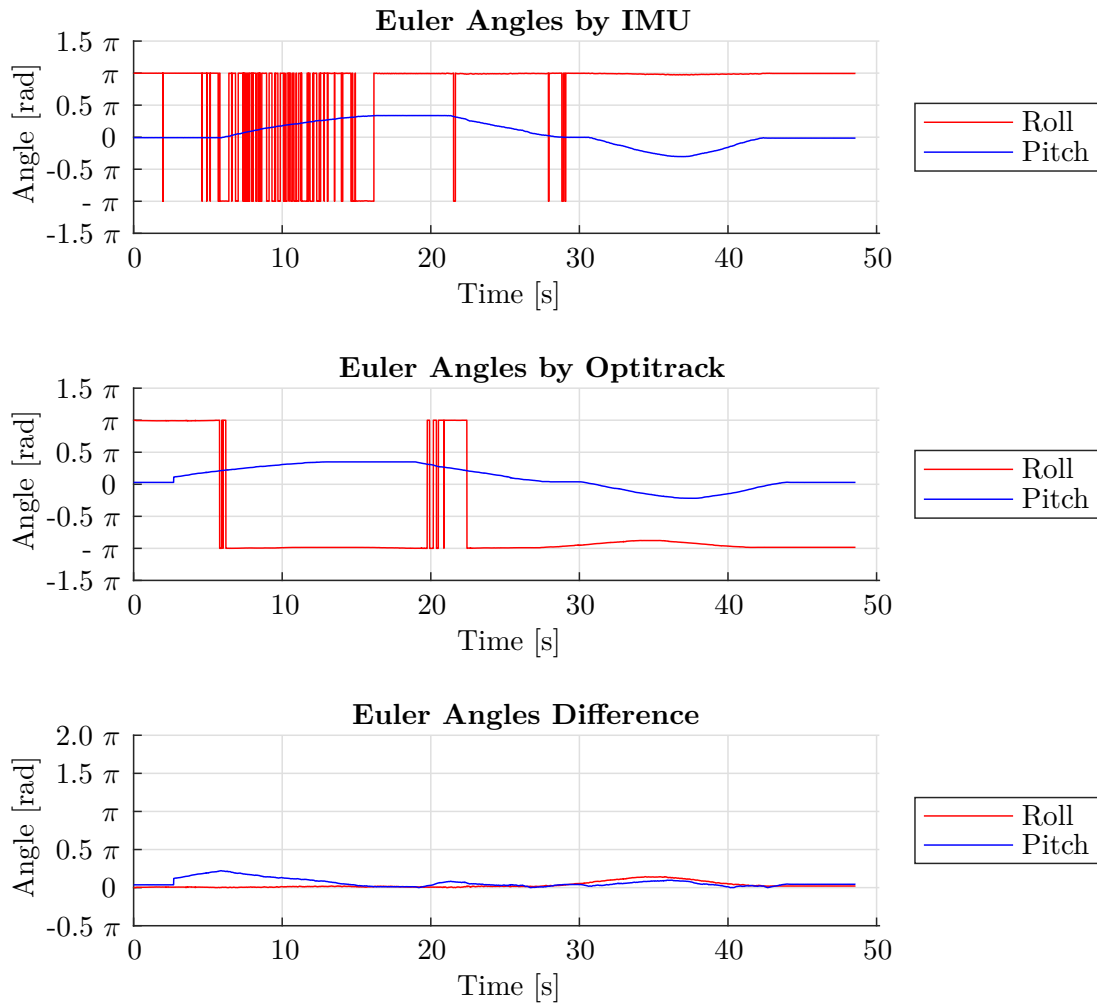


Figure A.38: Euler Angles obtained during the second experiment of Experiment D Configuration 1. Pitch rotation with three IMUs in the center of the sphere. Top: Euler Angles determined with the IMU data and the filter. Middle: Orientation recorded from the Optitrack system. Bottom: Absolute Euler Angles difference (Ground truth minus IMU). The Euler Angles are Roll (red), Pitch (blue) and Yaw (green) plotted against time.

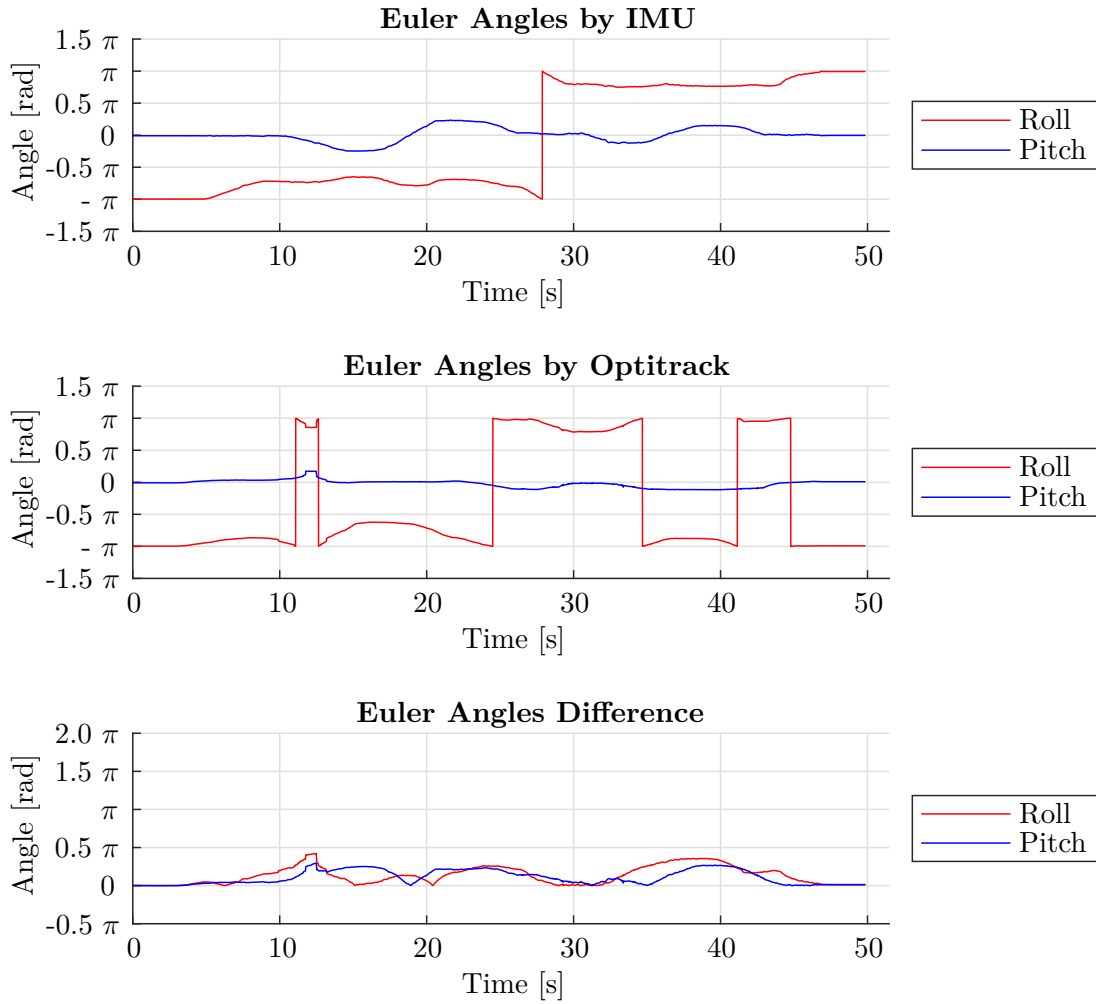


Figure A.39: Euler Angles obtained during the third experiment of Experiment D Configuration 1. Roll and Pitch rotation with three IMUs in the center of the sphere. Top: Euler Angles determined with the IMU data and the filter. Middle: Orientation recorded from the Optitrack system. Bottom: Absolute Euler Angles difference (Ground truth minus IMU). The Euler Angles are Roll (red), Pitch (blue) and Yaw (green) plotted against time.

Configuration D2: One IMU on each rotational axis

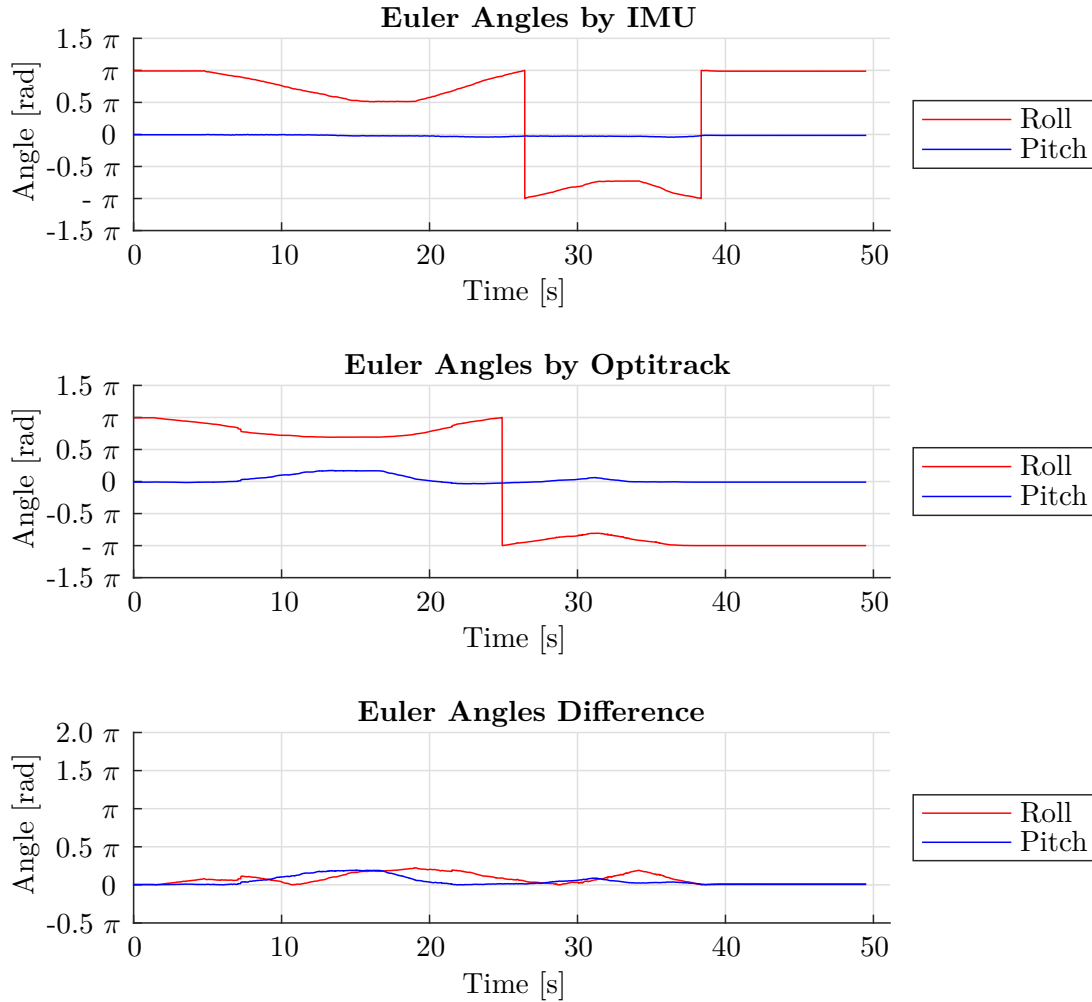


Figure A.40: Euler Angles obtained during the first experiment of Experiment D Configuration 2. Roll rotation with one IMU on each rotational axis. Top: Euler Angles determined with the IMU data and the filter. Middle: Orientation recorded from the Optitrack system. Bottom: Absolute Euler Angles difference (Ground truth minus IMU). The Euler Angles are Roll (red), Pitch (blue) and Yaw (green) plotted against time.

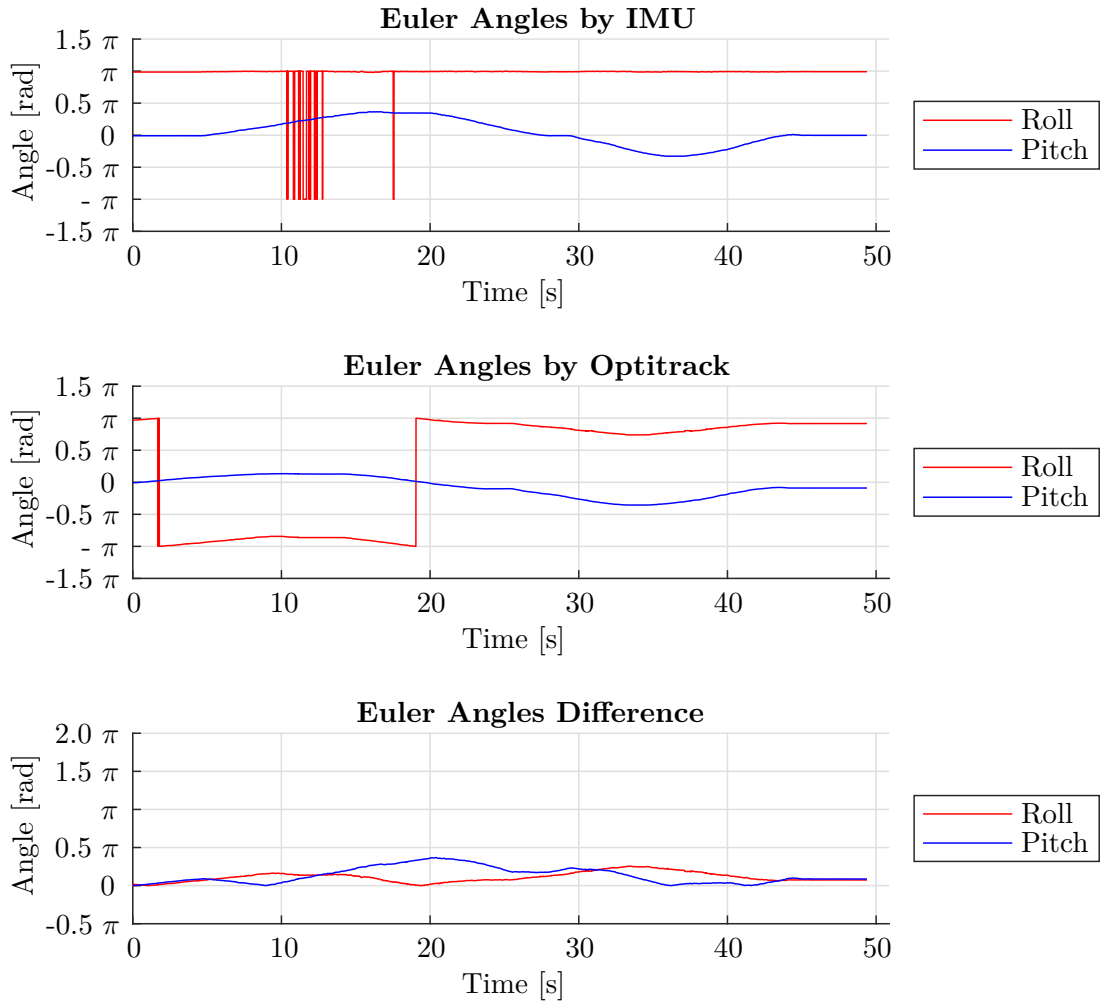


Figure A.41: Euler Angles obtained during the second experiment of Experiment D Configuration 2. Pitch rotation with one IMU on each rotational axis. Top: Euler Angles determined with the IMU data and the filter. Middle: Orientation recorded from the Optitrack system. Bottom: Absolute Euler Angles difference (Ground truth minus IMU). The Euler Angles are Roll (red), Pitch (blue) and Yaw (green) plotted against time.

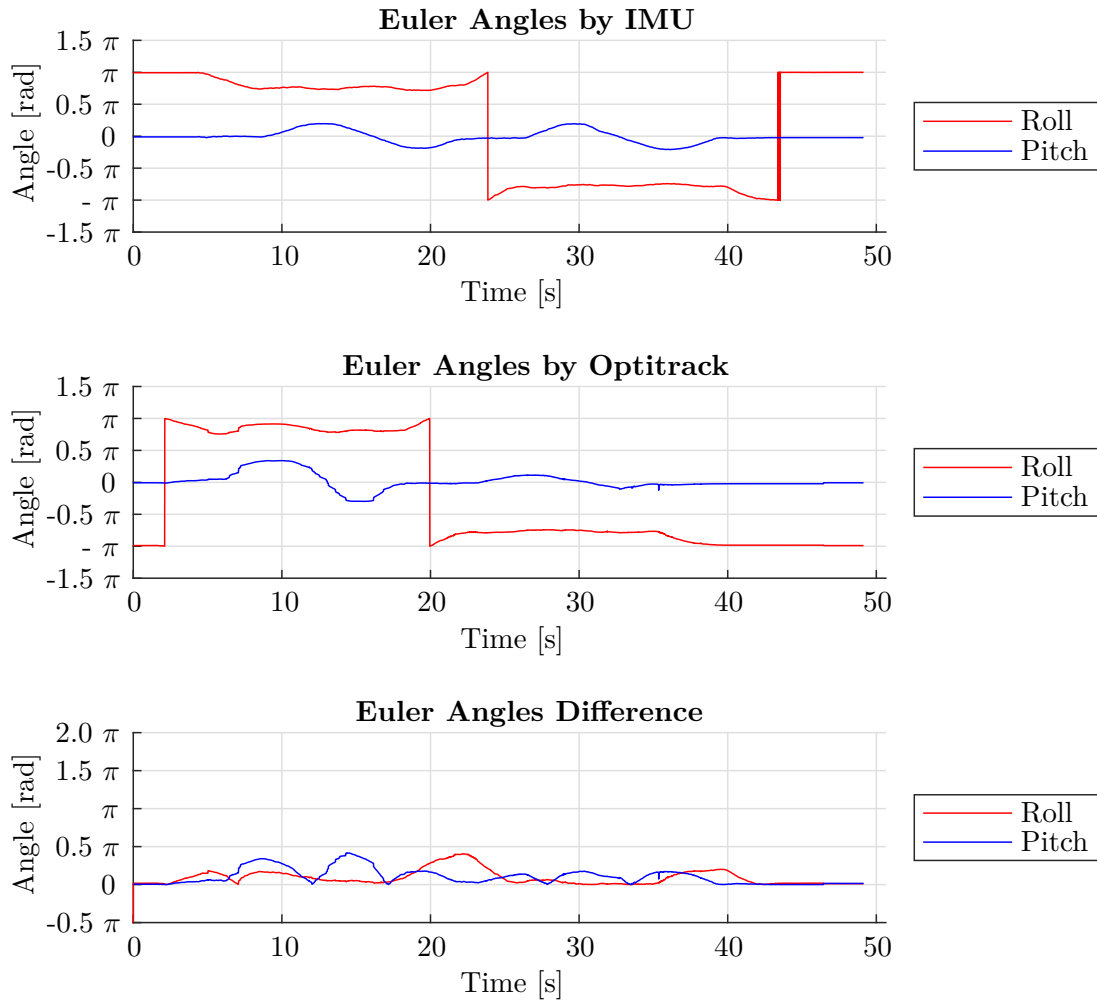


Figure A.42: Euler Angles obtained during the third experiment of Experiment D Configuration 2. Roll and Pitch rotation with one IMU on each rotational axis. Top: Euler Angles determined with the IMU data and the filter. Middle: Orientation recorded from the Optitrack system. Bottom: Absolute Euler Angles difference (Ground truth minus IMU). The Euler Angles are Roll (red), Pitch (blue) and Yaw (green) plotted against time.

Configuration D3: One IMU on each rotational axis and one IMU in the center of the sphere

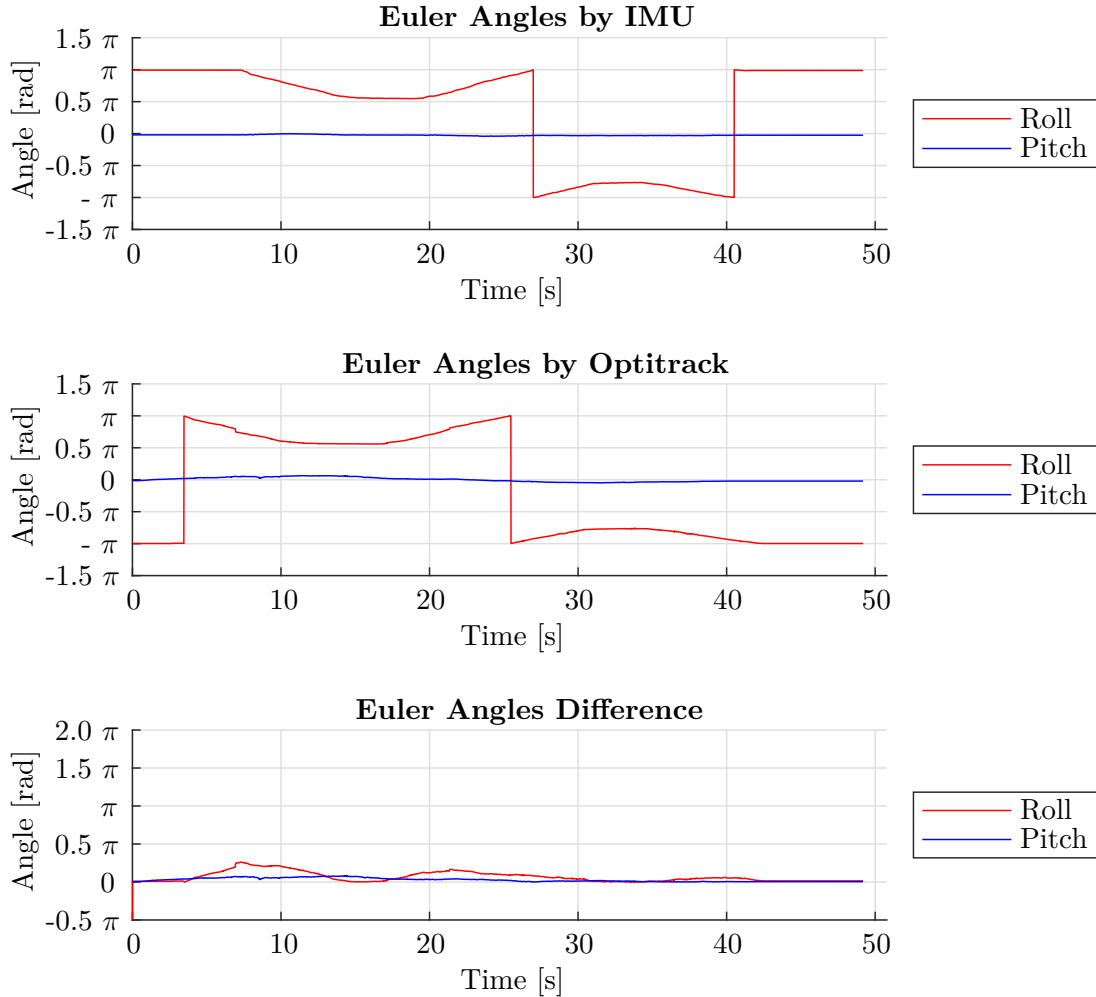


Figure A.43: Euler Angles obtained during the first experiment of Experiment D Configuration 3. Roll rotation with one IMU on each rotational axis and one IMU in the center of the sphere. Top: Euler Angles determined with the IMU data and the filter. Middle: Orientation recorded from the Optitrack system. Bottom: Absolute Euler Angles difference (Ground truth minus IMU). The Euler Angles are Roll (red), Pitch (blue) and Yaw (green) plotted against time.

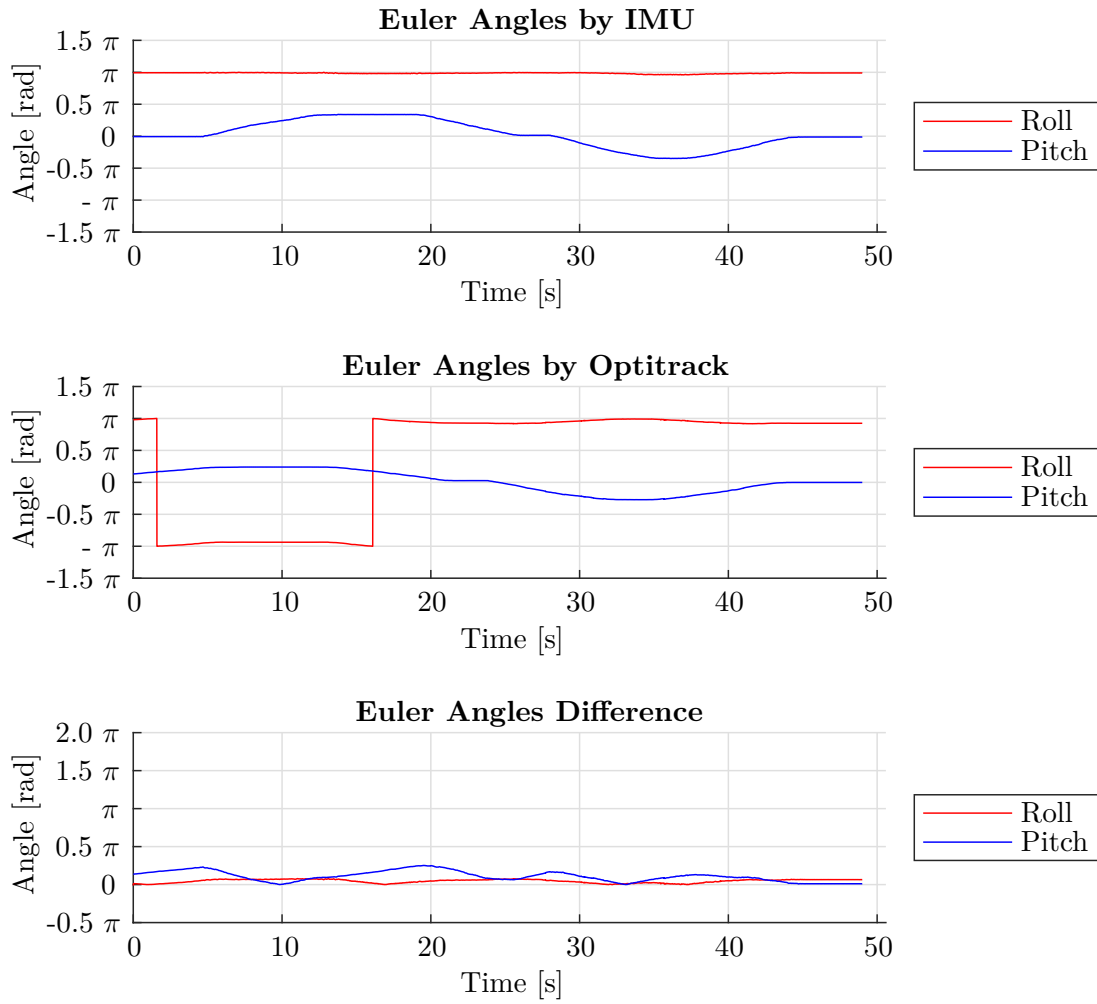


Figure A.44: Euler Angles obtained during the second experiment of Experiment D Configuration 3. Pitch rotation with one IMU on each rotational axis and one IMU in the center of the sphere. Top: Euler Angles determined with the IMU data and the filter. Middle: Orientation recorded from the Optitrack system. Bottom: Absolute Euler Angles difference (Ground truth minus IMU). The Euler Angles are Roll (red), Pitch (blue) and Yaw (green) plotted against time.

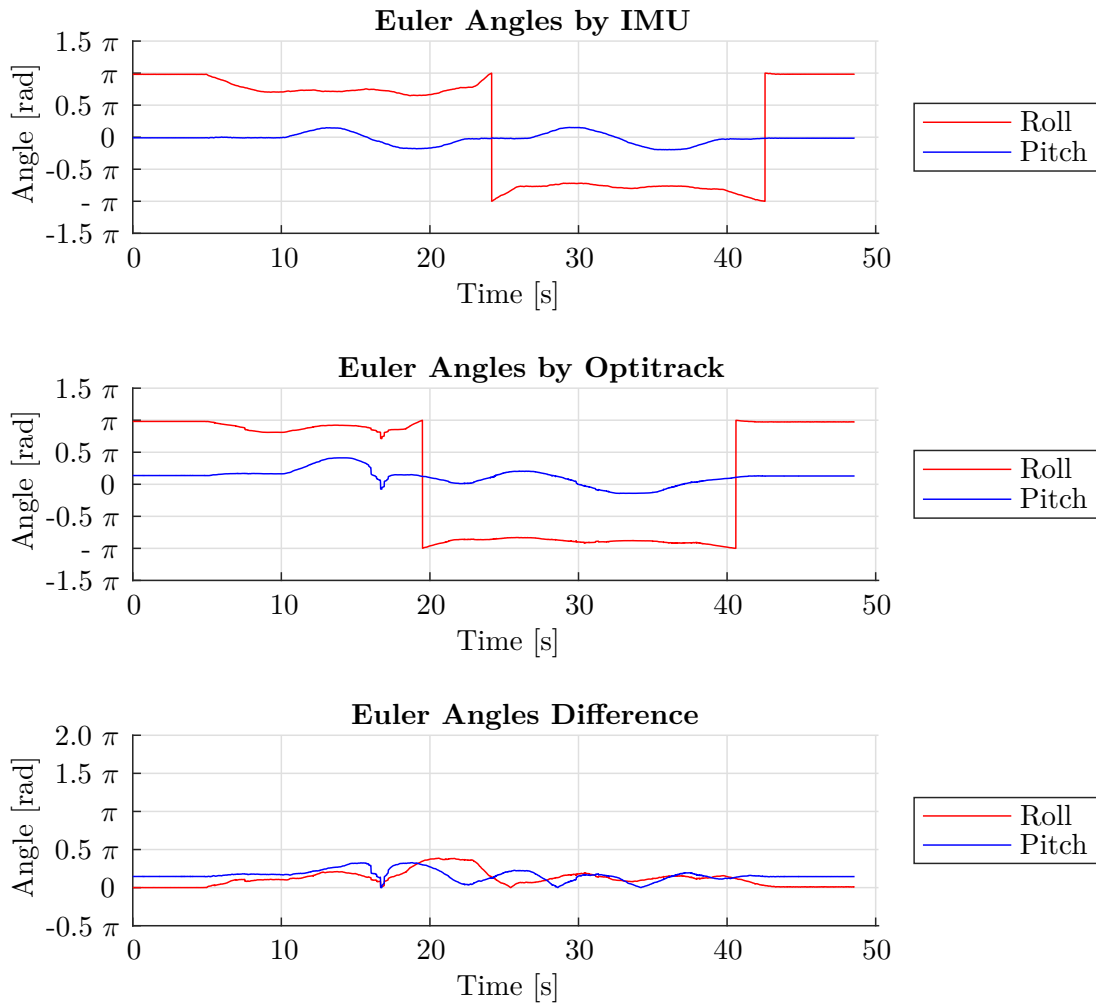


Figure A.45: Euler Angles obtained during the third experiment of Experiment D Configuration 3. Roll and Pitch rotation with one IMU on each rotational axis and one IMU in the center of the sphere. Top: Euler Angles determined with the IMU data and the filter. Middle: Orientation recorded from the Optitrack system. Bottom: Absolute Euler Angles difference (Ground truth minus IMU). The Euler Angles are Roll (red), Pitch (blue) and Yaw (green) plotted against time.

Bibliography

- [1] H Benjamin Brown and Yangsheng Xu. A single-wheel, gyroscopically stabilized robot. In *Proceedings of IEEE International Conference on Robotics and Automation*, volume 4, pages 3658–3663. IEEE, 1996.
- [2] Vrunda A Joshi, Ravi N Banavar, and Rohit Hippalgaonkar. Design and analysis of a spherical mobile robot. *Mechanism and Machine Theory*, 45(2):130–136, 2010.
- [3] J. Zevering, D. Borrmann, A. Bredenbeck, and A. Nüchter. The concept of rod-driven locomotion for spherical lunar exploration robots. In *IEEE/RSJ International Conference on Intelligent Robots and Systems (IROS '22)*, Kyoto, Japan, October 2022.
- [4] Asif A Siddiqi. *Beyond Earth: A chronicle of deep space exploration, 1958-2016*, volume 4041. National Aeronautics & Space Administration, 2018.
- [5] Physik für alle! Lunochod 1. https://www.cosmos-indirekt.de/Physik-Schule/Lunochod_1. Accessed: 15. November 2022.
- [6] Jacob Matijevic. Autonomous navigation and the sojourner microrover. *Science*, 280(5362):454–455, 1998.
- [7] NASA. Mars exploration rover - brains. <https://mars.nasa.gov/mer/mission/technology/avionics/>. Accessed: 15. November 2022.
- [8] NASA. Mars curiosity rover - brains. <https://mars.nasa.gov/msl/spacecraft/rover/brains/>. Accessed: 14. November 2022.
- [9] NASA. Mars2020 perseverance rover - brains. <https://mars.nasa.gov/mars2020/spacecraft/rover/brains/>. Accessed: 14. November 2022.
- [10] Jasper Zevering, Anton Bredenbeck, Fabian Arzberger, Dorit Borrmann, and Andreas Nüchter. Luna-a laser-mapping unidirectional navigation actuator. In *International Symposium on Experimental Robotics*, pages 85–94. Springer, 2020.
- [11] Angelo Pio Rossi, Francesco Maurelli, Vikram Unnithan, Hendrik Dreger, Kedus Mathewos, Nayan Pradhan, Dan-Andrei Corbeanu, Riccardo Pozzobon, Matteo Massironi, Sabrina Ferrari, et al. *DAEDALUS-Descent And Exploration in Deep Autonomy of Lava Underground Structures: Open Space Innovation Platform (OSIP) Lunar Caves-System Study*. 2021.

- [12] Isaac Skog, John-Olof Nilsson, and Peter Handel. An open-source multi inertial measurement unit (MIMU) platform. In *2014 International Symposium on Inertial Sensors and Systems (ISISS)*, pages 1–4, Laguna Beach, CA, USA, February 2014. IEEE.
- [13] Simone A. Ludwig. Investigation of Orientation Estimation of Multiple IMUs. *Unmanned Systems*, 09(04):283–291, October 2021. Publisher: World Scientific Publishing Co.
- [14] SBG Systems. Imu - inertial measurement unit. <https://www.sbg-systems.com/inertial-measurement-unit-imu-sensor/>. Accessed: 19. October 2022.
- [15] Adrian Waegli, Stéphane Guerrier, and Jan Skaloud. Redundant mems-imu integrated with gps for performance assessment in sports. In *2008 IEEE/ION Position, Location and Navigation Symposium*, pages 1260–1268. IEEE, 2008.
- [16] Stéphane Guerrier. Improving accuracy with multiple sensors: Study of redundant mems-imu/gps configurations. In *Proceedings of the 22nd international technical meeting of the Satellite Division of the Institute of Navigation (ION GNSS 2009)*, pages 3114–3121, 2009.
- [17] Timothy P Crain, Robert H Bishop, Tye Brady, et al. Shifting the inertial navigation paradigm with the mems technology. In *33rd Annual AAS Guidance and Control Conference*, number JSC-CN-19574, 2010.
- [18] Daniel Greenheck, Robert Bishop, Eric Jonardi, and John Christian. Design and testing of a low-cost mems imu cluster for smallsat applications. *Small Satellite Conference Technical Session III: Advanced Technologies I*, 2014.
- [19] Drew E. Bittner, John A. Christian, Robert H. Bishop, and Darryl May. Fault Detection, Isolation, and Recovery techniques for large clusters of Inertial Measurement Units. In *2014 IEEE/ION Position, Location and Navigation Symposium - PLANS 2014*, pages 219–229, Monterey, CA, USA, May 2014. IEEE.
- [20] A Srivastava and M Schwabacher. Intelligent data understanding for integrated systems health management (ishm), 2000.
- [21] Salah Sukkarieh, Peter Gibbens, Ben Grocholsky, Keith Willis, and Hugh F Durrant-Whyte. A low-cost, redundant inertial measurement unit for unmanned air vehicles. *The International Journal of Robotics Research*, 19(11):1089–1103, 2000.
- [22] Arthur J Pejsa. Optimum skewed redundant inertial navigators. *AIAA Journal*, 12(7):899–902, 1974.
- [23] T Brunner, S Changey, JP Lauffenburger, and M Basset. Multiple mems-imu localization: Architecture comparison and performance assessment. In *ICINS, 2015*, 2015.
- [24] Bruno Zappa, Giovanni Legnani, Anton J Van den Bogert, and Riccardo Adamini. On the number and placement of accelerometers for angular velocity and acceleration determination. *J. Dyn. Sys., Meas., Control*, 123(3):552–554, 2001.

- [25] Jasper Zevering, Anton Bredenbeck, Fabian Arzberger, Dorit Borrmann, and Andreas Nuechter. Imu-based pose-estimation for spherical robots with limited resources. In *2021 IEEE International Conference on Multisensor Fusion and Integration for Intelligent Systems (MFI)*, pages 1–8. IEEE, 2021.
- [26] Robert J Twiss, Eldridge M Moores, et al. *Structural geology*. Macmillan, 1992.
- [27] William Rowan Hamilton. On quaternions; or on a new system of imaginaries in algebra. *Philosophical Magazine*, 25(3):489–495, 1844.
- [28] Manon Kok, Jeroen D Hol, and Thomas B Schön. Using inertial sensors for position and orientation estimation. *arXiv preprint arXiv:1704.06053*, 2017.
- [29] John J Craig. Introduction to robotics. 2005.
- [30] Project Chrono 2016. Coordinate transformations. https://api.projectchrono.org/coordinate_transformations.html. Accessed: 18. October 2022.
- [31] Herbert Goldstein, Charles P Poole Jr, and John L Safko Sr. *Klassische mechanik*. John Wiley & Sons, 2012.
- [32] Jack B Kuipers. *Quaternions and rotation sequences: a primer with applications to orbits, aerospace, and virtual reality*. Princeton university press, 1999.
- [33] Sebastian Madgwick et al. An efficient orientation filter for inertial and inertial/magnetic sensor arrays. *Report x-io and University of Bristol (UK)*, 25:113–118, 2010.
- [34] Wolfgang Rindler. *Essential relativity: special, general, and cosmological*. Springer Science & Business Media, 1977.
- [35] Embedded Inventor 2022. Imu sensors: Everything you need to know! https://embeddedinventor.com/what-is-an-imu-sensor-a-complete-guide-for-beginners/#How_IMU_works. Accessed: 19. October 2022.
- [36] Avinash N Bhat. Mems technology and working principle of accelerometers, 2020. <https://timestech.in/mems-technology-and-working-principle-of-accelerometers/>. Accessed: 24. October 2022.
- [37] Vishwanath Tigadi. Mems gyroscope precision inertial sensing in harsh, high temperature environments, 2016. <https://www.edn.com/mems-gyroscope-precision-inertial-sensing-in-harsh-high-temperature-environments/>. Accessed: 24. October 2022.
- [38] Dejan. What is mems? accelerometer, gyroscope & magnetometer with arduino. <https://howtomechatronics.com/how-it-works/electrical-engineering/mems-accelerometer-gyrocope-magnetometer-arduino/>. Accessed: 24. October 2022.
- [39] LEIFI Physik. Hall-effekt. <https://www.leifiphysik.de/elektrizitaetslehre/bewegte-ladungen-feldern/grundwissen/hall-effekt>. Accessed: 24. October 2022.

- [40] Shane Colton and FRC Mentor. The balance filter. *Presentation, Massachusetts Institute of Technology*, 2007.
- [41] Walter T Higgins. A comparison of complementary and kalman filtering. *IEEE Transactions on Aerospace and Electronic Systems*, (3):321–325, 1975.
- [42] Pengfei Gui, Liqiong Tang, and Subhas Mukhopadhyay. MemS based imu for tilting measurement: Comparison of complementary and kalman filter based data fusion. In *2015 IEEE 10th conference on Industrial Electronics and Applications (ICIEA)*, pages 2004–2009. IEEE, 2015.
- [43] Vincent A Crossley. A literature review on the design of spherical rolling robots. *Pittsburgh, Pa*, pages 1–6, 2006.
- [44] Richard Chase and Abhilash Pandya. A review of active mechanical driving principles of spherical robots. *Robotics*, 1(1):3–23, 2012.
- [45] Francois Michaud and Serge Caron. Roball, the rolling robot. *Autonomous robots*, 12(2):211–222, 2002.
- [46] Viktor Kaznov and Mattias Seeman. Outdoor navigation with a spherical amphibious robot. In *2010 IEEE/RSJ International Conference on Intelligent Robots and Systems*, pages 5113–5118. IEEE, 2010.
- [47] Bo Zhao, Pengfei Wang, Haiyan Hu, Mantian Li, and Lining Sun. Study on turning in place of a spherical robot based on stick-slip principle. In *2009 IEEE International Conference on Robotics and Biomimetics (ROBIO)*, pages 771–775. IEEE, 2009.
- [48] Bo Zhao, Mantian Li, Haitao Yu, Haiyan Hu, and Lining Sun. Dynamics and motion control of a two pendulums driven spherical robot. In *2010 IEEE/RSJ International Conference on Intelligent Robots and Systems*, pages 147–153. IEEE, 2010.
- [49] Qiang Zhan, Yao Cai, and Caixia Yan. Design, analysis and experiments of an omni-directional spherical robot. In *2011 IEEE International Conference on Robotics and Automation*, pages 4921–4926. IEEE, 2011.
- [50] Yue Ming, Deng Zongquan, Yu Xinyi, and Yu Weizhen. Introducing hit spherical robot: dynamic modeling and analysis based on decoupled subsystem. In *2006 IEEE International Conference on Robotics and Biomimetics*, pages 181–186. IEEE, 2006.
- [51] J Alves and J Dias. Design and control of a spherical mobile robot. *Proceedings of the Institution of Mechanical Engineers, Part I: Journal of Systems and Control Engineering*, 217(6):457–467, 2003.
- [52] Ranjan Mukherjee, Mark A Minor, and Jay T Pukrushpan. Simple motion planning strategies for spherobot: a spherical mobile robot. In *Proceedings of the 38th IEEE Conference on Decision and Control (Cat. No. 99CH36304)*, volume 3, pages 2132–2137. IEEE, 1999.

- [53] James Lux. Alternative way of shifting mass to move a spherical robot. *NASA Tech Briefs - 'Beach-Ball' Robotic Rovers*, 19(11):83, 2005.
- [54] Puyan Mojabi et al. Introducing august: a novel strategy for an omnidirectional spherical rolling robot. In *Proceedings 2002 IEEE International Conference on Robotics and Automation (Cat. No. 02CH37292)*, volume 4, pages 3527–3533. IEEE, 2002.
- [55] Matteo Artusi, Marco Potz, Jeydmer Aristizabal, Carlo Menon, Silvio Cocuzza, and Stefano Debei. Electroactive elastomeric actuators for the implementation of a deformable spherical rover. *IEEE/ASME Transactions on Mechatronics*, 16(1):50–57, 2011.
- [56] Keith W Wait, Philip J Jackson, and Lanny S Smoot. Self locomotion of a spherical rolling robot using a novel deformable pneumatic method. In *2010 IEEE International Conference on Robotics and Automation*, pages 3757–3762. IEEE, 2010.
- [57] Yuuta Sugiyama, Ayumi Shiotsu, Masashi Yamanaka, and Shinichi Hirai. Circular/spherical robots for crawling and jumping. In *Proceedings of the 2005 IEEE International Conference on Robotics and Automation*, pages 3595–3600. IEEE, 2005.
- [58] Kwok Wai Au and Yangsheng Xu. Decoupled dynamics and stabilization of single wheel robot. In *Proceedings 1999 IEEE/RSJ International Conference on Intelligent Robots and Systems. Human and Environment Friendly Robots with High Intelligence and Emotional Quotients (Cat. No. 99CH36289)*, volume 1, pages 197–203. IEEE, 1999.
- [59] Phidgets Inc. 2022. Phidgetspatial precision 3/3/3 high resolution. <https://www.phidgets.com/?tier=3&catid=10&pcid=8&prodid=1158>. Accessed: 06. October 2022.
- [60] Inc. DBA OptiTrack 2022. Optitrack - v120 trio. <https://optitrack.com/cameras/v120-trio/>. Accessed: 07. October 2022.
- [61] Paul Bovbel. `vrpn_client_ros`. http://wiki.ros.org/vrpn_client_ros. Accessed: 07. October 2022.
- [62] Mili Shah, Roger Eastman, and Tsai Hong. An overview of robot-sensor calibration methods for evaluation of perception systems. 2012 Performance Metrics for Intelligent Systems Workshop, College Park, MD, US, 2012.
- [63] Mili Shah. Calibration and registration techniques for robotics, 2014. <http://math.loyola.edu/~mili/Calibration/>. Accessed: 07. October 2022.
- [64] Raspberry Pi. Raspberry pi 3 model b. <https://www.raspberrypi.com/products/raspberry-pi-3-model-b/>. Accessed 06. October 2022.
- [65] Ubiquity Robotics. Raspberry pi images. https://learn.ubiquityrobotics.com/noetic_pi_image_downloads. Accessed: 23. Dezember 2022.
- [66] newbedev. Map vs. hashmap in c++. <https://newbedev.com/map-vs-hash-map-in-c>. Accessed: TODO 13. July 2022.

- [67] Right-hand rule. https://en.wikipedia.org/wiki/Right-hand_rule. Accessed: TODO 13. July 2022.
- [68] Piyatap Promrit, Somphop Chokchaitam, and Masami Ikura. In-vehicle mems imu calibration using accelerometer. In *2018 IEEE 5th International Conference on Smart Instrumentation, Measurement and Application (ICSIMA)*, pages 1–3. IEEE, 2018.
- [69] Yuan Zhong and Yong Xu. A calibration method of uav accelerometer based on levenberg-marquardt iteration algorithm. In *2018 Chinese Control And Decision Conference (CCDC)*, pages 5634–5638. IEEE, 2018.
- [70] Minh Long Hoang and Antonio Pietrosanto. Yaw/heading optimization by drift elimination on mems gyroscope. *Sensors and Actuators A: Physical*, 325:112691, 2021.
- [71] Eric Foxlin et al. Motion tracking requirements and technologies, 2002.
- [72] Salah Sukkarieh, Eduardo Mario Nebot, and Hugh F Durrant-Whyte. A high integrity imu/gps navigation loop for autonomous land vehicle applications. *IEEE transactions on robotics and automation*, 15(3):572–578, 1999.
- [73] Simone A Ludwig. Optimization of control parameter for filter algorithms for attitude and heading reference systems. In *2018 IEEE Congress on Evolutionary Computation (CEC)*, pages 1–8. IEEE, 2018.
- [74] Haifeng Dong and Yang Gao. Comparison of compensation mechanism between an nmr gyroscope and an serf gyroscope. *IEEE Sensors Journal*, 17(13):4052–4055, 2017.
- [75] O Nonnarit, Armando Barreto, et al. Gyroscope drift correction algorithm for inertial measurement unit used in hand motion tracking. In *2016 IEEE SENSORS*, pages 1–3. IEEE, 2016.
- [76] Qinglin Tian, Kevin I-Kai Wang, and Zoran Salcic. An ins and uwb fusion-based gyroscope drift correction approach for indoor pedestrian tracking. *Sensors*, 20(16):4476, 2020.
- [77] Chan-Gun Lee, Nhu-Ngoc Dao, Seonmin Jang, Deokhwan Kim, Yonghun Kim, and Sungrae Cho. Gyro drift correction for an indirect kalman filter based sensor fusion driver. *Sensors*, 16(6):864, 2016.
- [78] Billur Barshan and Hugh F Durrant-Whyte. Evaluation of a solid-state gyroscope for robotics applications. *IEEE Transactions on Instrumentation and measurement*, 44(1):61–67, 1995.
- [79] Antonio Ramón Jiménez, Fernando Seco, José Carlos Prieto, and Jorge Guevara. Indoor pedestrian navigation using an ins/ekf framework for yaw drift reduction and a foot-mounted imu. In *2010 7th workshop on positioning, navigation and communication*, pages 135–143. IEEE, 2010.

-
- [80] Zhanlin Diao, Haiyang Quan, Lidong Lan, and Yifei Han. Analysis and compensation of mems gyroscope drift. In *2013 Seventh International Conference on Sensing Technology (ICST)*, pages 592–596. IEEE, 2013.
- [81] Y Akcayir and Yakup Ozkazanc. Gyroscope drift estimation analysis in land navigation systems. In *Proceedings of 2003 IEEE Conference on Control Applications, 2003. CCA 2003.*, volume 2, pages 1488–1491. IEEE, 2003.
- [82] Luqiang Shi, Yigang He, Bing Li, Yuting Wu, Yuan Huang, and Tongtong Cheng. On-line measurement of dynamic tilt angle by compensating gyroscope drift error. *IEEE Transactions on Instrumentation and Measurement*, 68(9):3244–3252, 2018.

Proclamation

Hereby I confirm that I wrote this thesis independently and that I have not made use of any other resources or means than those indicated.

Würzburg, January 2023